Nanofabrication and Characterization of Nanoelectronic Biosensors Based on Emerging Layered Semiconductors

by

Hongsuk Nam

A dissertation submitted in partial fulfillment
of the requirements for the degree of
Doctor of Philosophy
(Mechanical Engineering)
in the University of Michigan
2016

Doctoral Committee:

Assistant Professor Xiaogan Liang, Chair
Professor L. Jay Guo
Professor Katsuo Kurabayashi
Professor Wei Lu

Acknowledgments

First of all, I would like to express my deepest gratitude to my advisor, Professor Xiaogan Liang, for his invaluable guidance, support, and encouragement on my Ph.D. journey. He has always had an enthusiastic attitude about our research, bringing to it his keen observation, vision, and intuition, which has enabled me to strengthen valuable skills as an independent researcher. Moreover, he taught me not only as an academic advisor, but also a mentor for my life.

I would also like to extend my thanks to my committee members for spending their valuable time on my work and providing useful advice: Professor L. Jay Guo, Professor Katsuo Kurabayashi, and Professor Wei Lu.

I would like to thank all the collaborating students and Liang research group members for valuable discussions and support for my research and experiment. I was fortunate to meet such great colleagues during my Ph.D. program.

In particular, I am deeply grateful to my family, especially my parents, and parents-in-law for their unconditional support and love which made this dissertation possible. I express my warmest thanks to my beloved wife Bo-Ram Oh for her endless encouragement and love. She has been with me throughout my Ph.D. program as my best friend, mentor, and even collaborator of my research, which was tremendously helpful in ultimately finishing my Ph.D. program.

Table of Contents

Chapter 3 Multiple MoS_2 Transistor for Sensing Molecule Interaction Kinetics………………………………………………………………………………..41

List of Figures

List of Appendices

Abstract

Many important biomedical and clinical applications, such as early-stage cancer diagnosis, autoimmune disease treatment, and real-time monitoring of patients' immune status, demand new integrated multiplexing nanoelectronic/microfluidic biosensors. These biosensors are anticipated to enable fast (minute-scale) quantification of illness-related biomarkers, unprecedented detection sensitivity, fM-level limit-of-detection (LOD), and point-of-care capability. However, these new highly desirable biosensing capabilities have not been realized yet.

Atomically layered transition metal dichalcogenides (TMDCs) have gained a lot of attention because of their excellent electronic and structural properties. Especially, semiconducting TMDCs can serve as an essential complement to zero-band-gap graphene and enable novel semiconductor-related applications, such as thin-film transistors, phototransistors, and various types of sensors. More importantly, such TMDCs hold significant potential to be exploited for making new electronic biosensors and realize the highly desirable biosensing capabilities mentioned above. The research presented in this thesis sought to advance the scientific and technical knowledge for fabricating and

operating new TMDC-based electronic/microfluidic-integrated biosensors and realizing rapid fM-level quantification of biomarkers.

The first part (*i.e.*, the second chapter) is mainly focused on developing a top-down nanofabrication approach for producing orderly arranged, pristine few-layer MoS_2 flakes, which holds significant potential to be developed into a upscalable nanomanufacturing technology. The second part (*i.e.*, the third-to-fifth chapters) presents a systematic study on the biosensing characteristics of the TMDC-based transistor sensors fabricated using our nanoprinting techniques. First, multiple sets of MoS_2-based transistor biosensors were fabricated using our plasma-assisted nanoprinting method. Second, we studied the underlying device physics governing the response characteristics of TDMC transistor biosensors. Third, we further studied a cycle-wise method for operating MoS_2/WSe_2-based transistor biosensors to enable rapid, low-noise, highly specific biomolecule quantification at femtomolar levels.

The presented research has leveraged the superior electronic properties of emerging layered semiconductors for biosensing applications and advances label-free biosensing techniques toward realizing fast real-time immunoassay for low-abundance biomolecule detection. Moreover, the nanofabrication approaches developed in this research can be generally utilized for making other nanoelectronic devices based on emerging 2D layered materials, and the obtained device physics knowledge is anticipated to greatly leverage the excellent electronic and structural properties of TMDCs for other relevant sensing applications.

Chapter 1

Introduction

1.1 Emerging Two-Dimensional (2D) Atomically Layered Materials

Since Novoselov and Geim exfoliated graphene layers from highly oriented pyrolitic graphite (HOPG) for the first time using the mechanical cleavage method in 2004, great possibilities of two-dimensional atomically layered materials have opened up for research [1]. Graphene is a monolayer of carbon atoms with a two-dimensional (2D) honeycomb lattice, which has almost the same crystal energy as diamond [2]. Additionally, graphene has various extraordinary and attractive properties, such as ultrahigh carrier mobility at room temperature (~10,000 $cm^2 V^{-1} s^{-1}$) [1], high Young's modulus (~1 TPa) [3], and excellent thermal conductivity (3000-5000 $W m^{-1} K^{-1}$) [4]. These peculiar properties of graphene have motivated many researchers to develop a variety of applications in a broad range of device applications, such as electronics/optoelectronics [5-7], biomedicine [8, 9], sensors [10-16], and more.

Moreover, the success of graphene has inspired people to investigate other atomically layered materials, such as transition metal dichalcogenides [17], topological insulators [18], hexagonal boron nitrides [19], and layered metal oxides [20].

In comparison to the solid materials with zero-dimensional (0D), one-dimensional (1D), or three-dimensional (3D) morphologies, 2D nanomaterials provide several superior and unique characteristics. Especially in single-layer and few-layer forms, 2D layered materials exhibit a strong quantum confinement effect, which results in excellent electronic properties [21], such as Van Hove singularity points for high light absorption. Furthermore, 2D layered materials have other superb electronic properties. For example, owing to the high-quality crystal structure of graphene, the massless Dirac electrons in graphene can travel submicrometer distances without scattering, resulting in ultrahigh charge carrier mobility as mentioned above [22]. In addition, the atomically thin nature of 2D materials offers superb mechanical properties and high specific surface area. For example, the breaking strength and the ultimate tensile strength of graphene layers are 42 N m^{-1} and 120 GPa, respectively [23]. These standout properties of graphene indicate that graphene is one of the strongest materials today [3]. Moreover, the maximum Brunauer–Emmett–Teller (BET) surface area of graphene is 2630 m^2 g^{-1}, leading to very high electrocatalytic activity and ultrahigh loading capacity [24].

Another representative material is MoS_2, one of the transition metal dichalcogenides, which has mostly been explored recently. MoS_2 has a direct bandgap of ~1.8eV when it is in the single-layer form, and has an indirect bandgap of ~1.2eV in the bulk form [25]. Therefore, both monolayer and multilayer MoS_2 flakes can be exploited for semiconductor-related device applications and serve as a valuable complement to zero bandgap graphene structures. Additionally, the breaking strength, the in-plane stiffness, and the Young's modulus of MoS_2 layers are 15 N m^{-1}, 180 N m^{-1}, and 270 GPa, respectively, which are comparable to those of steel [26]. Further, MoS_2 has a high specific surface area of as high as 412 m^2 g^{-1} [27]. Exploiting these superior properties of 2D materials, there has been a broad range of potential device applications, including flexible electronics [28], solar cells [29], and surface-active applications owing to their high sensitivities from external stimuli, such as sensors [30-33], catalysis [34, 35], energy storage and conversion, and supercapacitors [36], *etc*.

1.2 Attractive Biosensing Properties of Semiconducting Transition Metal Dichalcogenides

All layered transition metal dichalcogenides (TMDCs) have a stratified crystal structure. The chemical formula of TMDCs can be generally expressed as MX_2, where M is the transition metal (*e.g.*, Mo and W), and X is a chalcogen atom (*e.g.*, S, Se, and Te), as illustrated in Figure 1.1 [37-39]. In a TMDC quintuple layer, the sub-layer consisting of transition metal atoms is sandwiched by two sub-layers consisting of chalcogen atoms that are covalently bonded together to form the quintuple layer. In a bulk TMDC material, multiple such quintuple layers are stacked together through the van der Waals interaction [40]. Multilayer MoS_2 has two types of stacking configurations: 2H-MoS_2 and 1T-MoS_2, as illustrated in Figure 1.2. The trigonal prismatic (2H) MoS_2 structure is thermodynamically stable and semiconductive, while the octahedral (1T) MoS_2 is thermodynamically unstable and metallic [41]. Attracted by their atomically thin structures and semiconducting properties (*e.g.*, MoS_2 and WSe_2), recently, many researchers have attempted to explore the applicability of semiconducting TMDCs for making biosensing devices [42-45].

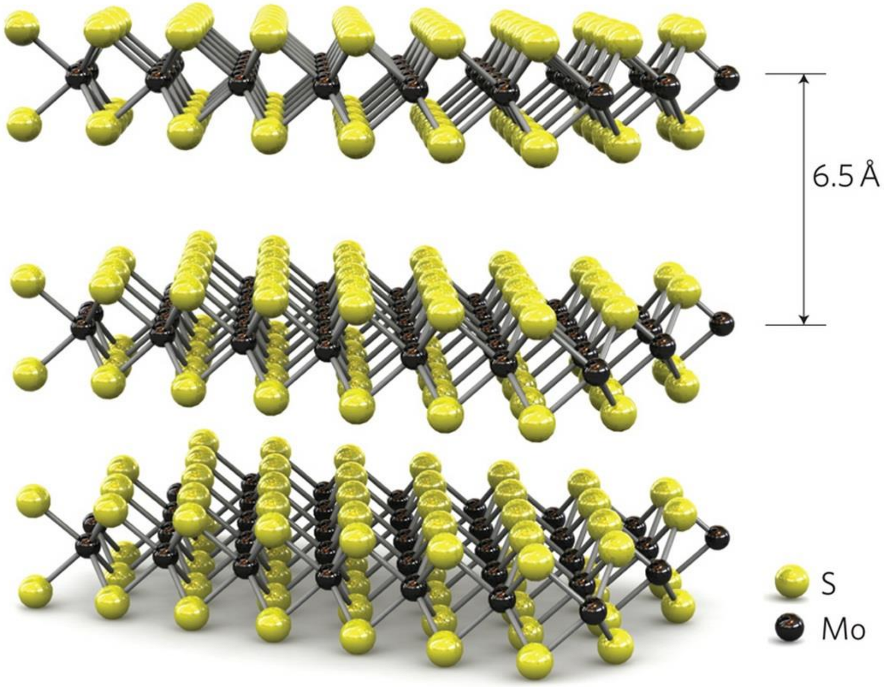

Figure 1.1 Three-dimensional schematic illustration of the MoS_2 structure. Courtesy of reference [25]

TMDCs have several appealing properties for biosensing applications. For example, pristine MoS_2 structures have high-quality 2D surfaces with an extremely low areal density of out-of-plane dangling bonds. Such 2D surfaces lead to very low probabilities for charged carriers to be scattered and trapped by surface defects, which results in a low electronic noise level and therefore a high signal-to-noise ratio for detecting the signals associated with biological events [43]. Additionally, due to the sizable bandgap and high specific surface area of monolayer and few-layer MoS_2

structures, MoS_2-based biosensors are anticipated to have a better biodetection sensitivity as compared to those based on bulk semiconductors and graphene. Moreover, MoS_2 and other TMDC layers have a very large mechanical strength as well as a superior flexibility, which could be exploited for making wearable and implantable biosensor devices. For example, a curvature radius down to 0.75 mm can be obtained in MoS_2 thin-film transistors with no observable degradation of their electrical performance [28]. Lastly, TMDCs show an excellent biocompatibility. In particular, through a series of biocompatibility tests, people have confirmed that MoS_2 exhibits a very low toxicity to most biological species as well as a high cell viability [46]. Such superior biocompatibility of MoS_2 is critical for making safe in-vivo TMDC-based biosensors in the near future.

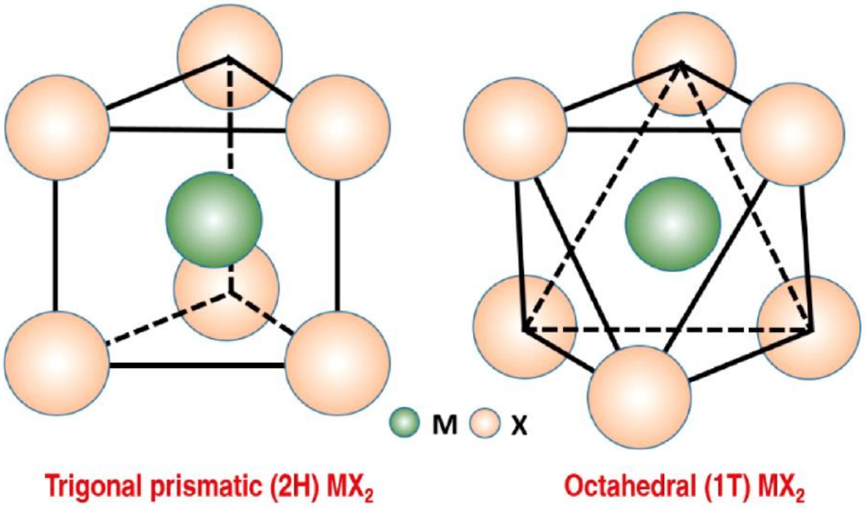

Figure 1.2 Unit cell structures of 2H-MX_2 and 1T-MX_2. Courtesy of reference [41]

1.3 Need of New Biosensing Technologies for Enabling Rapid Detection of Low-Concentration Illness-Related Biomarker Molecules

Cytokines are small secreted protein biomarkers released by immune cells, and they play very important roles in cell signaling and inflammatory response in the immune system (Figure 1.3). When pathogenic viruses or bacteria invade the immune system, the immune cells are activated and start to produce cytokines [47, 48]. Consequently, the concentration of different biomarkers indicates the development progress of target diseases. Therefore, the capability to detect and quantify low-concentration (femtomolar or single-molecule-level) biomarkers is critical for monitoring the development of immune responses at the early stage of a disease.

The current gold standard for detecting and quantifying biomarkers is enzyme-linked immunosorbent assay (ELISA). ELISA has commonly been used for both clinical and research purposes owing to its advantages, such as strong specificity, relatively high sensitivity, and safe environment for biomolecules. This method utilizes a plate-based assay with attached target biomolecules tagged with labels, and the signals from the labels are detected for quantification of the biomolecules. These labeling techniques require a long assay time because of a long sample preparation time and are not applicable for real-time detection of target biomolecules [48]. Additionally, ELISA processes need bulky instrument setups with large sample volumes, which hardly realize the point-of-care capability. To solve the listed challenges above, there is a strong need for new technology for enabling rapid label-free detection of low-concentration illness-related biomarker molecules.

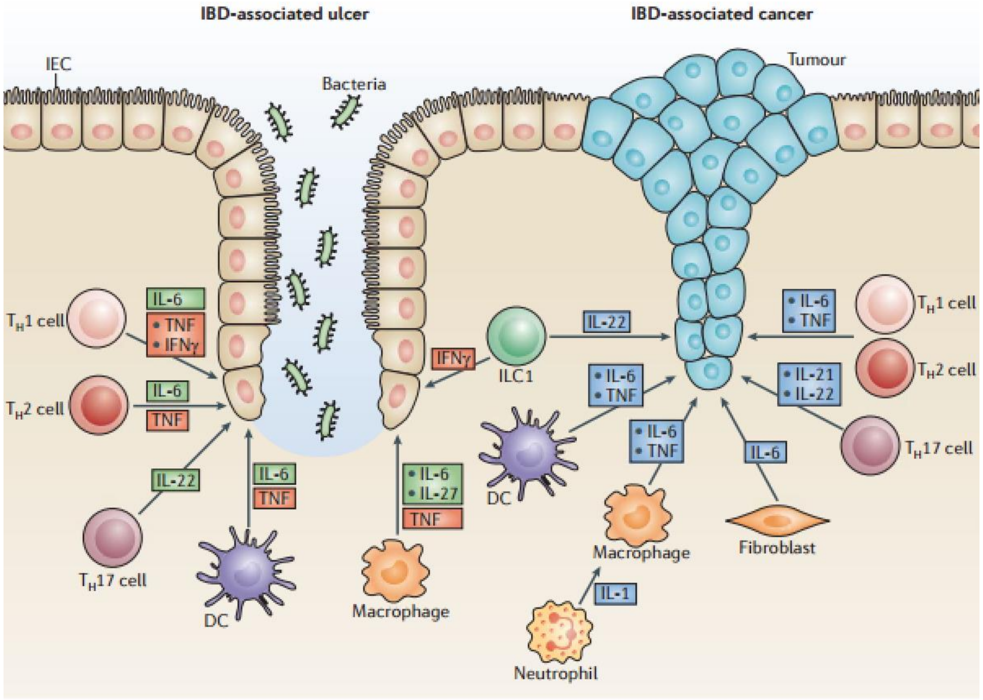

Figure 1.3 The role of cytokines during the pathogenic invasion. Courtesy of reference [47]

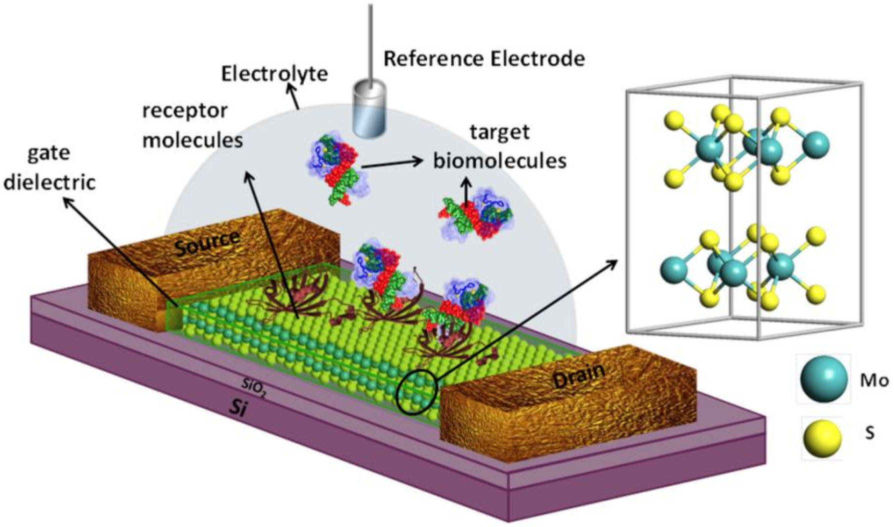

Figure 1.4 Schematic figure of MoS_2-based FET biosensor. Courtesy of reference [43]

1.4 Nanoscale Field-Effect-Transistor Biosensors for Realizing Rapid, Label-Free, Multiplexing Biomarker Quantification at fM-Level Detection Limits and New Opportunities of Emerging 2D Layered Semiconductors

Field-effect-transistor (FET) biosensors have gained a great deal of attention for severals years, and they have been demonstrated to be able to enable high biodetection sensitivity as well as label-free quantification capability. Additionally, FET biosensors can be integrated with portable electrical circuits and therefore enable point-of-care capability [49].

Among various types of nanomaterial structures, one-dimensional (1D) FET biosensors, such as silicon nanowires (Si NWs) [50] and carbon nanotubes (CNTs) [51], have been widely studied due to their high biodetection sensitivities. Such high sensitivities are attributed to the electrostatically gated nanoscale FET channels, which are highly sensitive to biomolecule conjugation reactions. However, cost-effective manufacturing of orderly-arranged (or addressable) NW or CNT-based FET sensors is still a critical challenge, which has significantly hindered their practical applications. Specifically, using top-down nanolithography methods (*e.g.*, electron-beam lithography (EBL) and nanoimprint lithography (NIL)), people can produce uniform arrays of Si NW FET biosensors on silicon-on-insulator (SOI) substrates. However, such sensor fabrication processes are too expensive to be used for practical biosensing applications, The bottom-up methods for directly synthesizing 1D FET biosensor structures still suffers from poor ordering and uniformity of synthesized 1D nanostructures over large areas. In addition, the bottom-up fabrication of CNT-based FET biosensors needs special techniques capable of selecting semiconducting nanotubes and eliminating metallic ones (*i.e.*, the purity of semiconducting CNTs need to be higher than 99% for scale-up applications), which also significantly increases the complexity and cost of the fabrication of CNT FET biosensors [43].

To address the aforementioned challenges, researchers have started to investigate the applicability of two-dimensional (2D) nanomaterials, such as graphene and TMDCs, for making FET biosensors. Due to its atomically thin structure, graphene can be used to make highly sensitive sensing FETs, and the fabrication process is highly compatible with the state-of-the-art planar lithographic techniques, which is potentially suitable for scale-up applications. However, although many studies have been performed for developing graphene FET biosensors, the lack of a bandgap in graphene fundamentally leads to a low carrier modulation for graphene FET biosensors [43]. Therefore, new efforts have been performed to create and characterize FET biosensors based on semiconducting TMDCs (Figure 1.4), which also have atomically thin FET channel structures [42, 43, 49]. TMDC-based FETs (*e.g.*, those based on MoS_2 and WSe_2) exhibit high On/Off current ratios up to 10^8, which, in combination with the advantages already discussed in chapter 1.2, can be exploited for creating label-free, highly sensitive FET biosensors with low limit-of-detection (LOD). Wang *et al.* and Sarkar *et al.* recently fabricated MoS_2 FET biosensors with 100-400 fM LODs for a cancer marker protein, Prostate-specific antigen (PSA) and the standard streptavidin–biotin conjugation reaction, respectively [42, 43]. Although individual MoS_2 FET biosensors have been fabricated and exhibited very high biodetection sensitivities, the fabrication of multiple such sensors with consistent sensor response characteristics has not been realized. Additionally, in order to achieve the multiplexing biomarker quantification capability, people need to develop new nanofabrication approaches capable of incorporating uniform TMDC device structures into addressable device sites or ordered arrays.

1.5 Summary of Dissertation

To address the scientific and technical gaps discussed in chapter 1.4, I have finished a series of nanofabrication and device-oriented projects, which are presented in this dissertation. The whole dissertation is divided into two main parts: (1) new nanoprinting processes for generating arrays of few-layer TMDC device structures (Chapter 2), and (2) fabrication of multiple TMDC FET biosensors for rapid, low-noise, multiplexing biomarker quantification at fM-level detection limits (Chapter 3, 4, and 5).

In chapter 2, I present a novel approach for producing orderly arranged, pristine few-layer MoS_2 flakes, which holds significant potential to be developed into a generic nanomanufacturing technology for producing device structures based emerging layered materials. In this work, I have successfully demonstrated the transfer printing of MoS_2 flakes into ordered arrays over cm^2-scale areas. Further, the FETs made from as-printed MoS_2 flakes exhibit excellent transport properties (*e.g.*, On/Off current ratio: 10^5-10^7, field-effect mobility on SiO_2 gate dielectrics: 6 to 44 $cm^2/(V\ s)$) as well as a good uniformity of such transistor parameters over large areas.

In chapter 3, I present the demonstration of MoS_2-based transistor biosensors capable of detecting tumor necrosis factor – alpha (TNF-α) with detection limits as low as 60 fM. All sets of transistors exhibit consistent calibrated responses with respect to TNF-α concentrations, and they result in a standard curve, from which the equilibrium constant of the antibody-(TNF-α) binding pair is extracted to be $K_D = 369 \pm 48$ fM. Based on this calibrated sensor model, the time-dependent binding kinetics is also presented and the association/dissociation rates of the antibody-(TNF-α) pair are extracted to be $(5.03 \pm 0.16) \times 10^8\ M^{-1}s^{-1}$ and $(1.97 \pm 0.08) \times 10^{-4}\ s^{-1}$, respectively.

In chapter 4, two different physics principles for operating MoS_2 transistor biosensors are experimentally identified, which depend on antibody functionalization locations. If antibodies are functionalized on an insulating layer coated on a MoS_2 transistor, antibody-antigen binding events mainly modify the transistor threshold voltage, which can be explained by the conventional capacitor model. If antibodies are directly grafted on the MoS_2 transistor channel, the binding events mainly modulate the ON-state transconductance of the transistor, which is attributed to the antigen-induced disordered potential in the MoS2 channel.

In chapter 5, a cycle-wise method for operating emerging MoS_2/WSe_2-based transistor biosensors is studied to enable rapid, low-noise, highly specific biomolecule quantification at femtomolar levels. The cycle-wise detection approach can physically separate incubation, flushing, and electrical measurement steps in the device chamber and therefore avoid the liquid-solution-induced electrochemical damage, screening, and nonspecific adsorption to the sensor. This capability can improve the transistor sensor's durability, sensitivity, and specificity. Furthermore, the time-dependent response signals measured by the cycle-wise method exhibit lower noise as compared to those measured by the continuous detection method. These advantages in combination with the inherent high sensitivity of MoS_2/WSe_2-based biosensors allow for rapid biomolecule quantification at femtomolar levels by analyzing the initial slopes of time-dependent response curves. We demonstrate the cycle-wise quantification of streptavidin and interleukin 1 beta in pure and complex solutions with detection limit ~ 1 fM and a total incubation time less than 20 min.

Chapter 2

MoS_2 Transistors Fabricated via Plasma-Assisted Nanoprinting of Few-Layer MoS_2 Flakes into Large-Area Arrays

2.1 Introduction

Molybdenum disulfide (MoS_2) belongs to the family of layered transition metal dichalcogenides [37]. It has been broadly used as a dry lubricant and as a catalyst for desulfurization in petroleum refineries [52]. Recently, MoS_2 attracted a great deal of attention because of its attractive electronic, optoelectronic, and mechanical properties [25, 28, 53, 54]. In the bulk form, MoS_2 is an indirect band-gap semiconductor with an energy gap of ~1.2 eV [54]. In the monolayer form, MoS_2 has a large direct band gap (~1.8 eV) [54]. Therefore, MoS_2 can serve as an important complement to zero-band-gap graphene and enable new semiconductor-related applications of two-dimensional (2-D) materials such as thin-film transistors [25, 55], phototransistors [56], chemical sensors [57], integrated circuits [58], and thin-film light-emitting diodes [54, 59]. As a 2-D nanoelectronic material, MoS_2 is advantageous over bulk Si for suppressing the undesirable tunneling between drain and source regions at the scaling limit of transistors and therefore provides benefits for miniaturization of electronic devices beyond Moore's law. In addition, bulk (or multilayer) MoS_2 shows relatively high in-plane carrier mobility comparable to that of crystalline Si [60], as well as robust mechanical and chemical properties, which makes it an attractive material for making flexible electronic devices with high performance and long lifetime [28, 58, 61]. A broad variety of prototype devices based on few layer MoS_2, such as high-performance field effect transistors [25, 55], phototransistors [56], sensors [33, 57], and integrated circuits [58], have been fabricated and extensively studied in research laboratories. However, the scale-up applications of MoS_2, especially the mass production of commercially feasible products, require large arrays of orderly arranged MoS_2 structures. This requirement breaks down into two critical challenges in nanomanufacturing: (1) incorporating pristine MoS_2 films over large areas and (2) patterning MoS_2 into ordered micro- and nanostructures over large areas to obtain both desirable electronic properties and required functionality. Several approaches have been attempted to produce MoS_2 materials for large-area applications, including Scotch tape exfoliation [1, 25, 61], liquid phase exfoliation in an organic solvent [62, 63], intercalation followed by forced hydration [59, 64, 65], transition metal sulfurization [66, 67], thermal decomposition of thiosalts [68], chemical vapor deposition (CVD) [69, 70], van der Waals epitaxial growth [71], etc. So far, a few efforts have been developed on the lithographic patterning of MoS_2 sheets and the deposition of MoS_2 crystals into ordered arrays [72-74]. All of these technologies for producing MoS_2 structures still suffer from one or more obstructions that prevent the creation of ordered, pristine MoS_2 device arrays over large areas. In particular, Scotch tape-based or liquid-phase exfoliation-based processes usually create a poor yield of few-layer MoS_2 flakes [1, 25, 61, 62]. Chemical intercalation methods can produce a relatively high yield of monolayer or few-layer MoS_2 flakes in colloidal solutions, but cannot arrange them into ordered arrays over large areas [59, 64, 65]. CVD and epitaxial methods are promising to generate very thin MoS_2 flakes over large areas in the future, but the present as-grown MoS_2 samples still feature randomly distributed micro- or nanoflakes with 10's-100's nm scale crystalline domains that are much smaller than the crystalline domains achieved in geographic MoS_2 materials (typically, 1 to 100's μm size) [37, 69-71]. Obviously, a nanomanufacturing technology capable of being scaled up and producing ordered and pristine few-layer MoS_2 patterns would have a transformative impact on future manufacturing of MoS_2 electronic and optoelectronic devices and systems.

In this chapter, we present novel transfer-printing processes for generating large-area arrays of prepatterned few-layer MoS_2 features. In this work, bulk MoS_2 films are prestructured with relief patterns by using lithographic techniques and subsequently serve as stamps for printing out MoS_2 flakes on pristine and plasma-charged SiO_2 substrates. Here, SiO_2 is chosen as the substrate material, because SiO_x-based substrates are widely used for electronic applications. Therefore, the approaches developed in this work can be generally applied to other SiO_x-based substrates such as glass, fused silica, and flexible silicone rubber. The few-layer MoS_2 flake pixels printed on such SiO_x substrates can be used to create working transistors showing excellent performance. In the future, the presented printing approaches in combination with other nanolithography techniques, precise deposition and etching processes, and new high-k gate dielectrics can potentially be employed for producing high performance MoS_2-based large-scale integrated circuits.

2.2 Methods and Materials

2.2.1 Prepatterning of Bulk MoS_2 Stamps

To fabricate a bulk MoS_2 stamp, a piece of bulk MoS_2 is mechanically exfoliated from a MoS_2 source sample (SPI, Inc., size ~1 cm^2) and firmly attached onto a bendable copper tape. The exfoliated MoS_2 film has a fresh and pristine surface with total area of ~1 cm^2. To pattern microscale relief features on the bulk MoS_2, a 1.4 μm thick photoresist layer is spun onto the MoS_2 surface and exposed on a Karl Suss MA6 photoaligner. The photomask used for this work bears periodic pillar patterns with pillar diameters ranging from 3 to 10 μm. After development, 100 nm thick Ti masks are formed on the MoS_2 surface by using electron-beam evaporation followed with lift-off in acetone. Afterward, the Ti mask patterns are etched onto the underlying MoS_2 using a SF_6- based RIE recipe (i.e., SF_6 flow rate 20 sccm, pressure 20 mTorr, power 200 W) with an etching rate of ~100 nm/min. Finally, the Ti masks are removed by soaking the MoS_2 film in a diluted HF acid solution.

2.2.2 Transfer Printing of Prepatterned MoS_2 Flakes onto Substrates

Prepatterned few-layer MoS_2 flakes are transfer printed onto SiO_2/Si substrates that are cleaned by using the standard RCA process. To perform a transfer printing, a bulk MoS_2 stamp and a SiO_2/Si substrate are firmly pressed to each other by using a lab-made pressing system that can generate a gauge pressure up to 3 MPa for contact printing. To improve the bonding strength between the MoS_2 flakes and the SiO_2 surface, an O_2-based plasma recipe (i.e., O_2 flow rate 50 sccm, pressure 25 mTorr, power 100 W, time duration 2 min) is used to treat the SiO_2 surface before the printing step. Such a plasma treatment is expected to introduce uniformly distributed electric charges on the SiO_2 surface that can provide additional electrostatic attractive stress for exfoliating prepatterned few-layer MoS_2 flakes from the bulk stamp [75]. After the printing process, the printed MoS_2 patterns are imaged by using a scanning electron microscope in secondary electron and backscattered modes as well as an optical microscope. An atomic force microscope is employed to measure the thickness of printed MoS_2 features in the tapping mode. Furthermore, an X-ray energy dispersive spectrometer integrated with a SEM system is used to confirm the presence of MoS_2 features within the printed areas.

2.2.3 Fabrication of Field-Effect Transistors Using Printed MoS_2 Flakes

To fabricate back-gated MoS_2 FETs, the metallic drain/source contacts (5 nm Ti/55 nm Au) are fabricated by photolithography or electron-beam lithography followed by metal deposition and lift-off. Especially, photolithography is used for fabricating FETs based on the inner flakes of MoS_2 pixels, and EBL is specifically used for fabricating FETs based on the outer edge ribbons of MoS_2 pixels. Finally, another metallic contact is made onto the p^+-Si substrate, which serves as a back gate contact. The device characteristic curves of FETs are measured using an Agilent-4145B semiconductor parameter analyzer.

2.2.4 Plasma-Assisted Transfer Printing of Prepatterned Graphene Nanoribbons

First, a highly oriented pyrolytic graphite stamp (SPI, Inc.) is prepatterned with 100 nm half-pitch, 100 nm deep relief gratings. Such grating features are replicated from a master mold (Nanonex, Inc.) by using thermal nanoimprint lithography (T-NIL) followed by O_2-based plasma etching [76]. The T-NIL process was performed on a Specac thermal pressing tool equipped with a cooling-water system. The fabricated HOPG stamp is subsequently used to stamp out graphene nanoribbons onto plasma-charged SiO_2 substrates. The plasma-assisted printing process performed here is the same as the process used for printing microscale MoS_2 pixel arrays.

2.3 Results and Discussion

2.3.1 Experimental Results of Plasma-Assisted Transfer Printing

Figure 2.1 (a) schematically illustrates our approach for transfer printing prepatterned MoS_2 flakes. The fabrication process includes the following steps. (1) The process starts with a piece of pristine bulk MoS_2. (2) Photolithography is performed to pattern a photoresist layer spin-coated on top of the MoS_2 surface. (3) Arrays of metal masks are created by depositing 100 nm Ti followed with lift-off in acetone. (4) SF_6-

based reactive ion etching (RIE) is performed to transfer the Ti mask pattern onto underlying MoS_2 [74, 77, 78]. (5) Ti masks are completely removed in hydrofluoric (HF) acid, and a bulk MoS_2 stamp is created. (6) A SiO_2 substrate is treated with O_2 plasma to generate electric charges on the surface [75]. (7) Finally, the bulk MoS_2 stamp is used for

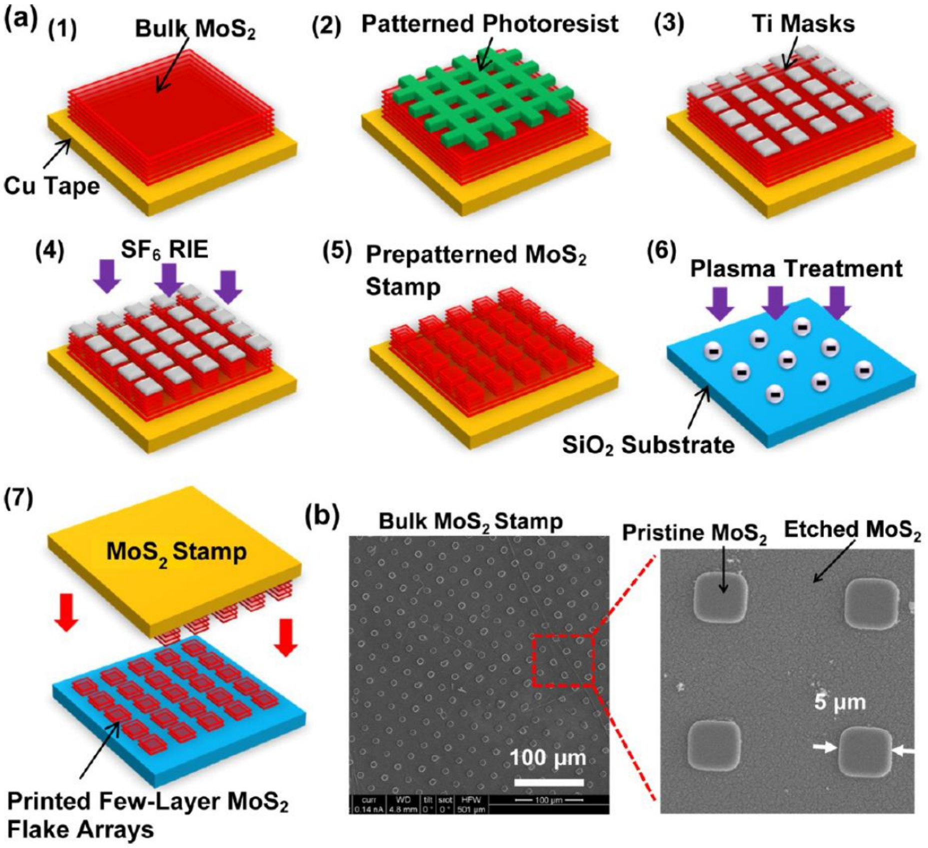

Figure 2.1 (a) Schematic flowchart of transfer printing of prepatterned few-layer MoS_2 flakes, which includes (1) initial bulk MoS_2 with a pristine surface; (2) photolithography for patterning device features; (3) formation of Ti masks by metal deposition followed by lift-off; (4) plasma etching of underlying MoS_2; (5) removal of Ti masks and finalization of a bulk MoS_2 stamp bearing relief features; (6) plasma treatment of the SiO_2 substrate; (7) direct transfer printing of prepatterned few-layer MoS_2 flakes onto the substrate. (b) SEM images of a bulk MoS_2 stamp prestructured with 5 μm size periodic pillars.

printing out MoS_2 flake arrays onto the SiO_2 substrate. This process can create MoS_2 device patterns directly from pristine geographic MoS_2 materials that have the largest crystalline domains (typically, 1 to 100's μm size) and the best electronic properties to date [37, 69-71]. Moreover, this approach can be generalized for manufacturing other emerging atomically layered nanomaterials such as graphene [79-81], boron nitride [82, 83], and topological insulator thin films [84]. It should be noted that such a plasma-assisted transfer-printing process is significantly advantageous over voltage-based electrostatic exfoliation methods previously developed by Liang *et al.* for generating atomically layered materials [80], in terms of application scope and printing uniformity.

In particular, plasma-assisted printing can be applied to any substrates with a dielectric layer, whereas voltage-based exfoliation processes can only be utilzed for conductive substrates. Furthermore, plasma-induced surface charges are usually immobilized and uniformly distributed over dielectric substrates and, therefore, result in uniform attractive stress for printing MoS_2 features over large areas. However, voltage-generated free charges are movable in the conductive substrate, and they tend to accumulate at locations with the smallest stamp/substrate gap, resulting in nonuniform electrostatic printing stress and a high risk of electrical leakage [80]. Figure 2.1 (b) shows scanning electron micrographs (SEMs) of an exemplary MoS_2 stamp prepatterned with 5 μm size, 600 nm high pillars. The zoomed view in Figure 2.1 (b) shows that the SF_6 plasma-etched area exhibits a relatively high roughness, which is attributed to plasma etching or ion bombardment. However, the raised pillar mesas protected by the Ti masks are still as smooth as a pristine MoS_2 surface. This should yield a conformal contact with the flat substrate during a mechanical printing process and therefore a high transfer-printing efficiency of MoS_2 flakes.

Figure 2.2 (a) and (c) display SEM images of MoS_2 flakes printed on a pristine SiO_2 surface. These images, captured over a large printed area (~1 cm^2), show that the mechanical printing process can create large-area, orderly paved arrays of MoS_2 pixel features. However, most of the printed pixels have relatively irregular edge profiles that

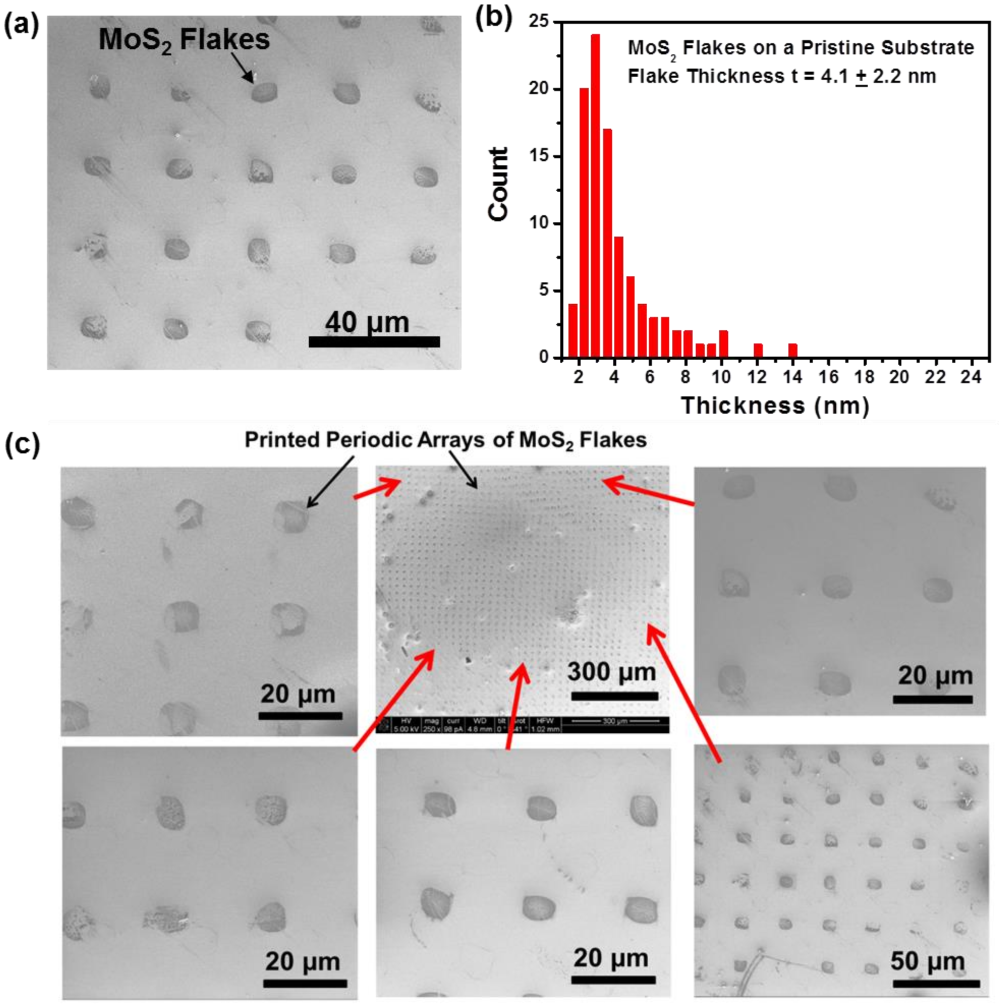

Figure 2.2 (a) SEM image of arrays of 10 μm size MoS_2 flake pixels printed onto a pristine SiO_2 substrate. (b) Stacked column chart of the average thickness data collected from 100 as-printed MoS_2 pixels. The thickness data were obtained from MoS_2 pixels printed over a~1cm^2 area by using an AFM. (c) SEM images of periodic arrays of 10 μm size MoS_2 flakes printed onto a pristine SiO_2 surface, which were acquired from different locations over the printed area, as indicated by the red arrows.

are not faithfully correlated to the edge profiles of pillars prestructured on the bulk stamp. The thickness data of MoS_2 pixels were obtained by using an atomic force microscope (AFM). For each of the printed MoS_2 pixels, the average flake thickness was extracted from AFM topographic data. Figure 2.2 (b) plots the statistical distribution of the average thickness data of 100 MoS_2 flake pixels of 10 μm size produced in a single transfer-printing cycle. Figure 2.2 (b) shows that the overall average flake thickness is measured to be 4.1 nm (~6 monolayers), and the standard deviation is 2.2 nm (~3 monolayers) over a ~1 cm^2 area. About 95% and 80% of printed MoS_2 flakes are thinner than 10 and 5 nm, respectively.

Figure 2.3 (a) shows an SEM image of MoS_2 patterns printed onto an O_2 plasma-charged SiO_2 substrate. Figure 2.4 lists more SEM images of MoS_2 patterns with various dimension sizes, which were captured from different locations over the printed area. These images show that the printing process on plasma-charged substrates can create large-area, orderly arranged arrays of MoS_2 flake pixels with a higher uniformity of pixel profiles in comparison with the printing result on a pristine substrate. In particular, MoS_2 pixel patterns feature clear, well-defined edge profiles that are faithfully correlated to the edge profiles of pillars prestructured on the bulk stamp. The zoomed image in Figure 2.3 (b) reveals that the clear edge profile of a MoS_2 pixel is indeed made up of a ring-shaped MoS_2 ribbon. Such outer edge ribbons of MoS_2 pixels have widths ranging from 200 to 400 nm. Besides these edge ribbon features, there are indeed thinner MoS_2 films or flakes located in the inner regions of printed pixels enclosed by the edge ribbons. These inner

MoS_2 flakes typically show a poor feature contrast in secondary-electron images. To enhance the SEM contrast, printed MoS_2 pixels were also imaged by detecting backscattered electrons (BSEs), as shown in Figure 2.3 (c-e), which are often used to detect contrast between areas with different chemical compositions. The BSE image contrast in Figure 2.3 (c-e) suggests the presence of thin MoS_2 flakes within each of the pixels.

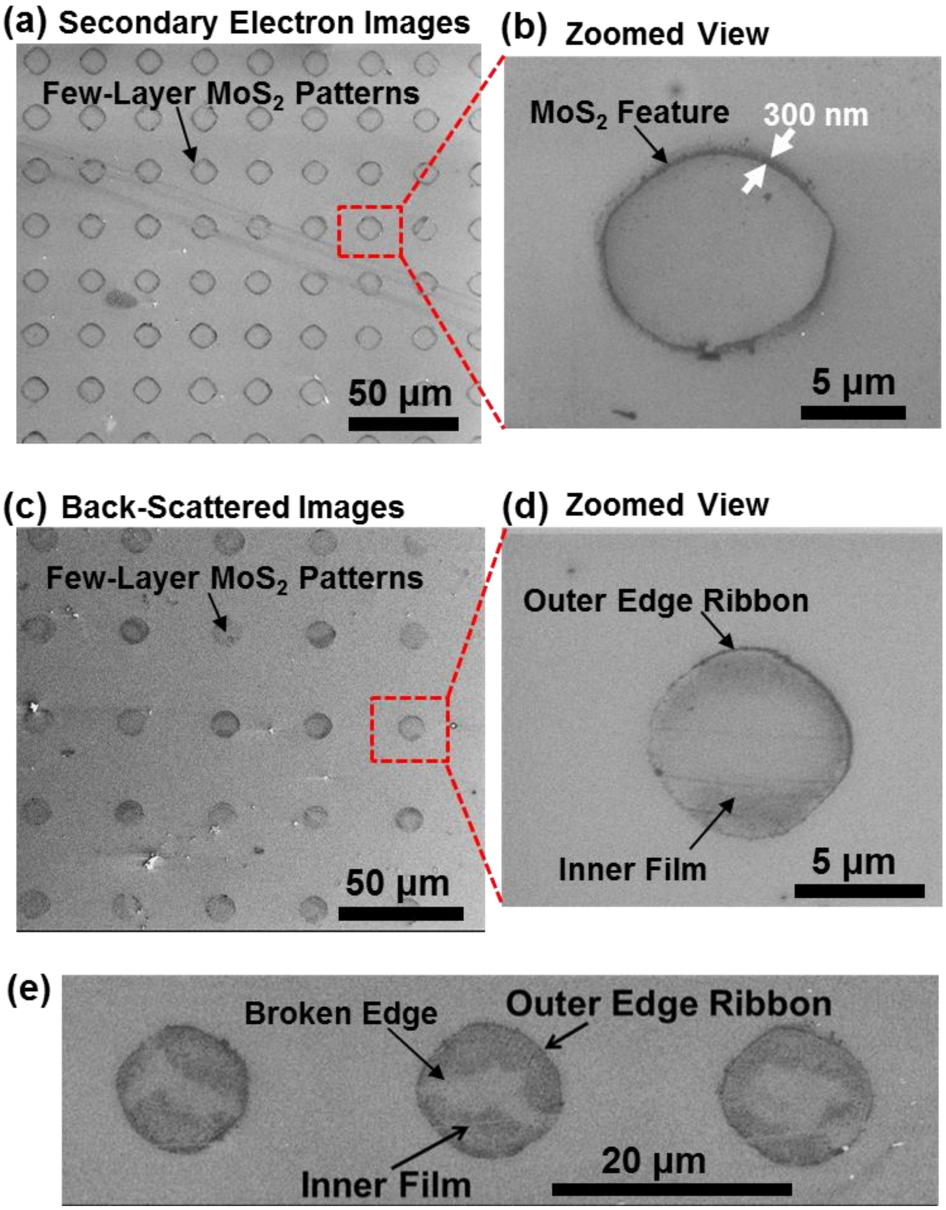

Figure 2.3 (a, b) Secondary-electron SEM images of MoS_2 pixel arrays printed onto an O_2 plasma-charged substrate, which exhibit clear, well-defined edge profiles faithfully correlated to the edge profiles of pillar features on the bulk MoS_2 stamps. (c, d) Backscattered SEM images of MoS_2 pixel arrays, which show the presence of thin inner MoS_2 flakes within each printed pixel. (e) Backscattered image of MoS_2 pixels with broken inner films.

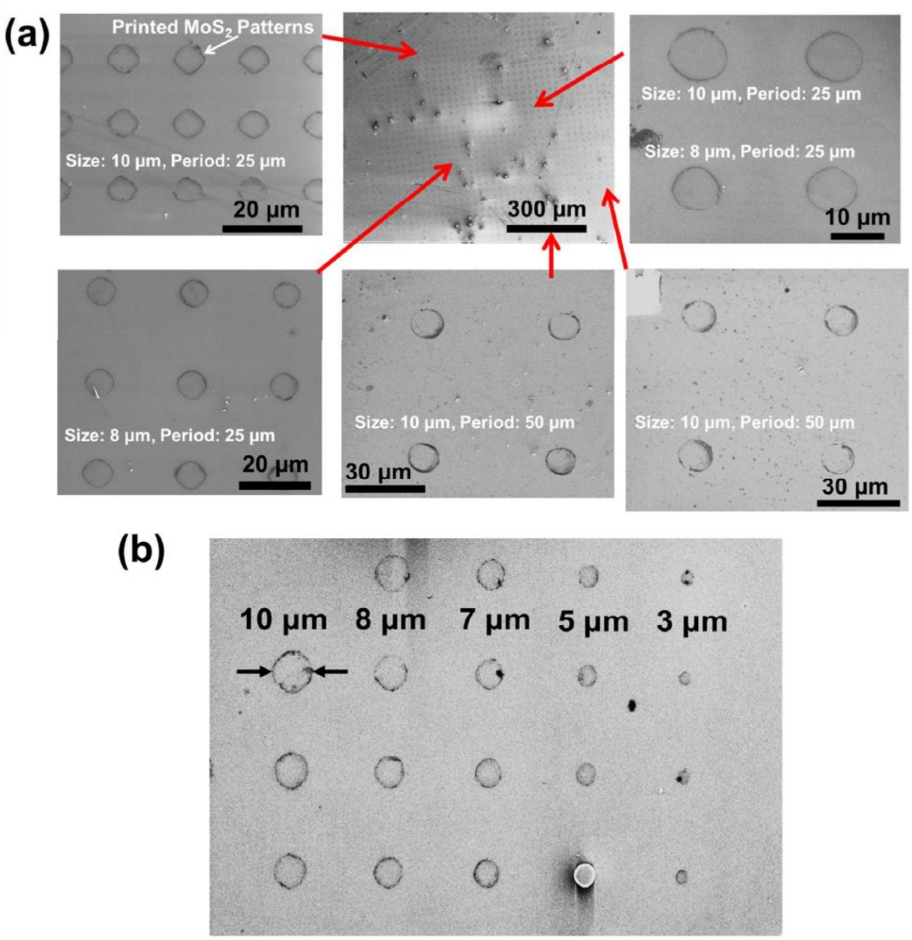

Figure 2.4 (a) SEM images of periodic arrays of MoS_2 patterns printed onto a plasma-charged SiO_2 surface, which were acquired from different locations over the printed area, as indicated by the red arrows. (b) SEM images of MoS_2 pixels with various feature sizes. All the MoS_2 features printed on the plasma-charged substrates exhibit clear, well-defined edge profiles that are faithfully duplicated from the edge profiles of the pillar features on the bulk MoS_2 stamps.

X-ray energy dispersive spectrometer (EDS) spectra were captured from the edge ribbons as well as the inner films of MoS_2 pixels, as shown in Figure 2.5. The EDS results confirm the presence of sulfur and molybdenum in both the edge and inner portions of printed pixels. Additionally, Figure 2.6 exhibits optical micrographs of printed MoS_2 pixels on a 330 nm thick SiO_2 substrate, and the feature contrast further confirms the presence of inner flakes within printed MoS_2 pixels. The spatial variation of BSE image contrast and the EDS intensity of MoS_2-associated peaks propose an interpixel variation of MoS_2 flake thickness over the printed substrate. To obtain the inner flake thickness data, MoS_2 pixels with partially broken inner films (*e.g.*, the pixels shown in Figure 2.3 (e) and Figure 2.6 (c)) were imaged by using AFM, and the thickness of an inner MoS_2 flake was measured from its broken edges.

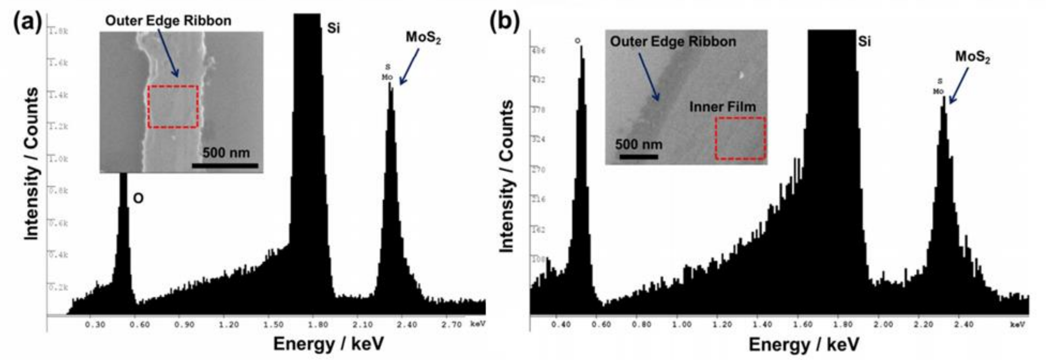

Figure 2.5 X-ray energy dispersive spectrometer (EDS) spectra of (a) the outer edge ribbon of a printed MoS_2 pixel and (b) the inner flake of a MoS_2 pixel. The dashed red squares in the inset SEM images indicate the locations on the samples where the EDS spectra were obtained. The EDS results further confirms the presence of sulfur and molybdenum in both the edge and inner portions of printed MoS_2 pixels.

Figure 2.7 (a) displays an AFM image of an exemplary MoS_2 pixel consisting of a relatively thick edge ribbon and broken inner flakes. The scan line denoted by the solid line and accordingly plotted in Figure 2.7 (b) explicitly exhibits that the thickness values measured at the left and the right sides of this outer edge ribbon are 7 nm (~11 monolayers) and 8 nm (~12 monolayers), respectively; the thickness of the broken inner flakes is measured to be 2.4 nm(~4 monolayers). The thickness data acquired from 10 scan lines are used to calculate the average thickness of the inner film and the outer edge

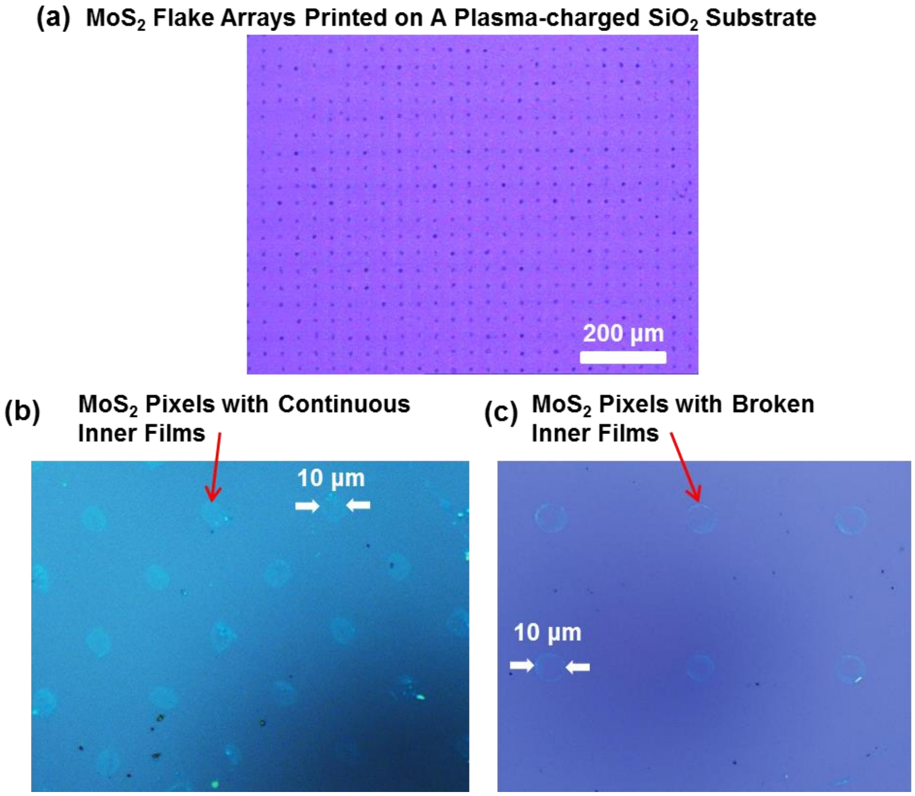

Figure 2.6 Optical micrographs of printed MoS_2 pixel arrays on a 330 nm thick SiO_2 substrate: (a) a low-magnification view; (b) a zoomed view of printed pixels with continuous inner films; (c) a zoomed view of printed pixels with broken inner films. All printed pixels exhibit regular edge profiles faithfully duplicated from prepatterned pillars on the bulk MoS_2 stamps.

ribbon of an individual MoS_2 pixel. Figure 2.7 (c) plots the statistical distribution of the average thickness data of 100 MoS_2 pixels printed on a plasma-charged substrate. Here, the thickness data of inner films (solid columns) and outer edge ribbons (blue hatched columns) of MoS_2 pixels are separately plotted. Figure 2.7 (c) shows that the overall average thickness of outer edge ribbons is 17 nm (~26 monolayers) with a standard deviation of 3 nm (~5 monolayers), whereas the overall average thickness of inner films is 3.0 nm (~5 monolayers) with a standard deviation of 1.9 nm (~3 monolayers). About 90% of inner flakes of MoS_2 pixels printed on a plasma-charged SiO_2 substrate are thinner than 5 nm (~8 monolayers). On the basis of such SEM, AFM, EDS, and optical micrograph characterizations, it is concluded that microscale MoS_2 pixels printed on a plasma-charged SiO_2 surface feature relatively thinner inner films or flakes enclosed by relatively thicker ring-shaped edge ribbons and a higher percentage yield of few-layer MoS_2 flakes thinner than 5 nm in comparison with pixels printed on a pristine SiO_2 substrate.

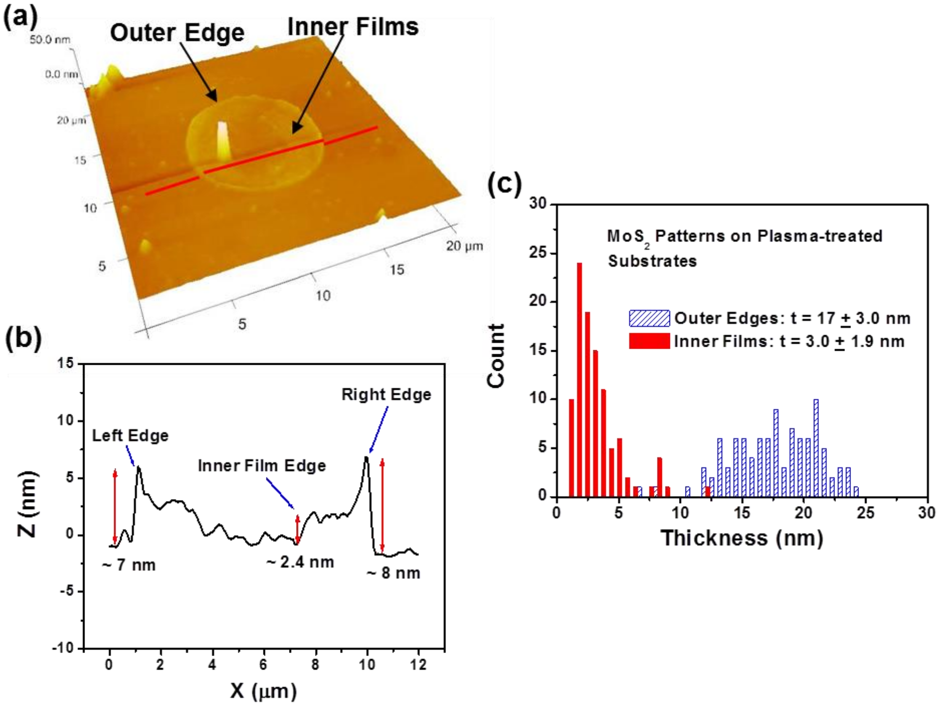

Figure 2.7 (a) AFM image of a 10 µm size MoS$_2$ pixel printed on a plasma-charged SiO$_2$ substrate. The solid line indicates a scanning trace across the pixel, which is explicitly plotted in (b). (c) Stacked column chart of the average thickness data collected from 100 as-printed MoS$_2$ pixels. Here, the thickness data acquired from the inner flakes (solid columns) and the outer edge ribbons (hatched columns) of these MoS$_2$ pixels are separately plotted.

Although plasma-assisted printing can produce large-area arrays of microscale MoS$_2$ pixels with regular edge profiles, many pixels have broken areas in their central regions, as shown in Figure 2.3 (e) and Figure 2.6 (c). This can be attributed to several possible reasons, including the limited size of crystalline domains in bulk MoS$_2$, nonuniformity of attractive stress within a microscale MoS$_2$ pixel mesa, as discussed in the simulation analysis, and the paradigm rule that the direct exfoliation of a large-area atomic layer (e.g., a complete microscale MoS$_2$ pixel film free of defects) is thermodynamically unfavorable. Such an analysis suggests that it is indeed desirable to prepattern bulk MoS$_2$ stamps with densely arranged nanostructures that can enhance the printing fidelity and eliminate the defects in the middle of printed patterns. In addition, such relief nanostructures are expected to generate a higher fringe field during printing processes because of the higher density of sharp feature edges and result in the higher transfer-printing efficiency of MoS_2 features. So far we have not developed a scalable process for patterning nanostructures on bulk MoS_2 because of its overly rough surface. However, we and other groups have successfully realized the nanopatterning of highly oriented pyrolytic graphite (HOPG) stamps with 100 nm half-pitch gratings using nanoimprint lithography, as shown in Figure 2.8 (a) [76, 85]. Figure 2.8 (b) shows SEM images of 100 nm half-pitch graphene nanoribbons (GNRs) produced by using plasma-assisted transfer printing. The printed GNRs exhibit a high degree of uniformity in ribbon widths over large areas and do not exhibit any visible defects in the middle of individual ribbons. The thickness of GNRs was measured to be 2.0 ± 1.0 nm by using an AFM. This work demonstrates that (1) nanoscale defect-free atomic layer patterns can be more easily produced by using plasma-assisted printing in comparison with microscale ones; (2) plasma-assisted printing can be generalized for producing high quality nanostructures of other atomically layered materials.

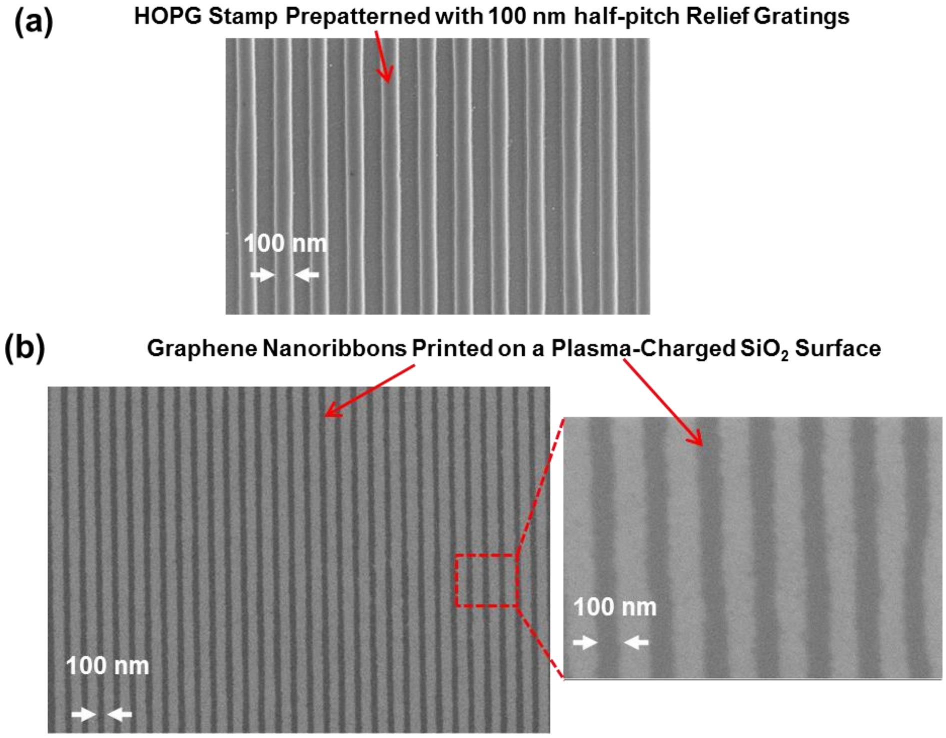

Figure 2.8 SEM images of (a) a HOPG stamp prepatterned with 100 nm half-pitch relief gratings by using nanoimprint lithography followed with plasma etching and (b) graphene nanoribbons printed onto a plasma-charged SiO_2 substrate.

2.3.2 Maxwell Stress Tensor Calculation

To obtain a preliminary understanding of plasma-assisted printing mechanisms responsible for the resultant morphology of MoS_2 pixels, Maxwell stress tensor calculation was performed and used for evaluating the distribution of surface charge-induced electrostatic attractive stress between the bulk MoS_2 stamp and the dielectric substrate [86, 87]. Figure 2.9 (a) illustrates the 2-D model for the calculation, in which a plasma-charged SiO_2 substrate is in contact with a bulk MoS_2 stamp and the surface charge density is arbitrarily set to 0.05 C/m^2 (currently we lack experimentally measured data of surface charge densities). Figure 2.9 (b) plots the calculated attractive stress exerted by the plasma-charged SiO_2 substrate on the bulk MoS_2 stamp as a function of positions. Figure 2.9 (c) shows the zoomed view of the attractive stress distribution within a single MoS_2 mesa in contact with a SiO_2 surface. It is found that the attractive stress acting on a microscale MoS_2 mesa is uniform in the central region of the mesa but is significantly increased along the mesa edges due to the fringe effect. During a transfer printing process, such high attractive stress at the mesa edges is expected to result in the exfoliation of MoS_2 flake pixels with well-defined edges, as experimentally demonstrated. In addition, the strong electric field at the MoS_2/SiO_2 interface is expected to influence dispersion and dipole interactions of atoms there and therefore change the cohesive energy of MoS_2 layers close to the SiO_2 surface [88, 89]. This could lead to a dependence of the number of printed MoS_2 monolayers on the field magnitude, which could qualitatively explain our experimental result that for MoS_2 pixels printed on plasma-charged substrates the edge portions are statistically thicker than the inner flakes, as shown in Figure 2.7 (c). Our future theoretical simulation work will incorporate quantum mechanics, molecular simulations, and experimentally measured surface charge data to quantitatively analyze the effects of electric field on the number of printed MoS_2 monolayers.

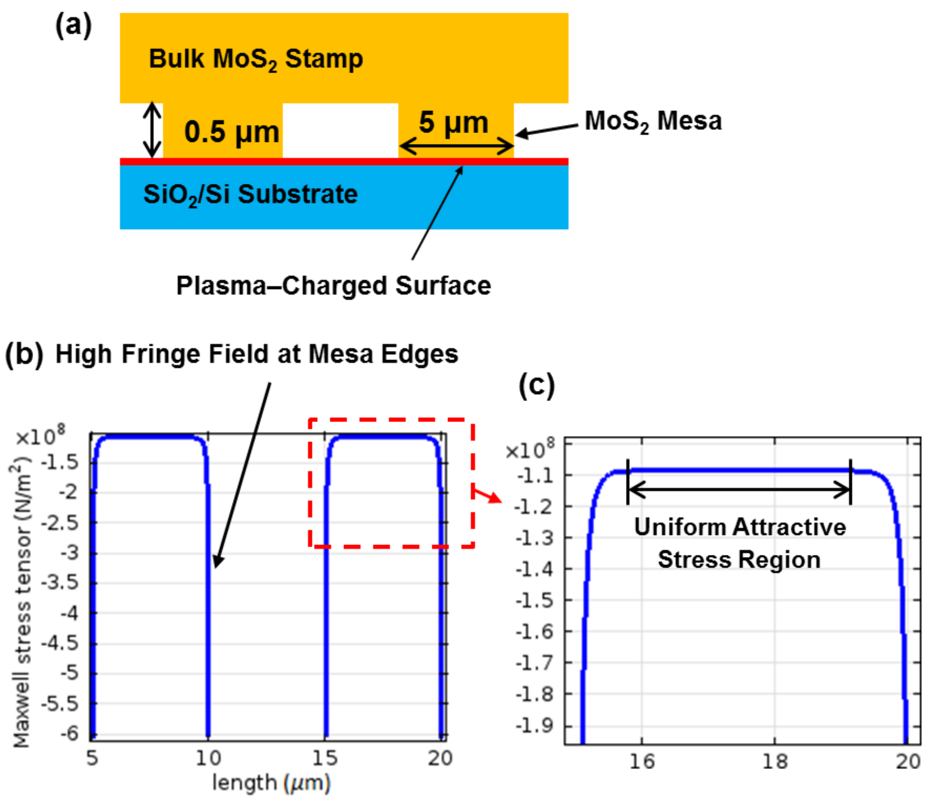

Figure 2.9 (a) Illustration of the 2-D model for Maxwell stress tensor calculation of surface charge-induced electrostatic attractive stress between the bulk MoS_2 stamp and the dielectric substrate. (b) Calculated attractive stress plotted as a function of positions. (c) Zoomed view of attractive stress distribution within a single MoS_2 mesa in contact with a SiO_2 surface. It is found that the attractive stress acting on a microscale MoS_2 mesa is uniform in the central region of the MoS_2 mesa but is significantly increased along the mesa edges due to the fringe effect.

2.3.3 Field-Effect Transistors (FETs) Made from Printed MoS_2 Flakes

To evaluate the electronic properties of printed MoS_2 flakes, we fabricated field-effect transistors (FETs) using MoS_2 pixels printed on plasma-charged SiO_2/p^+ Si substrates. Figure 2.10 (a) shows a BSE image of an inner flake of a MoS_2 pixel that was used to fabricate a back-gated FET with flake thickness of ~5 nm, channel length of L =

5.4 µm, average channel width of $W \approx 3.7$ µm, and gate dielectric thickness of $d = 330$ nm. Figure 2.10 (b) plots drain-source current (I_{DS}) versus drain-source voltage (V_{DS}) characteristics of this exemplary FET under different gate voltages (V_G) ranging from -75 to 100 V. Figure 2.10 (c) plots the I_{DS}-V_G characteristics under a fixed drain-source voltage ($V_{DS} = 10$ V). As shown in Figure 2.10 (b) and (c), this FET displays n-type conduction with an ON/OFF current ratio (I_{ON}/I_{OFF}) of ~10^7. The transconductance at the linear region of the I_{DS}-V_G characteristic curve was obtained as $dI_{DS}/dV_G = 1.60$ µS by the linear fitting (denoted with the red solid line in the inset of Figure 2.10 (c)). The field-effect mobility was estimated to be $\mu = 22$ cm^2/(V s) by using equation (1) (valid for the linear region of MoS_2-based FETs with microscale channel widths), where ε_0 is the vacuum permittivity, $\varepsilon_r \approx 3.9$ is the dielectric constant of SiO_2, C_{ox} is the gate capacitance, and W/L is the width/length ratio of the MoS_2 flake channel. The field-effect mobility values obtained from other FETs made from the inner flakes of printed MoS_2 pixels range from 6 to 44 cm^2/(V s), which are comparable to the highest mobility values previously reported for MoS_2 FETs using SiO_2 as the gate dielectric [61, 90]. This indicates that our transfer-printing approaches can produce high-quality MoS_2 features and are suitable for practical nanoelectronic applications.

$$\mu = \frac{\Delta I_{DS}}{C_{ox}\frac{W}{L}V_{DS}\Delta V_G} \qquad C_{ox} = \frac{\varepsilon_0 \varepsilon_r}{d} \qquad (1)$$

We also fabricated FETs using the ring-shaped edge ribbons of MoS_2 pixels as the semiconducting channels. To make an edge ribbon-based FET, electron-beam lithography (EBL) followed by metal evaporation and lift-off was performed to fabricate drain and source electrodes precisely aligned to the specific segment of the edge ribbon of a MoS_2 pixel. In EBL, the overlay alignment was carefully performed to avoid incorporating any inner pixel flakes into the FET channel. Figure 2.11 (a) shows an SEM image of an exemplary edge ribbon-based FET with a channel width of $W \approx 300$ nm, channel length of $L \approx 500$ nm, and average MoS_2 thickness of ~10 nm. Figure 2.11 (b) and (c) displays I_{DS}-V_{DS} and I_{DS}-V_G characteristics, respectively, which show that this edge ribbon-based FET exhibits p-type conduction for V_G = -100 to 100 V. The transconductance at the linear region of the I_{DS}-V_G characteristic curve was obtained as $dI_{DS}/dV_G = -1.74$ nS by the linear fitting (denoted with the red solid line in the inset of Figure 2.11 (c)). The field-effect mobility was estimated to be $\mu = 0.27$ cm^2/(V s) by using equation (2), where C_g is the average gate capacitance associated with a single MoS_2 edge ribbon per unit channel length [unit: F/m]. Here, C_g is calculated by using a simulation model based on finite element analysis that takes into account the fringe effect at the MoS_2 nanoribbon edges, as shown in Appendix A. Such a fringe effect can significantly affect the values of C_g for MoS_2 FETs with nanoscale channel widths. The field-effect mobility values measured from other edge ribbon-based FETs range from 0.1 to 1.0 cm^2/(V s). The p-type conduction is generally observed in other edge ribbon-based FETs, and it is attributed to the chemical doping to the edge portions of MoS_2 pixels, which might be induced during the SF_6 RIE process for patterning pillars in bulk MoS_2 stamps.

$$\mu = \frac{L}{C_g V_{DS}} \left(\frac{dI_{DS}}{dV_G} \right) \qquad (2)$$

Our current printing approaches can generate few-layer MoS_2 flakes with the change of thickness mainly in the range 0.7-10 nm on a pristine SiO_2 substrate (Figure 2.2 (b)) or 0.7-5 nm on a plasma-charged substrate (Figure 2.7 (c)). As-printed MoS_2 pixels with such flake thickness distributions over large areas are still suitable for scale-up transistor-based electronic applications (if not for all applications), because previous works have demonstrated that FETs made from multilayer MoS_2 flakes with thicknesses

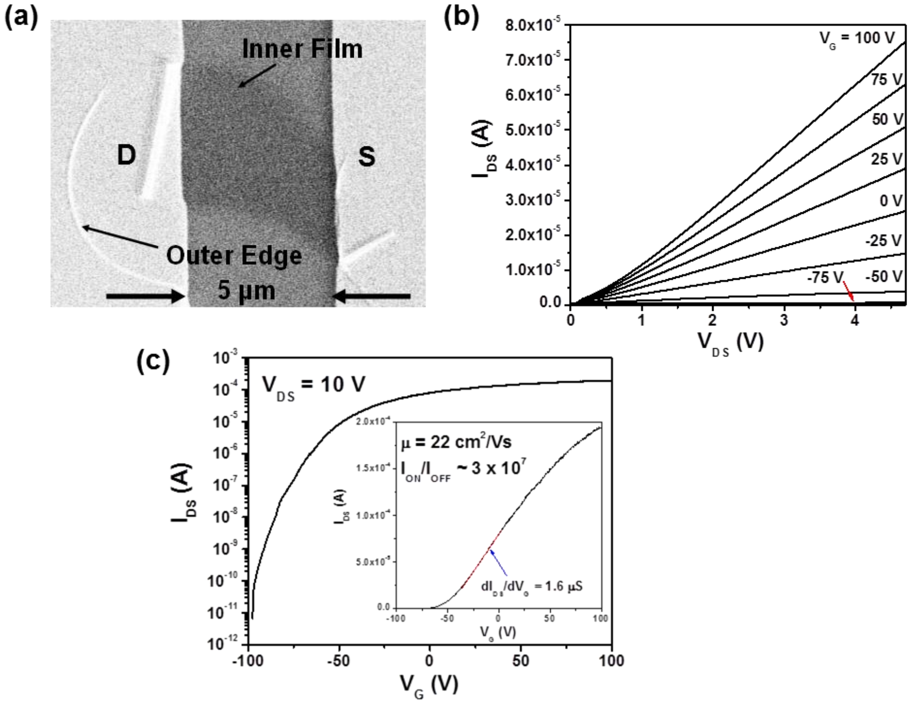

Figure 2.10 (a) BSE image of an exemplary back-gated FET made from the inner flake of a printed MoS_2 pixel with flake thickness of~5 nm, channel width of~3.7 μm, channel length of~5.4 μm, and gate dielectric (SiO_2) thickness of 330 nm, in which Ti/Au contacts were deposited as drain (*D*) and source (*S*) contacts and the p^+ silicon substrate serves as a back gate. (b) I_{DS}-V_{DS} characteristics under different gate voltages (V_G) ranging from -75 to 100 V. (c) Semilogarithmic plot of an I_{DS}-V_G characteristic curve under a fixed drain-source voltage V_{DS} = 10 V, which exhibits an ON/OFF current ratio (I_{ON}/I_{OFF}) ≈ 10^7. The inset graph shows the linear plot of the same I_{DS}-V_G curve, and the transconductance (dI_{DS}/dV_G) is obtained by fitting the linear region of the I_{DS}-V_G curve, as indicated by the red line. The field-effect mobility is subsequently extracted to be μ = 22 $cm^2/(V\ s)$ for this FET.

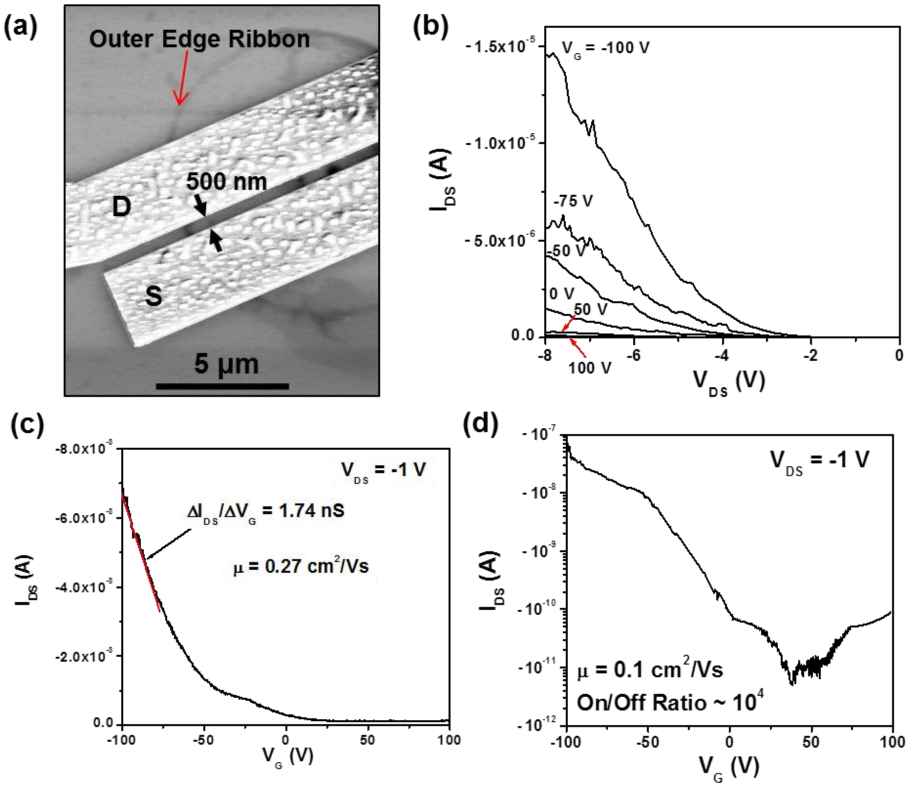

Figure 2.11 (a) SEM image of an exemplary back-gated FET made from the outer edge ribbon of a printed MoS_2 pixel with channel width of~300 nm, channel length of~500 nm, and gate dielectric (SiO_2) thickness of 330 nm. I_{DS}-V_{DS} (b) and I_{DS}-V_G (c) characteristics of this edge ribbon-based FET exhibit p-type conduction and field-effect mobility of ~0.27 cm^2/(V s). (d) I_{DS}-V_G characteristics of a p-type FET made from a MoS_2 flake blank-treated by SF_6 plasma.

ranging from 2 to 50 nm exhibit excellent and stable transport properties (*i.e.*, high ON/OFF ratios ranging from 10^4 to 10^7, high field-effect mobility values on the order of 10s cm^2/(V s) on SiO_2-based dielectrics and 100's cm^2/(V s) on high-k dielectrics, as well as subthreshold slopes of 60-70 mV/decade for top-gated FETs) [91-93]. To evaluate the potential scalability of our printing approaches especially for future scale-up transistor-based applications, we studied the uniformity of the transport characteristics of MoS_2

FETs produced by plasma-assisted printing as well as the dependence of FET characteristics on the change of the MoS_2 thickness. Figure 2.12 shows the transport characteristics of 14 FETs produced in a single printing cycle. Figure 2.13 displays (a) ON/OFF current ratio and (b) field-effect mobility data measured from these FETs, which are plotted as a function of the MoS_2 thickness. These FETs have different flake thicknesses ranging from 3 to 20 nm. It should be noted that although the thickness values of most as-printed MoS_2 flakes can be controlled to be less than 10 nm, as shown in Figures 2.2 (b) and 2.7 (c), relatively thicker flakes (*i.e.*, thickness ~10-20 nm) were intentionally chosen for making FETs in order to extend the investigation range of the flake thickness values and analyze the degree of redundancy in the control of the MoS_2 thickness. Figure 10 shows that in spite of the variation of the MoS_2 flake thickness in the range 3-20 nm, all the FETs exhibit high ON/OFF ratios in the range 10^5-10^7, reasonably high field-effect mobility values on SiO_2 gate dielectrics ranging from 15 to 24 $cm^2/(V\ s)$, and uniform threshold gate voltages around $V_{th} \approx -50$ V. Such results preliminarily demonstrate that the MoS_2 FETs produced by plasma-assisted printing do not show a sensitive dependence of FET characteristics on the change of the MoS_2 thickness in the range 3-20 nm. This also proposes that our printing approaches can generate a high yield of electronic-grade MoS_2 flakes with an acceptable degree of uniformity in FET characteristics and hold significant potential to be further developed into a manufacturing process for making arrays of working FETs. In addition, using HfO_2-based high-k gate dielectrics, the mobility values of our FETs are expected to be further improved by at least 1 order of magnitude [25], which is attributed to the dielectric screening effect [94].

The large arrays of such high-performance FETs produced by printing processes are expected to significantly facilitate the future scale-up electronic applications of few-layer

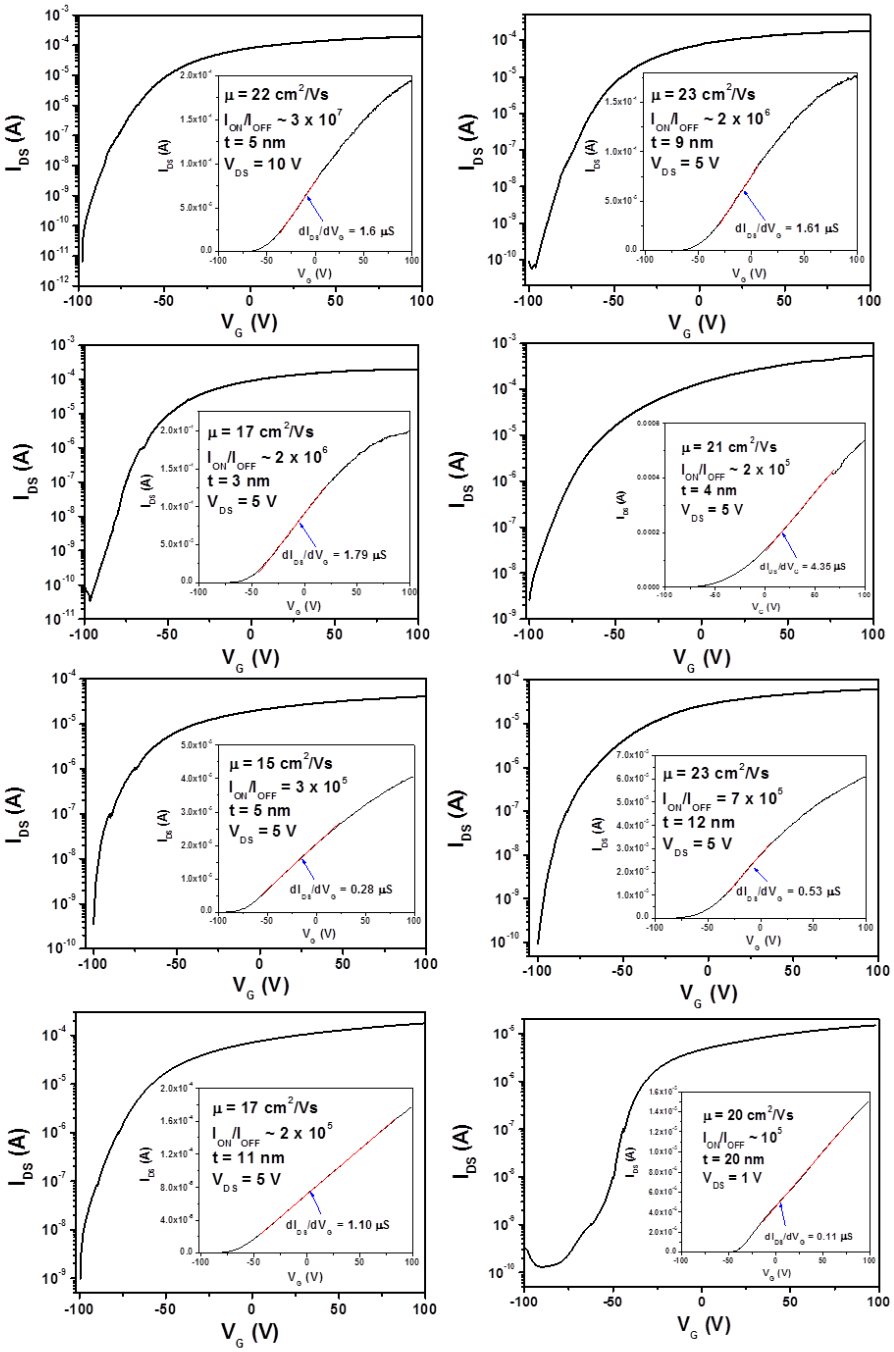

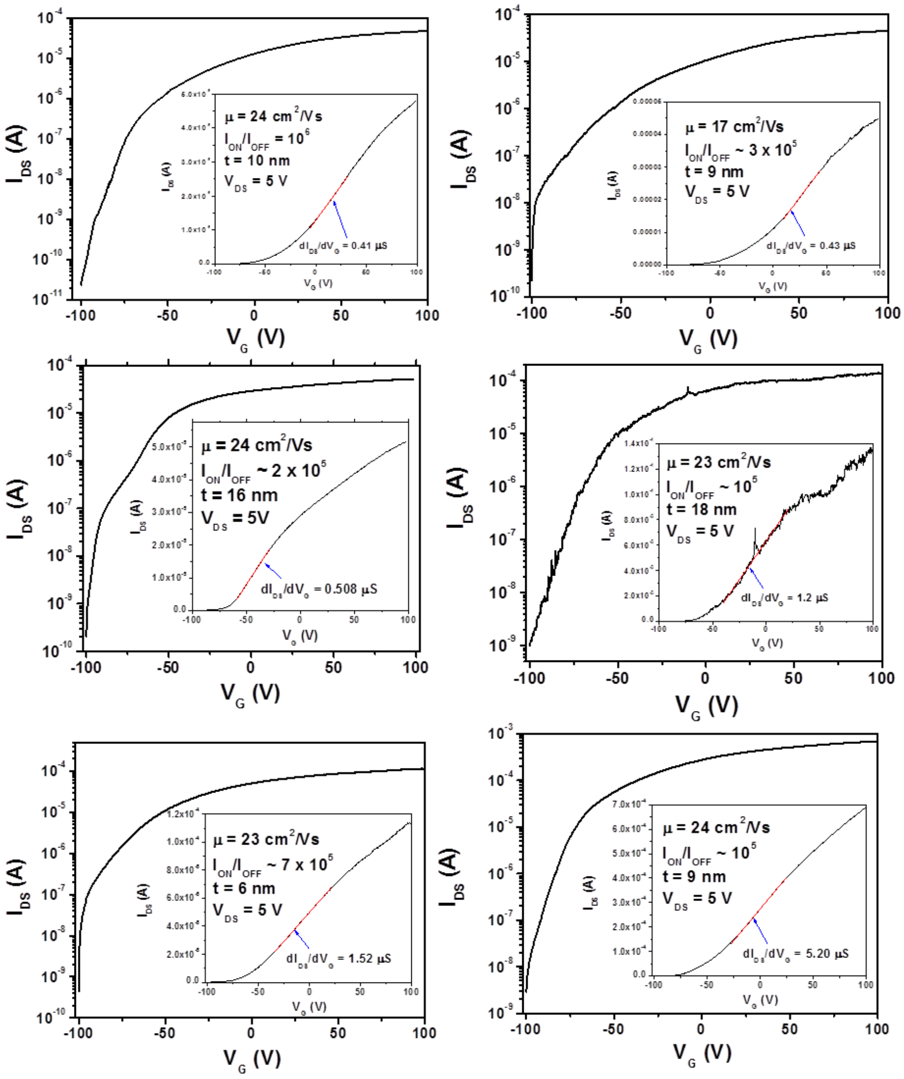

Figure 2.12 Semi-logarithmic I_{DS}-V_G characteristic curves of 14 back-gated FETs made from the inner flakes of MoS_2 pixels printed on a single substrate, which exhibit ON/OFF current ratios (I_{ON}/I_{OFF}) ranging from 10^5 to 10^7. The inset graphs display the linear plots of the I_{DS}-V_G curves, and the field-effect mobility (μ) can be extracted by fitting the linear regions of I_{DS}-V_G curves. μ ranges from 15 to 24 cm^2/Vs.

MoS_2. In our future research, we will integrate the top gates with sub-5 nm thick gate dielectrics into MoS_2 FETs in order to study the uniformity of other important FET parameters (*e.g.*, subthreshold slopes) and further explore the potential of our printing processes for manufacturing high-performance MoS_2-based electronic devices.

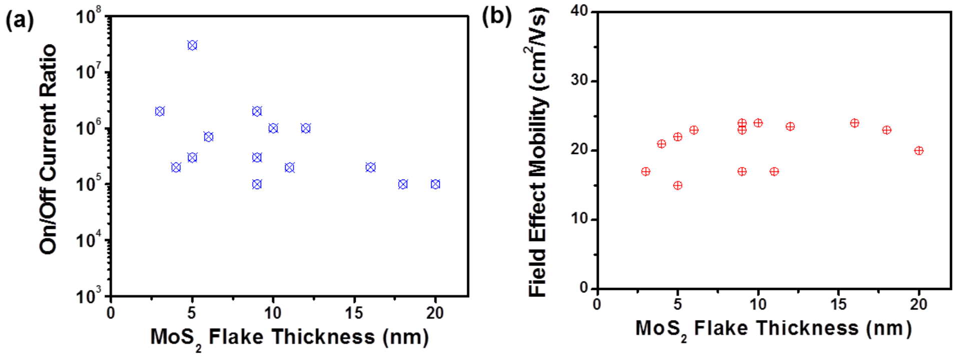

Figure 2.13 (a) ON/OFF current ratio and (b) field-effect mobility data extracted from the FET characteristics listed in Figure 2.12, which are plotted as a function of the MoS_2 flake thickness.

There are device applications requiring a more demanding control of the MoS_2 thickness. For example, optoelectronic applications usually require MoS_2 monolayers to obtain a large direct band gap [6]. For such applications, our printing approaches can potentially serve as a useful technique for transforming initial raw materials of few-layer MoS_2 into arrays of active device sites. These orderly formed MoS_2 flakes can be subsequently tailored through a series of postprinting processes to achieve a higher degree of uniformity in thickness and feature profile. For example, the laser-thinning technology with a self-termination mechanism recently developed by Castellanos-Gomez *et al.* could be used as a postprinting process for thinning as-printed MoS_2 flakes to increase the percentage yield of MoS_2 monolayers [72]. Furthermore, a postprinting lithography step (e.g., photolithography and nanoimprint) followed by plasma etching can be easily implemented to trim as-printed MoS_2 flakes into functional nanopatterns with specific shapes.

2.4 Summary

In conclusion, we demonstrate a novel approach for producing ordered arrays of few-layer-MoS_2 device features. In this process, the relief structures are prepatterned onto a bulk MoS_2 film, which serves as a stamp for printing out orderly arranged MoS_2 pixel patterns over cm^2-scale areas on both pristine and plasma-charged SiO_2 substrates. MoS_2 pixels printed on plasma-charged substrates feature a higher degree of uniformity in pattern profiles and a narrower distribution of the MoS_2 flake thickness (i.e., 3 ± 1.9 nm) in comparison with those printed on pristine substrates. This is attributed to the strong fringe field around the feature edges that is induced by plasma-introduced electric charges. We demonstrate that such printing approaches can be generalized for producing other emerging atomically layered nanostructures (e.g., graphene nanoribbons). The printed MoS_2 flakes can be used to build working n-type FETs with superior electronic properties (*i.e.*, $I_{ON}/I_{OFF} \approx 10^5$-$10^7$, mobility $\mu \approx$ 6-44 $cm^2/(V\ s)$). Using additional plasma treatment processes, as-printed MoS_2 flakes can be doped to create p-type FETs. Finally, we systematically study the thickness-dependent characteristics of MoS_2 FETs and show that our printing processes can produce a high yield of electronic-grade MoS_2 flakes with an acceptable degree of uniformity in transport properties.

Chapter 3

Multiple MoS_2 Transistors for Sensing Molecule Interaction Kinetics

3.1 Introduction

Using field-effect transistor (FET)-based biosensors produced from nanowires (NWs) and carbon nanotubes (CNTs), researchers have demonstrated detection of cancer biomarkers from nM to fM range in serum [95-101], in vitro detection of nM proteins in cell growth systems [102, 103], and quantification of the affinities/kinetics of the protein interactions with fM-level sensitivities [104]. The fM-level limit-of-detection (LOD) achieved by such nanoscale FET biosensors for monitoring biomarker concentrations would enable label-free, single-molecule-level detection of trace-level amount biomarkers. The arrays of such biosensors with consistent transistor responses would serve as reliable lab-on-a-chip platforms for precisely determining the kinetics of various biomolecule interactions. However, serious constraints imposed on nanofabrication severely prohibit the reliable manufacturing of the affordable biosensor chips utilizing such one dimensional (1D) nanostructures [95, 99, 100]. In particular, high-quality, small-size NWs and CNTs are required to make biosensors with fM-level LOD for concentration monitoring (or single-molecule-level LOD for trace-level amount detection) [105]. Especially, for trace-level amount detection, the critical dimensions of the sensing channels need to be comparable to the impact dimensions of charged molecules to maximize the gating effect due to the charged molecules and achieve very low LOD [98, 106, 107]. CNTs and many NWs are usually produced by using bottom-up synthesis methods (*e.g.*, chemical vapor deposition (CVD)). The community currently lacks proper top-down planar nanofabrication processes to produce ordered arrays of such nanostructures, which makes it very challenging to realize parallel high-throughput assay using biosensors made from these nanostructures. High-quality Si NW biosensor arrays can be made using top-down lithographic techniques [104]. However, the fabrication of such Si NW arrays usually requires expensive semiconductor-on-insulator (SOI) substrates and exquisite nanolithographic tools, which can result in a high processing cost and is not very suitable for manufacturing affordable (even disposable) assay chips for practical clinical biosensing applications. Emerging two-dimensional (2D) atomically layered materials, such as graphene, topological insulators (TIs), and TMDCs, recently attracted a great deal of interest because of their attractive electronic/ optoelectronic properties, large abundance, and compatibility to planar nanofabrication processes [25, 28, 53, 54, 58, 59, 61, 108-111]. Due to their atomically thin structures, the transport properties of 2D layers are highly sensitive to the external stimuli, which can enable new ultrasensitive 2D FETs suitable for biosensing applications [112-116]. Especially, in comparison with the thin film transistors made from conventional bulk semiconductors (e.g., Si and III-V compounds), the transistors based on MoS_2 and other atomically layered semiconductors are expected to show much more sensitive electrical responses to antigen-antibody binding events. Moreover, all 2D layers have an extremely low density of dangling bonds on their surfaces, which can result in high-quality FET channels with low densities of scattering centers (and hence low Flicker noise level), and enable highly sensitive, low-noise-level detecting of biomolecules [113, 117-120]. Novoselov *et al.* have demonstrated graphene-based FET sensors capable of detecting individual gas molecules absorbed on the graphene channels [10, 121]. In contrast to zero-bandgap graphene, semiconducting TMDCs (*e.g.*, MoS_2) have sizable bandgaps. Therefore, TMDC-based FETs show high On/Off current ratios up to 10^8, which, in combination with their atomically thin structures, can potentially enable the higher detection sensitivities for gas, chemical, and biological sensing applications in comparison with graphene FETs [43, 57, 122]. Wang *et al.* and Sarkar *et al.* recently demonstrated that FET biosensors made from microscale few-layer-MoS_2 flakes exhibit 100-400 fM LODs for detecting cancer-related biomarkers [42, 43]. These previous works strongly imply that such TMDC-based FET biosensors may not require sensing channels of nanoscale width to achieve fM-level LODs for concentration monitoring applications, and the fabrication of such biosensors would not need exquisite nanolithographic tools. Additionally, several recent nanomanufacturing-related works suggest that monolayer/few-layer TMDC structures and other relevant atomically layered materials hold significant potential to be produced over large areas on low-cost substrates (*e.g.*, glass, plastic, or rubber) by using cost-efficient processes such as CVD followed with roll-to-roll transfer [123], addressable deposition [124], and microscale stamping [80, 125, 126]. Therefore, it is very promising to realize cost-efficient manufacturing of multiplexing assays based on TMDC transistor arrays in the future. Toward such envisaged bio-assay capability, additional device-oriented research is required for quantitatively calibrating the sensor responses measured from multiple sets of TMDC FET biosensors, so that the calibrated response signals are consistent with each other and can synergistically enable precise quantification of biomarker concentrations (or amounts) as well as the affinities/kinetics of biomolecule interactions. Although individual MoS_2 FET biosensors have been fabricated and exhibited very high biodetection sensitivity [42, 43]. the utilization of multiple such devices for quantifying the biomolecule interactions has not been attempted.

In this chapter, we fabricated multiple sets of MoS_2-based transistor biosensors and demonstrated that these devices can be synergistically utilized to measure the concentrations of analyte solutions as well as the affinity and kinetic properties of the analyte-receptor pair. The biomolecule under study, TNF-α, is a pro-inflammatory cytokine and a key biomarker associated with host defense and immunosurveillance [127-130]. Researchers have shown that TNF-α secreted from immune cells stimulated with lipopolysaccharide (LPS) - an endotoxin causing septic shock due to severely pronounced immune response of the human body - reflects a functioning innate immune response [131, 132]. All our biosensors showed a TNF-α detection limit as low as 60 fM despite the small molecular size of the cytokine biomarker (~17 kDa) that renders its label-free detection at high sensitivity significantly challenging. Such a low detection limit was achieved in both linear and subthreshold regimes of the transfer characteristics of MoS_2 transistors. In both transport regimes, the electrically measured sensor responses were calibrated into signal quantities independent of the transistor performance. All sets of transistor biosensors showed consistent relationships between calibrated sensor responses and TNF-α concentrations. They created a standard curve, from which the equilibrium constant of the antibody-(TNF-α) pair was extracted to be K_D = 369 ± 48 fM. Based on this calibrated sensor model, the time-dependent association-dissociation kinetics of the antibody-(TNF-α) pair was further studied and the association/dissociation rates of the antibody-(TNF-α) pair were measured to be $(5.03 \pm 0.16) \times 10^{8}\ M^{-1}\ s^{-1}$ and $(1.97 \pm 0.08) \times 10^{-4}\ s^{-1}$, respectively.

3.2 Methods and Materials

3.2.1 Fabrication and Characterization of MoS_2 Transistor Biosensors

The MoS_2 transistors were fabricated using a microprinting method previously reported [126]. Few-layer-MoS_2 channel thicknesses were specifically controlled to be 15-20 nm. Such a MoS_2 thickness range has been demonstrated to result in the optimal field-effect mobility values for MoS_2 transistors [93, 133]. The transistor channel lengths (*L*) were ~5 μm and the channel widths (*W*) ranged from 5 to 8 μ m. Ti (5 nm)/Au (50 nm) electrode pairs served as drain (*D*) and source (*S*) contacts, which were produced using photolithography followed with metal deposition and lift-off. The p^{+}-Si substrates were used as the back gates (*G*). Thermally grown SiO_2 layers (300 nm thick) were used as the back-gate dielectrics. Such 300 nm thick SiO_2 layers can enable a simple color coding method for us to quickly identify MoS_2 flakes with appropriate thicknesses (*i.e.,* 15-20 nm) [134]. All electrical measurements were performed using an HP-4145B semiconductor parameter analyzer.

3.2.2 Bio-Functionalization of MoS_2 Transistor Biosensors

First, an as-fabricated transistor biosensor is immersed in 5% (3-Aminopropyl) triethoxysilane (APTES, purchased from Sigma-Aldrich Co. LLC.) in ethanol for 1 hour. After the incubation, the sensor is rinsed with phosphate buffered saline (PBS) and blown dry by nitrogen gas. After this step, the HfO_2 effective layer is silanized with an APTES monolayer. The device is subsequently immersed in 5% gluteraldehyde (GA) (purchased from Sigma-Aldrich Co. LLC.) in PBS for 2 hours followed by rinsing with PBS. Afterwards, anti-human TNF-α antibody (from eBioscience, Inc.) of 50 μg/ml concentration in DI water is dropped on the sensor and incubated for 1 hour. For studying the equilibrium-state sensor responses, the as-functionalized sensor is incubated with TNF-α solutions with incremental concentrations (i.e., n = 60 fM, 300 fM, 600 fM, 3 pM, and 6 pM; the incubation time for each of the concentrations: ~2 hours). The incubation is performed using the setup illustrated in Figure 3.1 (d). After each incubation process, the transfer characteristics of the transistor sensor are measured.

3.2.3 Quantification of the Time-Dependent Association/Dissociation Kinetics of the Antibody-(TNF-α) Pair

An as-functionalized MoS_2 transistor biosensor is covered with a polydimethylsiloxane (PDMS) block bearing a microfluidic channel (10 mm in length, 200 μm in width, 50 μm in height), as illustrated in Figure 3.1 (e). A motorized syringe pump is used for driving the analyte flows into and out of the microfluidic channel through an inlet/outlet tubing kit (tube diameter: 0.75 mm). At the beginning of the measurement of a real-time sensor response curve associated with antibody-(TNF-α) binding, deionized (DI) water is injected into the sensor with flow rate of 5 μL/min. At the same time, the MoS_2 transistor is biased under a given set of V_G and V_{DS}. After the I_{DS} value is stabilized, the analyte solution with a specific TNF-α concentration is inserted into the sensor.

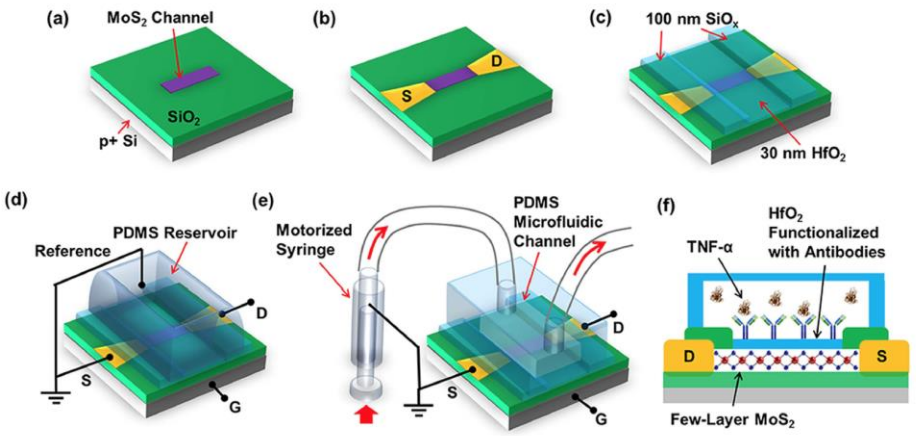

Figure 3.1 Flow chart for fabricating a MoS_2 transistor biosensor: (a) printing of a few-layer MoS_2 flake onto a p^+-Si/SiO_2 substrate; (b) fabrication of Ti/Au *D/S* contacts; (c) ALD growth of the HfO_2 effective layer on top of the MoS_2 channel and coating of *D/S* contacts with thick SiO_x layers; (d) integration of a PDMS liquid reservoir on top of the MoS_2 transistor for measuring sensor responses from different TNF-α concentrations under thermodynamic equilibrium condition and determining the affinity of the antibody-(TNF-α) pair; (e) integration of a microfluidic inlet/outlet tubing kit driven by a motorized syringe pump on top of the transistor for quantifying the association-dissociation kinetics of the antibody-(TNF-α) pair; (f) functionalization of the HfO_2 effective layer with antibody receptors and subsequent TNF-α detection.

3.3 Results and Discussion

3.3.1 Static Measurement Results of Few-Layer MoS_2 Transistor Biosensors

Figure 3.1 displays the steps for fabricating a transistor biosensor with a few-layer MoS_2 sensing channel. First, a pristine few-layer MoS_2 flake is printed onto a p^+-doped Si substrate coated with 300 nm thick SiO_2 (Figure 3.1 (a)). This printing process is the same as the method previously reported by us [126]. The thickness of the MoS_2 flake chosen for making a biosensor is specifically controlled to be 15-20 nm, aiming to achieve relatively high field-effect mobility values (μ = 20 to 30 $cm^2/V\ s$) [93, 133]. After the MoS_2 printing, metallic drain/source (*D/S*) contacts (5 nm Ti/50 nm Au) are fabricated using photolithography followed with metal deposition and lift-off, and a back-gated MoS_2 transistor is subsequently formed (Figure 3.1 (b)). To enable a capacitive coupling between the microfluidic reservoir (or channel) and the MoS_2 transistor channel, a 30 nm thick HfO_2 layer is deposited on top of the MoS_2 channel using atomic layer deposition (ALD) (Figure 3.1 (c)). This HfO_2 layer also serves as an effective layer for biofunctionalization. Afterwards, additional 100 nm thick SiO_x is sputtered on D/S contacts to minimize the leakage current between D/S contacts and microfluidic components (Figure 3.1 (c)). Before the TNF-α detection, anti-human TNF-α antibody is functionalized on the HfO_2 effective layer. The detailed antibody functionalization procedure is illustrated in Figure 3.2. To measure the MoS_2 transistor sensor responses from different TNF-α concentrations under the thermodynamic equilibrium condition and determine the affinity of the antibody-(TNF-α) pair, a large open liquid reservoir made from polydimethylsiloxane (PDMS) is integrated on top of the MoS_2 transistor (Figure

3.1 (d)). Such a setup is very simple and enables the quick loading of various analyte solutions. To measure the association-dissociation kinetics of the antibody-(TNF-α) pair, a microfluidic channel is integrated on top of the transistor sensor, and a motorized syringe pump is used for driving the TNF-α solution flow into and out of the microfluidic channel through an inlet/outlet tubing kit (Figure 3.1 (e)). Such a setup can enable stable laminar flows of analyte solutions and minimize the noise induced by the liquid loading processes, which is needed to precisely analyze the real-time kinetic processes of antibody-(TNF-α) binding. Figures 3.1 (d) and (e) also illustrate the circuit setups for measuring the transistor sensor responses. In addition, Figure 3.1 (f) illustrates the cross-sectional view of a MoS_2 transistor sensor in the TNF-α detection operation.

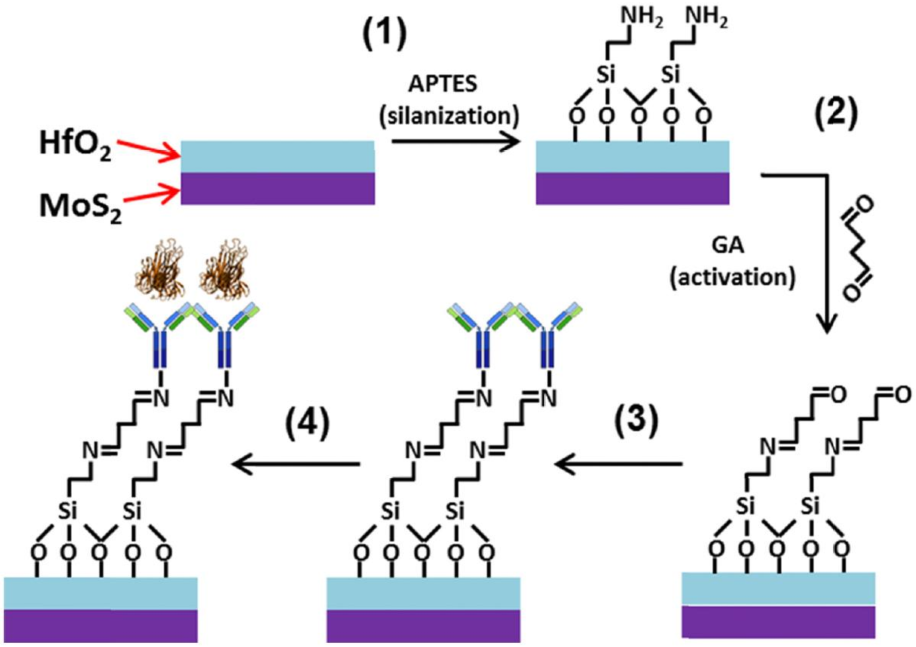

Figure 3.2 Protocol for functionalizing a MoS_2 transistor sensor with anti-human TNF-α antibody receptors for detecting TNF-α molecules

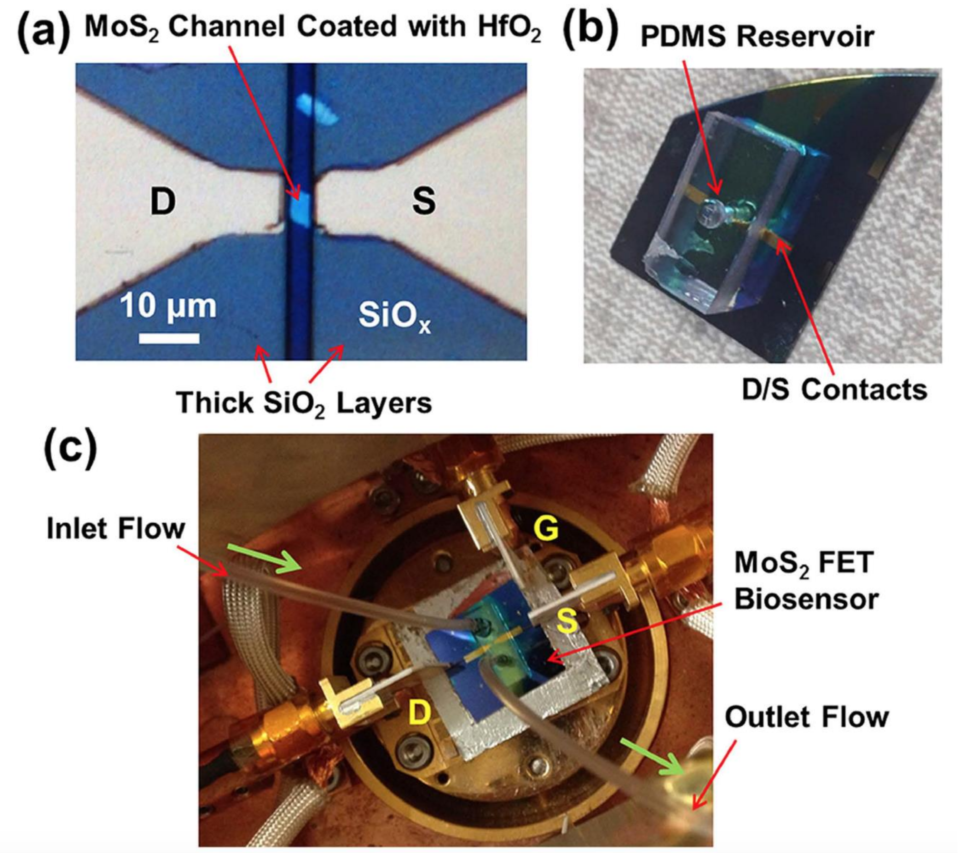

Figure 3.3 Optical micrographs or photographs of (a) an exemplary MoS$_2$ transistor with channel length (L) and width (W) of 5 and 6 μm, respectively; (b) an as-fabricated MoS$_2$ transistor biosensor integrated with a cylindrical liquid reservoir, which is drilled into a PDMS block and is ~4 mm deep and ~1 mm in diameter; (c) a transistor biosensor integrated with a microfluidic channel system connected with an inlet/outlet tubing kit, which is driven by a motorized syringe pump.

Figure 3.3 (a) displays the optical micrograph (OM) of an exemplary MoS$_2$ transistor with channel length (L) and width (W) of 5 and 6 μm, respectively. Figure 3.3 (b) shows the photograph of an as-fabricated MoS$_2$ transistor biosensor integrated with a PDMS liquid reservoir. The reservoir is ~4 mm deep and is ~1 mm in diameter, which is drilled into a PDMS block with length, width, thickness of 2, 1, and 0.4 cm, respectively. Figure 3.3 (c) displays the photograph of a biosensor integrated with a microfluidic channel connected with an inlet/outlet tubing kit.

First we measured the sensor responses from different TNF-α concentrations under the thermodynamic equilibrium condition. The biosensor setup shown in Figure 3.3 (b) was used for this measurement. For each transistor biosensor, the static transfer characteristics (*i.e.*, drain-source current (I_{DS}) – back gate voltage (V_G) curves acquired under a fixed drain-source voltage (V_{DS})) were measured at each of the biodetection stages, following the sequence of (1) bare transistor, (2) antibody functionalization, and inputs of TNF-α solutions with concentrations of (3) 60 fM, (4) 300 fM, (5) 600 fM, (6) 3 pM, and (7) 6 pM. To remove the effect of the I_{DS}-V_G hysteresis, all I_{DS}-V_G curves were measured by sweeping V_G from -100 V to 100 V with a sweep rate of 10 V/s.

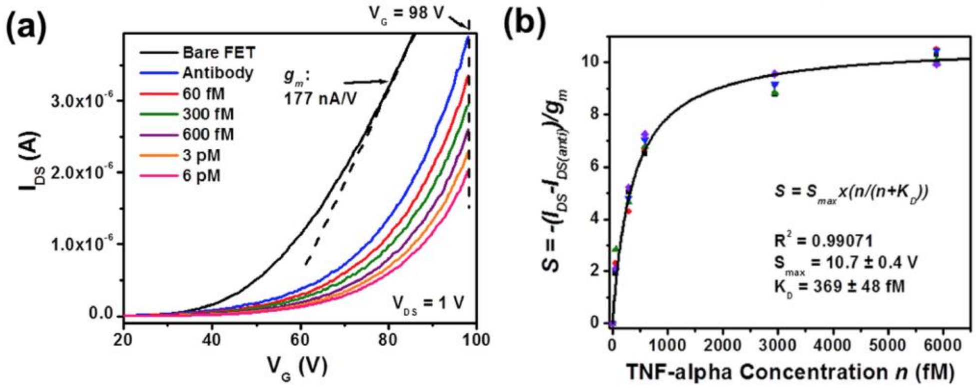

Figure 3.4 Sensor responses measured in the linear transport regimes of MoS_2 transistor biosensors: (a) transfer characteristics of an exemplary MoS_2 transistor sensor measured at various biodetection stages, following the sequence of (1) bare transistor, (2) antibody functionalization, and inputs of TNF-α solutions with concentrations of (3) 60 fM, (4) 300 fM, (5) 600 fM, (6) 3 pM, and (7) 6 pM; (b) a set of calibrated linear-regime responses (*S*) measured from five different MoS_2 transistor sensors with respect to TNF-α concentration (*n*). These *S*-*n* relationships can be well fitted with Langmuir isotherms and the dissociation constant (K_D) of the antibody-(TNF-α) pair is extracted to be 369 ± 48 fM.

Figure 3.4 shows the sensor responses measured in the linear transport regimes of MoS_2 transistor sensors. Specifically, Figure 3.4 (a) shows the transfer characteristics of an exemplary sensor measured at various biodetection stages. Here, I_{DS} data are plotted in the linear scale. The transfer characteristics of this sensor show a strong dependence on TNF-α concentrations, and the TNF-α detection limit is estimated to be ~60 fM. We choose a fixed V_G within the linear regimes of all I_{DS}-V_G curves (*e.g.*, V_G = 98 V, as denoted by the dashed vertical line in Figure 3.4 (a)). The I_{DS} values measured under this V_G vary according to different biodetection states and such I_{DS} data could be used as a sensor response signal. However, such a response signal is highly dependent on the transistor performance parameters (*e.g.*, transconductance (g_m) and threshold voltage (V_T)). Therefore, in the analysis of a given biodetection state, the I_{DS} signals obtained by different MoS_2 transistors may exhibit a poor device-to-device consistency due to the nonuniformity of MoS_2 transistors. Although such an issue could be alleviated through optimizing the material deposition and device fabrication processes, a calibrated sensor response quantity independent of the device performance is highly desirable.

$$I_{DS} = g_m\left(V_G - V_T - \frac{V_{DS}}{2}\right) \qquad (1)$$

$$S = -\frac{I_{DS} - I_{DS(anti)}}{g_m} = \Delta V_T = \frac{q d_{SiO2}\sigma_{TNF}}{K_{SiO2}\varepsilon_0} \qquad (2)$$

The linear regime of an I_{DS}-V_G characteristic curve measured from a microscale MoS_2 transistor sensor in a specific biodetection state can be expressed as Equation (1). In our experiments, it is observed that for a given transistor sensor, the g_m values extracted from different I_{DS}-V_G curves that correspond to different biodetection states are very close and can be approximated as a constant for this sensor. For example, the g_m value of the sensor shown in Figure 3.4 (a) is extracted to be ~177 nS at V_{DS} = 1 V. Based on this observation and Equation (1) as well as the implication from previous works done by Duan *et al.* and Ishikaw *et al.* [104, 135], a calibrated sensor response quantity (S) is derived and expressed in Equation (2), where $I_{DS(anti)}$ is the I_{DS} value measured in the "antibody functionalization" state of a sensor biased under a set of fixed V_{DS} and V_G, and I_{DS}-$I_{DS(anti)}$ indicates the I_{DS} variation induced by the introduction of TNF-α molecules. Such an I_{DS} variation normalized by the g_m of this sensor results in a sensor response quantity directly associated with the change in the V_T of the sensor (*i.e.*, ΔV_T). It should be noted that although ΔV_T is assumed to be completely induced by the charge brought to the HfO_2 effective layer on top of the transistor channel through antibody-(TNF-α) binding events, ΔV_T is not exactly the binding-event-induced potential change ($\Delta \Phi$) on the effective layer. This is because in this work, ΔV_T is the change in the V_T measured from the back gate. However, ΔV_T and $\Delta \Phi$ can be related by $\Delta V_T = (C_{HfO2}/C_{SiO2})\Delta \Phi$, where C_{SiO2} and C_{HfO2} are the capacitances of the SiO_2 back gate dielectric and the HfO_2 effective layer, respectively. More detailed discussion about these potential parameters can be found from the dual-gate transistor model illustrated in Appendix B. Based on this model, ΔV_T can be evaluated using $\Delta V_T = qd_{SiO2}\sigma_{TNF}/k_{SiO2}\varepsilon_0$, where q is the effective charge carried by a TNF-α molecule (the screening effect due to the buffer liquid has been incorporated into q); d_{SiO2} and k_{SiO2} are the thickness and dielectric constant of the SiO_2 back-gate dielectric layer, respectively; ε_0 is the vacuum permittivity; and σ_{TNF} is the areal density of TNF-α molecules bound to the antibody receptors functionalized on the effective layer. Therefore, such a calibrated response quantity (S) is proportional to the antibody receptor occupancy at the equilibrium state and it is also independent of the MoS_2 transistor performance. These two conditions are important for the subsequent Langmuir isotherm analysis.

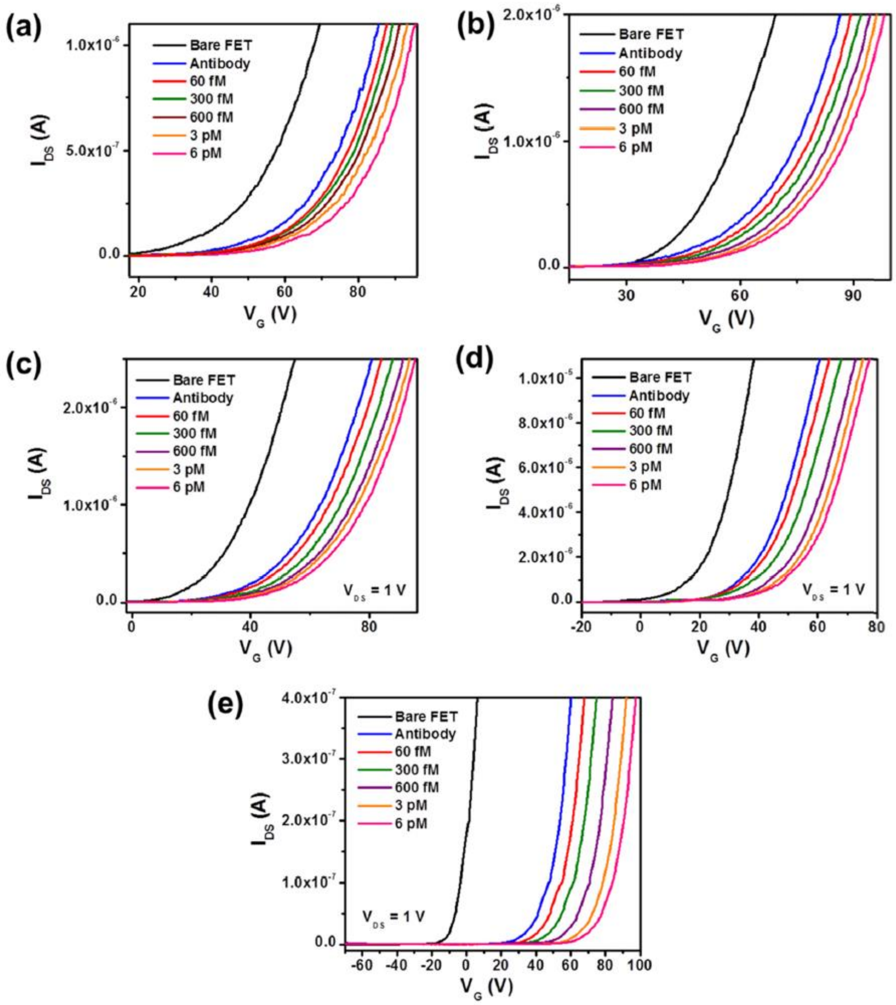

Figure 3.5 Linear-regime sensor responses at the equilibrium state: The transfer characteristics of five different MoS_2 transistor sensors measured at various biodetection stages, following the sequence of (1) bare transistor, (2) antibody functionalization, and inputs of TNF-α solutions with concentrations of (3) 60 fM, (4) 300 fM, (5) 600 fM, (6) 3 pM, and (7) 6 pM.

Figure 3.4 (b) plots the calibrated responses measured from the linear transport regimes of five different sensors with respect to TNF-α concentration (n). The detailed transfer characteristics of these five devices measured at various biodetection stages are showed in Figure 3.5. Although Figure 3.5 shows that the transfer characteristics of these five sensors exhibit significant difference in V_T, I_{DS} and g_m, Figure 3.4 (b) shows that the calibrated responses from these sensors are consistent with each other and can serve as a standard curve (*i.e.*, a generic S-n curve) for TNF-α detection. This standard curve can be well fitted with Langmuir isotherms (Equation (3)) and the affinity equilibrium (or dissociation) constant (K_D) of the antibody-(TNF-α) pair is extracted to be 369 ± 48 fM; the maximum sensor response (S_{max}) is extracted to be 10.7 ± 0.4 V.

$$S = S_{max} \frac{n}{n + K_D} \qquad (3)$$

Alternatively, sensor responses can also be measured from the subthreshold regimes of MoS_2 transistor sensors. In the subthreshold regime of a transistor sensor, the sensitivity of I_{DS} to the variation of electrical potential (or charge) at the effective layer is much higher than that in the linear transport regime of this sensor. Therefore, the responses from the subthreshold regimes of transistor sensors are expected to result in the higher biodetection sensitivity in comparison with those from the linear regimes. Figure 3.6 (a) displays the transfer characteristics of another exemplary MoS_2 transistor sensor, which were measured at various biodetection stages. Here I_{DS} data are plotted in the logarithm scale, and the subthreshold regimes are emphasized. We choose a fixed V_G within the subthreshold regimes of all I_{DS}-V_G curves (*e.g.*, V_G = 29 V denoted by the vertical dashed line in Figure 3.6 (a)). The I_{DS} values measured under this V_G clearly vary according to different biodetection states and exhibit a strong dependence on TNF-α concentration. Here, the TNF-α detection limit is estimated to be at least as low as 60 fM. Similarly, such I_{DS} data acquired in the subthreshold regimes of transistor sensors cannot be directly used as standard sensor responses. A calibrated subthreshold-regime response quantity independent of the transistor performance is required.

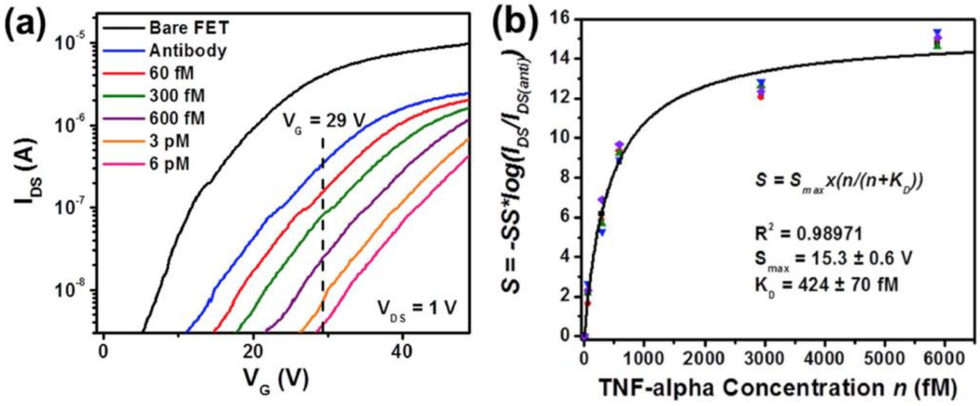

Figure 3.6 Sensor responses measured in the subthreshold regimes of MoS_2 transistor biosensors: (a) transfer characteristics of an exemplary MoS_2 transistor sensor measured at various biodetection stages, following the sequence of (1) bare transistor, (2) antibody functionalization, and inputs of TNF-α solutions with concentrations of (3) 60 fM, (4) 300 fM, (5) 600 fM, (6) 3 pM, and (7) 6 pM (Here I_{DS} data are plotted in the logarithm scale, and the subthreshold regimes are emphasized); (b) a set of calibrated subthreshold-regime responses (S) measured from five different MoS_2 transistor sensors with respect to TNF-α concentration (n). These S-n relationships can be well fitted with Langmuir isotherms and the dissociation constant (K_D) of the antibody-(TNF-α) pair is extracted to be 424 ± 70 fM.

In the subthreshold regime of a microscale MoS_2 transistor sensor, the I_{DS}-V_G relationship measured from a specific biodetection state can be approximately expressed by Equation (4), where I_T is the I_{DS} value measured at $V_G=V_T$ under a given V_{DS}; SS is the subthreshold swing. As observed in our experiments, although the functionalization of a transistor sensor with antibody receptors (*i.e.*, the transition from “bare transistor” to “antibody functionalization” states) can result in an observable reduction of the *SS* of this sensor, the *SS* value does not significantly vary among the subsequent biodetection states, including the inputs of TNF-α samples with incremental concentrations. Therefore, for a given as-functionalized transistor sensor, *SS* can be approximated as a constant. Based on this observation, a calibrated subthreshold-regime sensor response quantity (*S*) is derived from Equation (4) and expressed in Equation (5), in which $I_{DS(anti)}$ is the drain-source current measured in the “antibody functionalization” state of a sensor biased under a set of fixed V_{DS} and V_G; and I_{DS} is the drain-source current measured from a subsequent biodetection state (*i.e.*, a specific TNF-α concentration). Similar to the calibrated linear-regime response quantity expressed in Equation (2), this subthreshold counterpart is also directly related to ΔV_T, independent of the transistor performance, and proportional to σ_{TNF}.

$$I_{DS} = I_T \times 10^{(V_G - V_T)/SS} \qquad (4)$$

$$S = -SS \times \log\left(\frac{I_{DS}}{I_{DS(anti)}}\right) = \Delta V_T = \frac{q d_{SiO2} \sigma_{TNF}}{k_{SiO2} \varepsilon_0} \qquad (5)$$

Figure 3.6 (b) shows the calibrated subthreshold-regime responses (*S*) measured from five different sensors with respect to TNF-α concentration (*n*). The detailed transfer characteristics of these five devices measured at various biodetection stages are showed in Figure 3.7. As shown in Figure 3.7, the transfer characteristics of these five sensors show significant difference in V_T, I_{DS} and *SS* parameters. However, as shown in Figure

3.6 (b), the calibrated *S*-*n* curves measured from these devices are consistent with each other and can be well fitted with Langmuir isotherms (Equation (3)). Here, the equilibrium constant (K_D) of the antibody-(TNF-α) pair is extracted to be 424 ± 70 fM, which is consistent with the K_D value extracted from the linear-regime sensor responses (*i.e.*, 369 ± 48 fM). The S_{max} parameter is fitted to be 15.3 ± 0.6 V, which is about 40% larger than that extracted from the linear-regime responses (*i.e.*, 10.7 ± 0.4 V). This observable discrepancy has not been fully understood. However, this could be temporarily attributed to the different back-gate V_G levels required for biasing sensors in subthreshold and linear regimes, which could result in different magnitudes of electric field penetrating through few-layer MoS_2 channels as well as HfO_2 effective layers and leaking into the analyte solution. This could lead to different degrees of the modification of electrical-double-layers around sensors and therefore different degrees of the screening of the charges brought through analyte-receptor binding pairs.

Although the I_{DS} signals measured from both linear and subthreshold regimes can be mathematically normalized to consistent device-independent response quantities using Equations (2) and (5), the physical limit-of-detection of a transistor biosensor is indeed determined by the sensitivity of I_{DS} to the variation of analyte concentration (dn) as well as the noise level of electrically measured I_{DS} signals. This I_{DS} sensitivity is quantitatively defined as the relative change in I_{DS} per change in *n* (*i.e.*, Sensitivity $= \frac{dI_{DS}}{I_{DS}}/dn$). Figure 3.8 displays and compares the sensitivity data acquired from (a) the linear-regime I_{DS} signals measured from the five sensors shown in Figure 3.5 and (b) the subthreshold-regime I_{DS} signals from the five sensors shown in Figure 3.7. All differential sensitivity values are evaluated at TNF-α concentration of n = 60 fM. This can offer critical information about the sensitivity required for obtaining fM-level detection limits. Figure 3.8 shows that the subthreshold-regime I_{DS} sensitivities (0.52 ± 0.3%/fM) are statistically

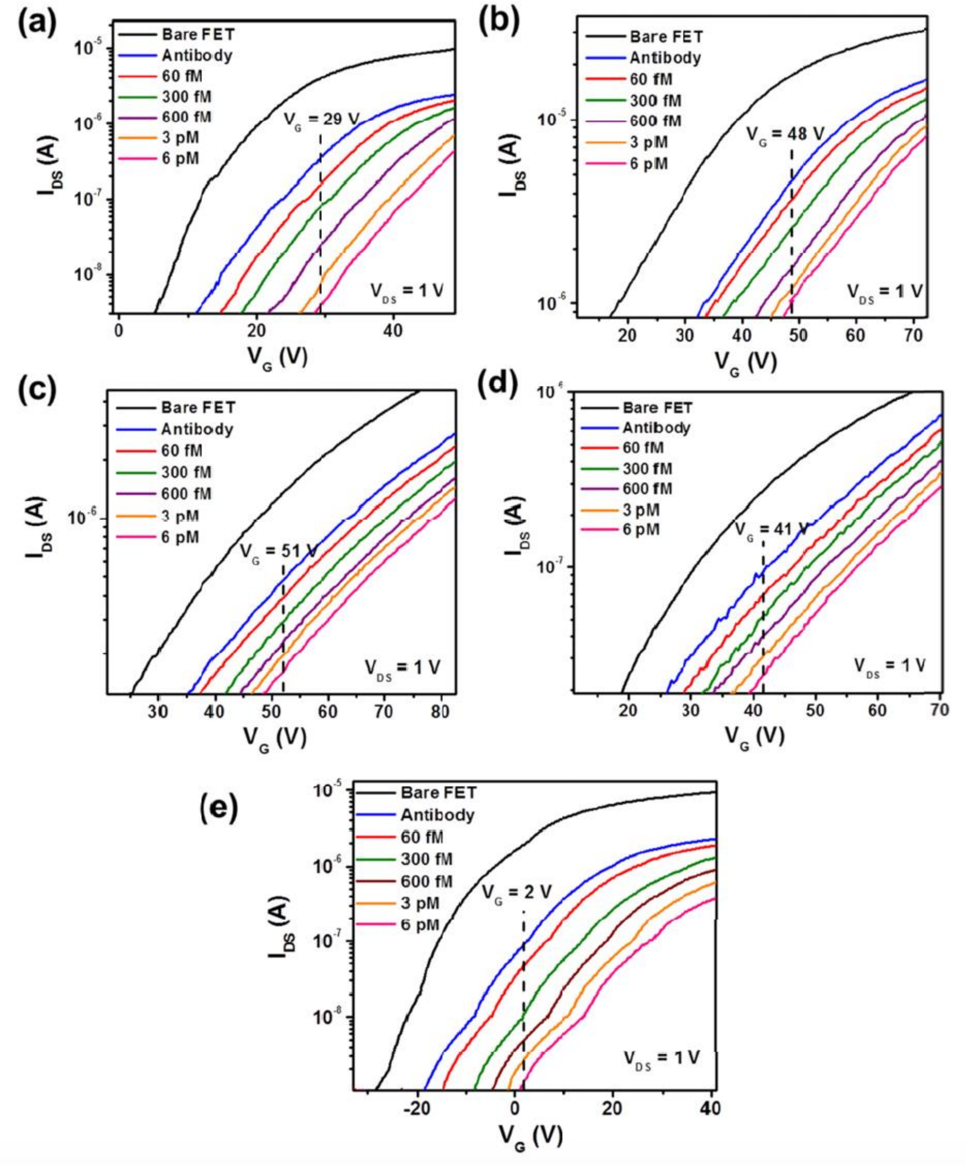

Figure 3.7 Subthreshold-regime sensor responses at the equilibrium state: The transfer characteristics of five different MoS_2 transistor sensors measured at various biodetection stages, following the sequence of (1) bare transistor, (2) antibody functionalization, and inputs of TNF-α solutions with concentrations of (3) 60 fM, (4) 300 fM, (5) 600 fM, (6) 3 pM, and (7) 6 pM.

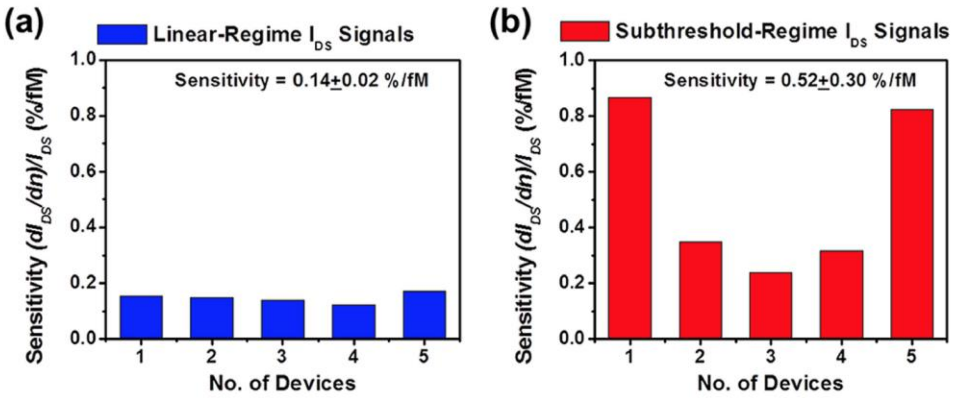

Figure 3.8 Sensitivity data acquired from (a) the linear-regime I_{DS} signals measured from the five sensors shown in Figure 3.5 and (b) the subthreshold-regime I_{DS} signals measured from the five sensors shown in Figure 3.7. All differential sensitivities were evaluated at TNF-α concentration of n = 60 fM

higher than the linear-regime I_{DS} sensitivities (0.14 ± 0.02%/fM). Therefore, subthreshold-regime sensor responses are more desirable in achieving high detection sensitivity. However, it should be noted that the ultimate detection limit of a transistor sensor is also limited by the signal-to-noise ratios of electrically measured I_{DS} signals. In addition, for detecting low-abundance molecules, the non-specific adsorption of target molecules could also strongly affect the detection limit. The further analysis of these aspects is beyond the scope of this work but will be addressed in the future research. Finally, it is also noted that the sensitivity data listed in Figure 3.8 (b) show the larger device-to-device variation in comparison with those listed in Figure 3.8 (a). This is probably because of that the subthreshold swing properties of MoS_2 transistors are more sensitive to the fabrication-introduced defects than their linear-regime transconductance properties. Therefore, for our current MoS_2 transistors, their linear-regime I_{DS} signals (or linear-regime transconductances) exhibit the higher device-to-device consistency than their subthreshold-regime I_{DS} signals.

To evaluate the detection specificity of our MoS_2 transistor sensors, a sensor functionalized with anti-human TNF-α antibody is used for detecting interleukin-6 (IL-6) cytokine. Figure 3.9 shows the transfer characteristics of this sensor measured at various stages, including (1) bare transistor, (2) antibody functionalization, and inputs of IL-6 solutions with concentrations of (3) 600 fM and (4) 6 pM. Figure 3.9 displays that the presence of IL-6 that is not specific to TNF-α antibody cannot result in prominent change in the transfer characteristics. Such experimentally observed weak sensor responses to IL-6 indicate a negligible nonspecific adsorption of IL-6 molecules on the sensor surface, which may be effectively screened by the densely-packed self-assembled monolayers of (3-Aminopropyl) triethoxysilane (APTES) on HfO_2 effective layers.

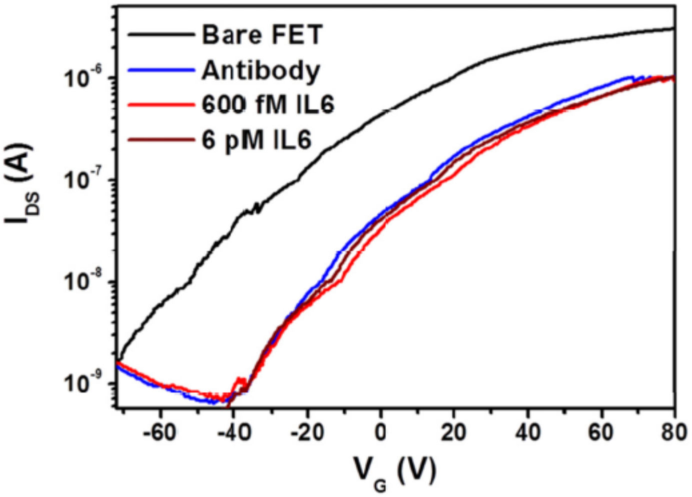

Figure 3.9 A negative control test of the detection specificity of MoS_2 transistor biosensors: The transfer characteristics of a control sensor measured at stages of (1) bare transistor, (2) antibody functionalization (still functionalized with anti-human TNF-α antibody receptors), and inputs of IL-6 solutions with concentrations of (3) 600 fM and (4) 6 pM.

3.3.2 Time-Dependent Measurement Results of Few-Layer MoS_2 Transistor Biosensors

The biosensor setup shown in Figure 3.3 (c) is used for measuring the time-dependent association/dissociation kinetics of the antibody-(TNF-α) pair. Figure 3.10 (a) shows real-time sensor responses of antibody-(TNF-α) binding measured under different TNF-α concentrations (*i.e.*, n = 60 fM, 600 fM, 3 pM, and 6 pM). Each of the time-dependent response curves was measured from a different MoS_2 transistor sensor and all as-measured I_{DS} responses were normalized using $S = -SS \times log(I_{DS}/I_{DS(anti)})$ (*i.e.*, Equation (5) for calibrating subthreshold-regime responses). Figure 3.11 presents the detailed transfer characteristics of these transistor sensors measured before the input of TNF-α samples, from which the SS parameters required for normalizing I_{DS} responses were acquired. In addition, the operation points (*i.e.*, the fixed V_G and V_{DS} values, under which a real-time response curve was measured) are also labeled in Figure 3.11. In Figure 3.10 (a), the red arrow indicates the onset time, at which the solutions with specific TNF-α concentrations were filled into the respective biosensors. The real-time response curves in Figure 3.10 (a) exhibit that the association rate of the antibody-(TNF-α) pair increases with increasing TNF-α concentration. The rise segment of each real-time response curve can be well fitted with the first-order absorption equation (*i.e.*, Equation (6)) [104]. In Equation (6), S_{eq} is the sensor response at the final equilibrium state; k_{on} and k_{off} are association and dissociation rates, respectively; $k_{on}n + k_{off}$ relates to the rising slope of the linear regime of the response curve. Table 1 lists the fitting results of S_{eq} and ($k_{on}n + k_{off}$) parameters for n = 60 fM, 600 fM, 3 pM, and 6 pM. These S_{eq} values extracted from the real-time binding responses are consistent with the sensor responses directly measured at the equilibrium state, that is, after a long incubation time of ~2 hours (*e.g.*, the equilibrium-state response data shown in Figure 3.6 (b)). In particular, Figure 3.10 (b) plots the extracted S_{eq} data as a function of TNF-α concentration, which can be also fitted

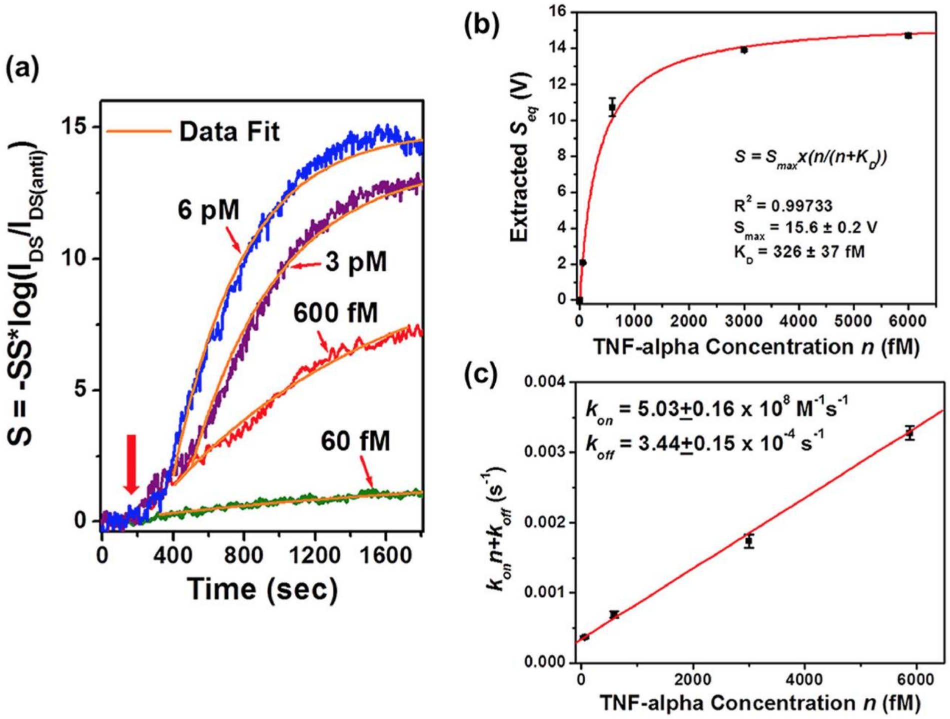

Figure 3.10 Time-dependent association kinetics of the antibody-(TNF-α) pair: (a) real-time sensor responses of antibody-(TNF-α) binding measured under different TNF-α concentrations (*n* = 60 fM, 600 fM, 3 pM, and 6 pM). Each of the response curves was measured from a different MoS_2 transistor sensor and all responses were normalized using Equation (5). The rise parts of the binding response curves can be fitted with Equation (6). (b) The equilibrium-state responses (S_{eq}) extracted from this fit plotted as a function of TNF-α concentration, which can be further fitted with Langmuir isotherm. The equilibrium constant (K_D) is extracted to be 326 ± 37 fM. (c) The extracted ($k_{on}n + k_{off}$) data plotted as a function of TNF-α concentration (n). The linear fitting of this ($k_{on}n + k_{off}$)-versus-n graph results in rate constants of $k_{on} = (5.03 \pm 0.16) \times 10^8$ M^{-1} s^{-1} and $k_{off} = (3.44 \pm 0.15) \times 10^{-4}$ s^{-1}.

with Langmuir isotherm. Here, the equilibrium constant (K_D) is extracted to be 326 ± 37 fM and the maximum response (S_{max}) is extracted to be 15.6 ± 0.2 V, which are consistent with those extracted from the equilibrium-state subthreshold-regime responses shown in Figure 3.6 (b).

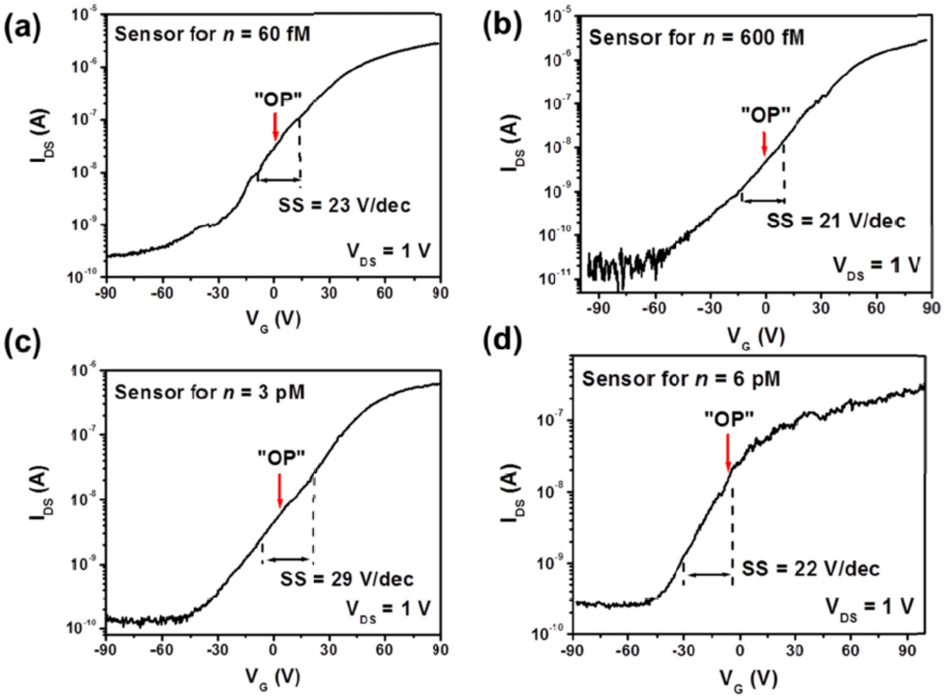

Figure 3.11 Transfer characteristics of four different MoS_2 transistor biosensors measured before the input of TNF-α samples, from which the subthreshold-swing (*SS*) parameters were acquired for normalizing the real-time subthreshold-regime sensor responses (Equation (5)). These sensors were utilized to quantify the real-time kinetics of antibody-(TNF-α) binding under different TNF-α concentrations (*n*) of (a) 60 fM, (b) 600 fM, (c) 3 pM, and (d) 6 pM. The operation points (OP, *i.e.*, the fixed V_G and V_{DS} values, under which a real-time response curve was measured) are also labeled by the red arrows.

$$S = S_{eq}\left(1 - e^{-(k_{on}n+k_{off})t}\right) \qquad (6)$$

	n=60 *fM*	**600 *fM***	**3 *pM***	**6 *pM***
S_{eq} (V)	2.07 ± 0.03	10.7 ± 0.5	13.9 ± 0.06	14.7 ± 0.13
$(k_{on}n \pm k_{off})$ (s^{-1})	$(3.68 \pm 0.15) \times 10^{-4}$	$(6.94 \pm 0.46) \times 10^{-4}$	$(1.74 \pm 0.10) \times 10^{-3}$	$(3.28 \pm 0.10) \times 10^{-3}$

Table 1 The fitting results of the real-time sensor response curves shown in Figure 3.8 (a) that are fitted with Equation (6). The table lists the extracted S_{eq} and ($k_{on}n$ + k_{off}) parameters for n = 60 fM, 600 fM, 3 pM, and 6 pM.

To evaluate k_{on} and k_{off} parameters, the extracted ($k_{on}n$ + k_{off}) data are plotted as a function of TNF-α concentration (n) (see Figure 3.10 (c)). The linear fitting results in rate constants of k_{on} = (5.03 ± 0.16) × 10^8 M^{-1} s^{-1} and k_{off} = (3.44 ± 0.15) × 10^{-4} s^{-1}. It should be noted that this fit is not sensitive to the dissociation rate (k_{off}) because of its small numerical value. To achieve a more precise quantification of k_{off}, we directly measured the real-time dissociation kinetics of the antibody-(TNF-α) pair. Specifically, two as-functionalized MoS_2 transistor biosensors were incubated in solutions with TNF-α concentration of 600 fM and 3 pM, respectively. The incubation time was more than 2 hours so that antibody-(TNF-α) association/dissociation processes reached to the equilibrium state. Afterwards, these fully incubated sensors were rinsed with pure buffer liquid flow and the calibrated sensor responses were recorded as a function of the lapsed time, as displayed in Figure 3.12. Figure 3.12 displays that the sensor responses decreased with time, which was attributed to the unbinding events. The response curve measured from the device incubated with TNF-α concentration of 600 fM can be well fitted with a monoexponential decay function (*i.e.*, the desorption equation expressed in Equation (7)). In Equation (7), S_r represents the sensor response corresponding to the areal density of bound molecule residues after the desorption process. This fit results in k_{off} = (1.97 ± 0.08) × 10^{-4} s^{-1}, from which the affinity equilibrium constant K_D can be also estimated to be K_D= k_{off}/k_{on}= 392 fM. This K_D value is also consistent with those extracted from the equilibrium-state sensor responses (*i.e.*, K_D values extracted in Figure 3.4 and 3.6). From this fit, S_r is extracted to be 3.0 ± 0.2 V and S_{eq} is 9.2 ± 0.4 V. This implies that ~30% of bound TNF-α molecules are expected to remain absorbed on the sensor even after a long rinsing process.

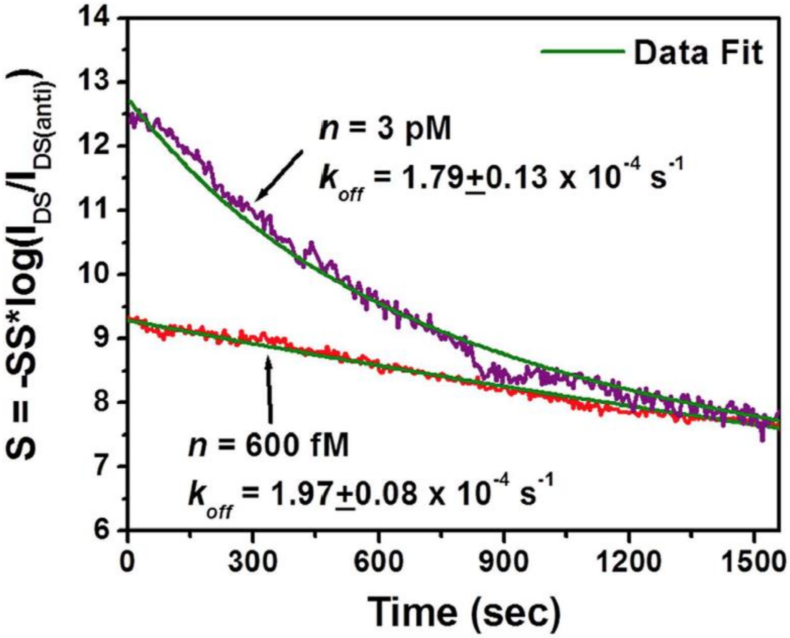

Figure 3.12 Time-dependent dissociation kinetics of the antibody-(TNF-α) pair measured from two MoS_2 transistor sensors that were incubated in solutions with TNF-α concentrations of n = 600 fM and 3 pM for about 2 hours and subsequently rinsed with the pure buffer liquid flow.

$$S = (S_{eq} - S_r)e^{-k_{off}t} + S_r \qquad (7)$$

$$S = (S_{eq} - S_2 - S_r)e^{-k_{off}t} + S_2 e^{-k_2 t} + S_r \qquad (8)$$

The response curve measured from the device incubated with TNF concentration of 3 pM can be hardly fitted with monoexponential Equation (7). We notice that it can be fitted with a bi-exponential decay equation (Equation (8)). This fit results in $S_{eq} = 13.6 \pm 1.0$ V, $S_2 = 4.5 \pm 0.2$ V, $S_r = 2.9 \pm 0.3$ V, $k_2 = (2.0 \pm 0.16) \times 10^{-3}$ s^{-1}, and $k_{off} = (1.79 \pm 0.13) \times 10^{-4}$ s^{-1}. As reported by several previous works [104, 136, 137], such a bi-exponential behavior of sensor responses is probably due to the multivalent antigen-antibody binding, which may become more prominent with increasing the analyte concentration. This explanation is reasonable because the antibody used in this work is polyclonal. To fully understand the association/dissociation kinetics of multivalent binding/unbinding processes, a more complicated model for describing antibody-(TNF-α) binding is required.

Finally, it should be noted that for our current MoS_2 transistor sensors, the calibrated sensor responses do not explicitly depend on HfO_2 layer thickness (t_{HfO2}). All sensors discussed above have 30 nm thick HfO_2 effective layers. To further experimentally verify that the sensor responses of our sensors do not strongly depend on HfO_2 layer thickness (t_{HfO2}), we fabricated additional sensors with $t_{HfO2} = 60$ nm. Figure 3.13 (a) shows the transfer characteristics of an exemplary sensor with $t_{HfO2} = 60$ nm, which were measured from a set of incremental TNF-α concentrations. From such transfer characteristics, we extracted calibrated subthreshold-regime responses (S) at $V_G = -25$ V ($V_T \sim -10$ V) and plotted them as a function of TNF-α concentration (n) (see the red stars shown in Figure 3.13 (b)). This S-n relationship is consistent with those measured from the sensors with t_{HfO2} = 30 nm. This result proves that the calibrated sensor response values do not strongly depend on the HfO_2 effective layer thickness.

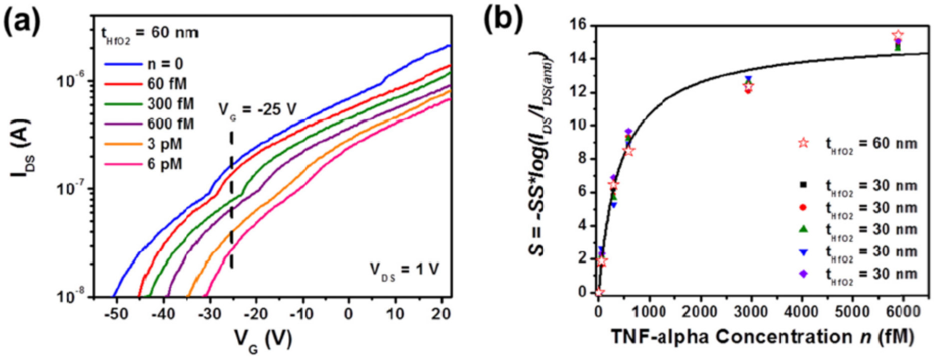

Figure 3.13 Sensor response measured in the subthreshold regime of a MoS_2 transistor biosensor with a 60 nm thick HfO_2 effective layer (*i.e.*, t_{HfO2} = 60 nm): (a) transfer characteristics of the MoS_2 transistor sensor with t_{HfO2} = 60 nm, which were measured from a set of incremental TNF-α concentrations (*i.e.*, n = 0, 60 fM, 300 fM, 600 fM, 3 pM, and 6 pM; (b) The calibrated subthreshold-regime responses (S) measured from this sensor (labeled as red stars) with respect to TNF-α concentration (n).

3.4 Summary

In conclusion, we presented significant device physics and metrics for calibrating the responses of MoS_2 transistor biosensors and demonstrated that multiple such sensors can be utilized to enable quantification of low-abundance biomarker molecules as well as the affinities and kinetics of antibody-mediated binding events. In particular, our biosensors exhibited a TNF-α detection limit at least as low as 60 fM. Such a low detection limit can be obtained in both linear and subthreshold regimes of MoS_2 transistors. We further observed that the sensors operated in the subthreshold regime showed the higher current sensitivities in comparison with those in the linear regime.

Such high subthreshold-regime sensitivities hold significant potential to further lower the TNF-α detection limit. In both transport regimes, the measured current signals can be normalized into response quantities independent of the transistor performance, which can effectively reduce the effect of sensor-to-sensor variation on biodetection results. Based on this calibration method, all sets of our biosensors can generate very consistent sensor responses with respect to TNF-α concentration and therefore a standard curve for TNF-α quantification. From this standard curve, the equilibrium constant of the antibody-(TNF-α) pair was extracted to be $K_D = 369 \pm 48$ fM from linear-regime responses (or $K_D = 424 \pm 70$ fM from subthreshold-regime responses). Furthermore, the real-time association/dissociation processes of the antibody-(TNF-α) pair were also quantified using multiple sensors. The association/dissociation rates were extracted to be $k_{on} = (5.03 \pm 0.16) \times 10^8$ M^{-1} s^{-1} and $k_{off} = (1.97 \pm 0.08) \times 10^{-4}$ s^{-1}, respectively. This work laid an important foundation for leveraging the excellent electronic properties of emerging atomically layered semiconductors in bio-assay applications as well as advanced the critical research capability in analyzing the biomolecule interactions with fM-level detection sensitivities. Notably, such capability would enable selection of antibodies with a high binding constant with respect to a specific target biomarker molecule, thereby offering a means to further enhance the selectivity and fidelity of immunoassay.

Chapter 4

Two Different Device Physics Principles for Operating MoS_2 Transistor Biosensors with Femtomolar-Level Detection Limits

4.1 Introduction

MoS_2, one of transition metal dichalcogenides (TMDCs), has been studied as an attractive nanoelectronic material for making field-effect transistor (FET) biosensors [42, 43], because the transport characteristics of monolayer or few-layer MoS_2 FET channels are extremely sensitive to external stimulations, such as antigen-antibody binding events; 2D MoS_2 surfaces have an extremely low density of electron scattering centers, which can result in a low detection noise; and also semiconducting MoS_2 FETs show much higher On/Off ratios and therefore the higher detection sensitivities in comparison with semi-metallic graphene FETs [53, 138, 139]. Therefore, MoS_2 FET biosensors hold the significant potential to enable single-molecule-level (or fM-level) detection of illness-related biomarkers. To leverage such superior sensing capability of MoS_2 FETs for cost-efficient immunoassay applications, large-scale MoS_2 FET arrays need to be manufactured at an affordable cost. To minimize the manufacturing cost, the sensor structure should be as simple as possible while meeting requirements unique to biosensing. In a conventional way of fabricating a typical FET biosensor based on MoS_2 or other layered materials [140, 141], a dielectric insulating layer (e.g., SiO_2, Al_2O_3, and HfO_2) is deposited on top of the MoS_2 channel for hosting the antibody receptors [42]. The growth of such insulating layers requires exquisite atomic layer deposition (ALD) tools. Moreover, due to the hydrophilic nature of these insulating layers, extra chemical processes need to be performed to introduce additional chemical linkers (*e.g.*, 3-Aminopropyl)triethoxysilane (APTES)) for interfacing the dielectric surface and hydrophobic antibodies [142]. These two concerns could significantly increase the manufacturing cost of MoS_2-based immunoassay chips. Recently, Lee *et al.* demonstrated that the direct antibody functionalization on MoS_2 surface is possible because of the hydrophobicity of MoS_2 layers, which could lower the fabrication complexity and the cost of MoS_2 biosensors [142]. Notwithstanding such a progress, the underlying physics of the device operation still remains unexplored. Additional work is needed for understanding the difference between insulating-layer-coated and insulating-layer-free MoS_2 sensors in their operation principles.

In this chapter, we report different physics principles governing the sensor responses measured from insulating-layer-coated and insulating-layer-free MoS_2 FET sensors. For an insulating-layer-coated sensor, antibody receptors are functionalized on the insulating layer. The charge introduced through antigen-antibody binding is capacitively coupled with the MoS_2 channel and shifts the threshold voltage without significantly changing the transconductance (or mobility). On the other hand, for an insulating-layer-free sensor, in which antibodies are directly grafted on the bare MoS_2 channel, antigen-antibody binding events mainly modulate the ON-state transconductance, which is attributed to the disordered potential formed in MoS_2 layers.

4.2 Methods and Materials

4.2.1 Fabrication and Characterization of MoS_2 Transistor Biosensors

Figure 4.1 (a) displays insulating-layer-coated (left) and insulating-layer-free (right) MoS_2 biosensors. To fabricate such devices, first few-layer MoS_2 flakes (5-7 nm thick) are exfoliated from a bulk MoS_2 ingot and printed onto the device substrates (*i.e.*, p^+-Si substrates coated with 300 nm thermally grown SiO_2) using our previously reported method [125, 126]. After MoS_2 exfoliation, metallic drain (*D*) and source (*S*) contacts are formed using photolithography followed with metal deposition (10 nm Ti/50 nm Au) and lift-off. To produces an insulating-layer-coated sensor, 30 nm HfO_2 is deposited on the MoS_2 channel using ALD. HfO_2 and other high-k dielectric materials can result in less surface scattering as compared to SiO_2 and can also host the antibody functionalization [25, 94]. We also deposit HfO_2 on D/S electrodes to minimize the leakage currents from the analyte solutions to the electrodes. To create an insulating-layer-free sensor, the antibodies are directly functionalized on the bare MoS_2 channel.

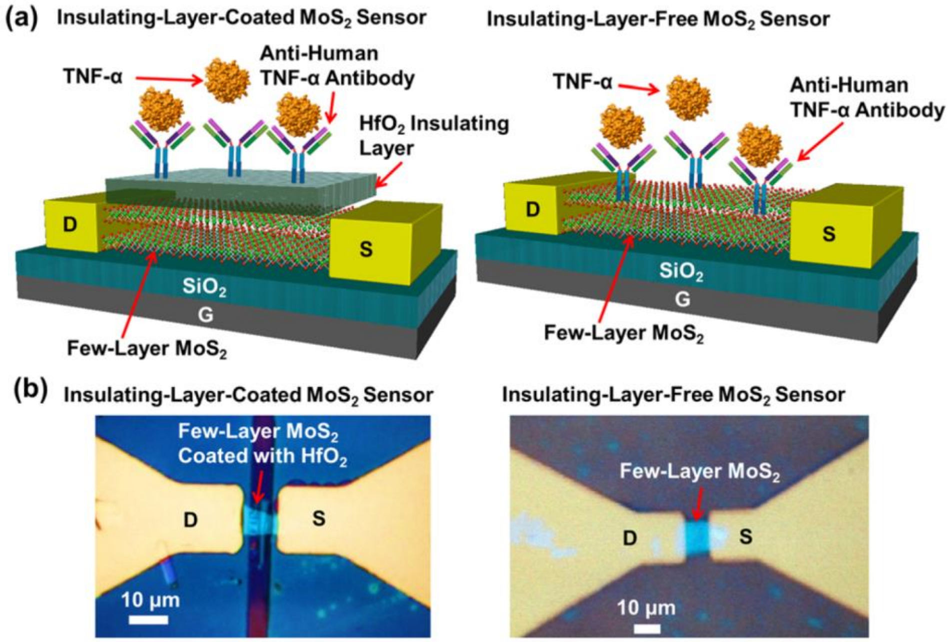

Figure 4.1 Illustrations (a) and optical micrographs (b) of insulating-layer-coated (left) and insulating-layer-free (right) MoS_2 FET biosensors.

4.2.2 Bio-Functionalization of MoS_2 Transistor Biosensors

Figure 4.1 (b) shows the optical micrographs of two exemplary biosensors with (left) and without (right) a 30 nm HfO_2 layer. In this work, we functionalized our sensors with Anti-Human TNF-α antibody receptors for detecting TNF-α molecules. The purified Anti-Human TNF-α (Clone: monoclonal antibody (MAb1) and Isotype: Immunoglobulin G (IgG1)) was purchased from Ebioscience, Inc. The MAb1 antibody has been used for capturing human TNF-α, immunoblotting, and neutralizing the biological activities of TNF-α. The antibody functionalization is described as follow. The sensors are submerged in 5% APTES in ethanol for 1 hour, and then they are washed with phosphate buffered saline (PBS) and blown dry. Afterwards, the sensors are submerged in 5% gluteraldehyde in PBS for 2 hours and rinsed with PBS [42]. Finally, the sensors are incubated with a solution of 50 lg/ml anti-TNF-a antibody for 45 min and subsequently blown dry by N_2 gas. For the TNF-α quantification at the equilibrium state of the (TNF-α)-antibody reaction, we perform the following steps: (1) incubate the sensor in a target TNF-α solution (solvent is 1×PBS; ionic strength is 162.7 mM) for a duration of 20-30 min to assure that the (TNF-α)-antibody reaction has reached to the equilibrium state; (2) briefly rinse away unreacted TNF-α molecules with DI water; and (3) blow dry the device and measure its transfer characteristics (*i.e.*, drain-source current (I_{DS})-gate voltage (V_G) curves) using a semiconductor analyzer. Such an equilibrium-state measurement is performed in the air, and the screening effect is negligible.

4.3 Results and Discussion

4.3.1 Comparison of Insulating-Layer-Coated and Insulating-Layer-Free MoS_2 Transistor Biosensors

Figure 4.2 (a) displays the transfer characteristics of an exemplary insulating-layer-coated sensor, which were measured from a set of incremental TNF-α concentrations (*i.e.*, n = 0, 60 fM, 300 fM, 600 fM, 3 pM, and 6 pM). With increasing n, the I_{DS}-V_G characteristic curve of this sensor shifted toward the positive V_G direction without changing the shape. Such a shape-retaining transition can be further verified by the fact that we can make all I_{DS}-V_G curves from different TNF-α concentrates coincide by using a horizontal shift of them along the V_G-axis, as shown in Figure 4.2 (b). This result indicates that the charges introduced by TNF-α molecules electrostatically affect the free carrier concentration in the MoS_2 channel and induce a shift of the threshold voltage (*i.e.*, ΔV_T measured at the back gate), but these charges do not cause a noticeable change of the ON-state transconductance ($g_m = dI_{DS}/dV_G$) (or the field-effect mobility) of the FET. For such insulating-layer-coated sensors, the response behavior can be well described by the conventional capacitor model [105], and a calibrated sensor response quantity (S) is expressed in Equation (1) [104, 135], where $I_{DS(n=0)}$ is the I_{DS} measured from an as-functionalized sensor (*i.e.*, $n = 0$) biased under a set of fixed V_{DS} and V_G, and I_{DS}-$I_{DS(n=0)}$ indicates the change of I_{DS} induced by the introduction of TNF-α solutions with various concentrations. I_{DS}-$I_{DS(n=0)}$ normalized by the g_m of this sensor creates a sensor response quantity (S) associated with ΔV_T. Here, ΔV_T can be calculated using $\Delta V_T = qd_{SiO2}\sigma_{TNF}/k_{SiO2}\varepsilon_0$, where q is the effective charge introduced by a TNF-α molecule; k_{SiO2} and d_{SiO2} are the dielectric constant and thickness of the SiO_2 back-gate dielectric, respectively; ε_0 is the vacuum permittivity; and σ_{TNF} is the areal density of TNF-α molecules bound to the sensor area.

Figure 4.2 (c) displays the transfer characteristics of an exemplary insulating-layer-free sensor, measured from n = 0, 60 fM, 600 fM, 6 pM, and 60 pM. This sensor exhibited a very different response behavior from insulating-layer-coated sensors. With increasing n, the I_{DS}-V_G curve of this sensor did not significantly shift along the V_G-axis, but exhibited a proportional scale-down along the I_{DS}-axis (*i.e.*, the I_{DS} (or g_m) values proportionally decreased with increasing n). Such a proportional reduction of I_{DS} (or g_m) values can be further verified by the fact that we can make all I_{DS}-V_G curves from different TNF-α concentrations coincide by multiplying their I_{DS} values with appropriate factors, as shown in Figure 4.2 (d). This result indicates that when TNF-α molecules are bound to an insulating-layer-free senor, they can result in reduction of the g_m (or the mobility) of the FET. Such a response behavior cannot be described by the simple capacitor model. For such insulating-layer-free sensors, a tentative calibrated response quantity is the relative change of the ON-state I_{DS} under a given V_G, as expressed by the Equation (2).

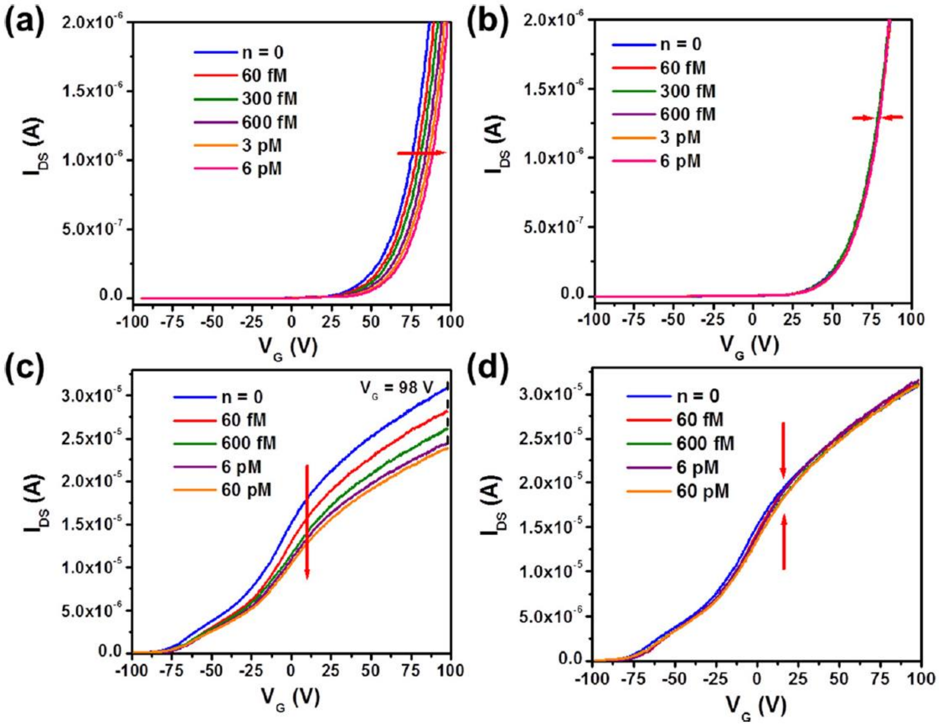

Figure 4.2 Comparison of sensor responses measured from MoS_2 FET biosensors with and without an insulating layer: (a) transfer characteristics of a sensor with a 30 nm HfO_2 insulating layer, measured at various TNF-α concentrations of $n = 0$, 60, 300, 600, 3000, and 6000 fM. We can make these transfer characteristic curves coincide by using a horizontal shift along the V_G-axis, as shown in (b). (c) transfer characteristics of an insulating-layer-free sensor measured at n = 60, 600, 6000, and 60 000 fM. We can make these transfer characteristic curves coincide by multiplying them with different factors, as shown in (d).

$$S = -\frac{I_{DS} - I_{DS(n=0)}}{g_m} = \Delta V_T \qquad (1)$$

As demonstrated in Figure 4.2, both insulating-layer-coated and insulating-layer-free sensors can result in a limit-of-detection (LOD) not higher than 60 fM for TNF-α detection. However, the employment of insulating-layer-free sensors can simplify the fabrication of future MoS_2 FET immunoassay chips. In addition, bare MoS_2 sensing areas are naturally hydrophobic and could enable the direct functionalization of a broad variety of antibodies without using complicated linkers, therefore simplifying the functionalization processes [142].

$$S = -\frac{I_{DS} - I_{DS(n=0)}}{I_{DS(n=0)}} \qquad (2)$$

4.3.2 Simulation of Electrostatic Potential Distribution in Insulating-Layer-Coated and Insulating-Layer-Free MoS_2 Channels

Despite the simplicity of insulating-layer-free sensors, to ultimately realize biomarker quantification using such sensors, ones need to understand the device physics governing their response behavior. We tentatively attribute the antigen/ antibody-binding-induced reduction of the g_m values of our insulating-layer-free sensors (Figure 4.2 (c)) to the biomolecule-induced disordered potential in the MoS_2 channels, which can reduce the FET mobility [143-146]. To support this hypothesis, we quasi-quantitatively simulated the electrostatic potential distribution in the MoS_2 channels, which is induced by the charged antigen-antibody pairs. The simulation was performed using an electromagnetics simulation software (Maxwell^{TM}) based on finite-element analysis. In this simulation, the antigen-antibody pairs were modeled as charged pillars randomly and discretely distributed on the sensors (pillar diameter: 4 nm, height: 10 nm, and minimum spacing between pillars: 10 nm). Such a simple model of antigen-antibody pairs is approximately consistent with the geometric dimensions and spatial spacings of real antibody-(TNF-α) pairs bound to a solid sensor surface [147].

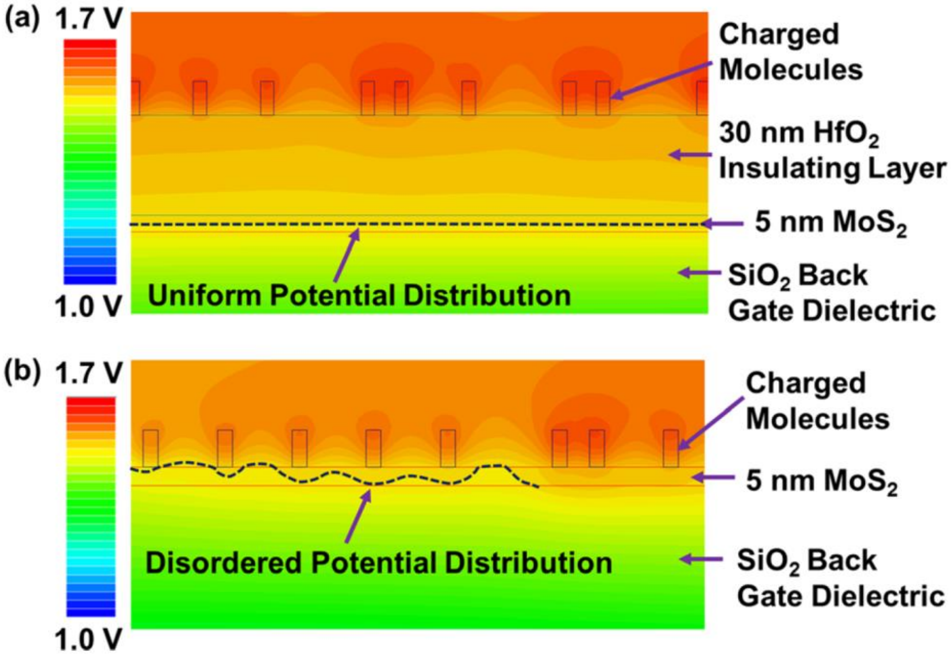

Figure 4.3 Simulation of the electrostatic potential distribution in the MoS_2 channel of (a) an insulating-layer-coated sensor, in which charged molecules are bonded to the HfO_2 insulating layer, and (b) an insulating-layer-free sensor, in which charge molecules are directly bonded to the MoS_2 surface.

Figure 4.3 displays the simulated potential distributions in the MoS_2 channels of (a) an insulating-layer-coated sensor and (b) an insulating-layer-free sensor. For both sensors, the charged molecules induce disordered and corrugated equipotential surfaces in the proximity of molecules. For the insulating-layer-coated sensor, the presence of a 30 nm HfO_2 insulating layer can effectively buffer such a disordered potential distribution and result in relatively flat equipotential surfaces in the MoS_2 channel. Such a uniform field distribution in the MoS_2 channel does not significantly modulate the carrier mobility (or g_m) but only induces a ΔV_T. For the insulating-layer-free sensor, the molecules directly create a disordered/corrugated potential distribution in the MoS_2 channel, which is expected to significantly enhance the scattering and localization probabilities of moving carriers, therefore degrading the carrier mobility (and g_m) of the FET [143-146]. In 2D monolayer or quasi-2D few-layer MoS_2 FET channels, such a disordered potential effect is expected to be more prominent than that in bulk semiconductors because of the 2D confinement of carriers. This simulation result can qualitatively explain the response behavior of our insulating-layer-free sensors.

4.3.3 Static Measurement: Sensor Reponses Measured Using a MoS_2 FET Sensor with a 5 nm Thick HfO_2 Insulating Layer

Additionally, our simulation implies a critical HfO_2 layer thickness of $t_c \sim 5$ nm. When the HfO_2 layer thickness (t_{HfO2}) is thinner than t_c, the biomolecule-induced potential disorder is prominent in the MoS_2 channel and the FET is expected to function as a g_m-modulated sensor, as demonstrated in Figure 4.2 (c) and 4.2 (d). When t_{HfO2} is thicker than t_c, the potential distribution in the MoS_2 channel is uniform and the FET is expected to function as a V_T-modulated sensor, as demonstrated in Figure 4.2 (a) and 4.2 (b). It is further speculated that when t_{HfO2} is close to t_c, the sensor may exhibit a hybrid response behavior involving both g_m and V_T modulations. To test this speculation, we fabricated additional sensors with $t_{HfO2} = 5$ nm $\sim t_c$. Figure 4.4 (a) displays the transfer characteristics of one of such sensors. With increasing TNF-a concentration, the I_{DS}-V_G curve of this sensor indeed underwent a shift toward the positive V_G direction in concurrent with a drop of the g_m. This indicates that the sensors with $t_{HfO2} \sim t_c$ show a hybrid g_m/V_T-modulated character. Such a response behavior can be further confirmed by

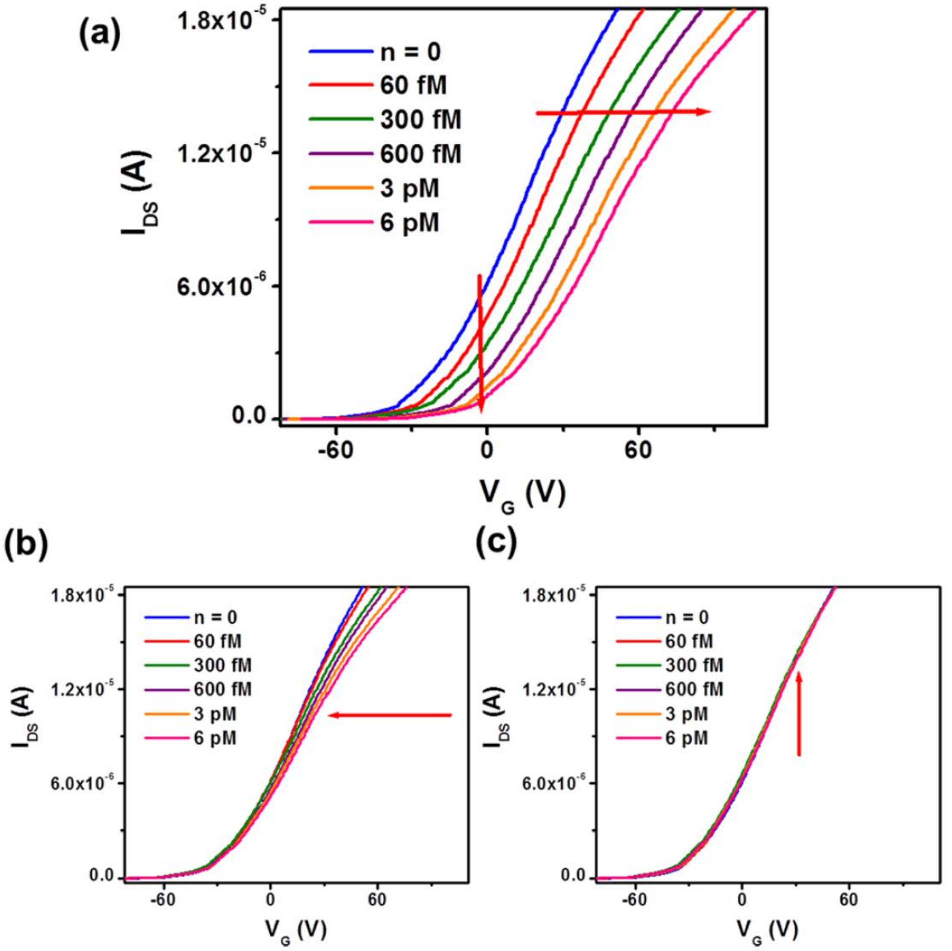

Figure 4.4 Sensor responses measured using a MoS_2 FET sensor with a 5 nm thick HfO_2 insulating layer: (a) transfer characteristics of this sensor measured at various TNF-α concentrations of n = 0, 60, 300, 600, 3000, and 6000 fM. We can make these transfer characteristic curves coincide by horizontally shifting them along the V_G-axis and subsequently multiplying them with different factors, as shown in (b) and (c).

the fact that we can make all I_{DS}-V_G curves coincide by shifting them along the V_G-axis and subsequently multiplying them with different factors, as shown in Figure 4.2 (b) and 4.2 (c). This result strongly supports our simulation model and further implies that HfO_2 layer thickness strongly affects the potential disorder in the MoS_2 channels and determines the sensor response characters.

4.3.4 Repeatability of the Sensor Response Behaviors Using MoS_2 FET Sensors

To evaluate the repeatability of the sensor response behaviors, we identified, fabricated, and characterized additional insulating-layer-coated and insulating-layer-free sensors. Figures 4.5 and 4.6 display the transfer characteristics of all these devices. All insulating-layer-coated sensors exhibit a V_T-modulated behavior, and all insulating-layer-free ones exhibit a g_m-modulated behavior. Their sensor response behaviors are highly consistent with those of the representative devices, as shown in Figure 2. Figure 4.7 plots the response quantity (S)-TNF-α concentration (n) standard curves measured from all (a) insulating-layer-coated and (b) insulating- layer-free sensors. Here, the S values for insulating-layer-coated and insulating-layer-free sensors are calculated using Equation (1) and (2), respectively. The I_{DS} values used for the calculation are measured at $V_G = 98$ V. Figure 4.7 shows that our sensors exhibit a reasonably good device-to-device consistency in their S-n curves. Here, we do not use the Langmuir isotherm model to fit the S-n curves in Figure 4.7. This is because the antigen-antibody binding kinetics on our MoS_2 transistor biosensors may not follow the Langmuir isotherm model. In particular, for the insulating-layer-free sensors, we still lack a suitable physics model to correlate the sensor

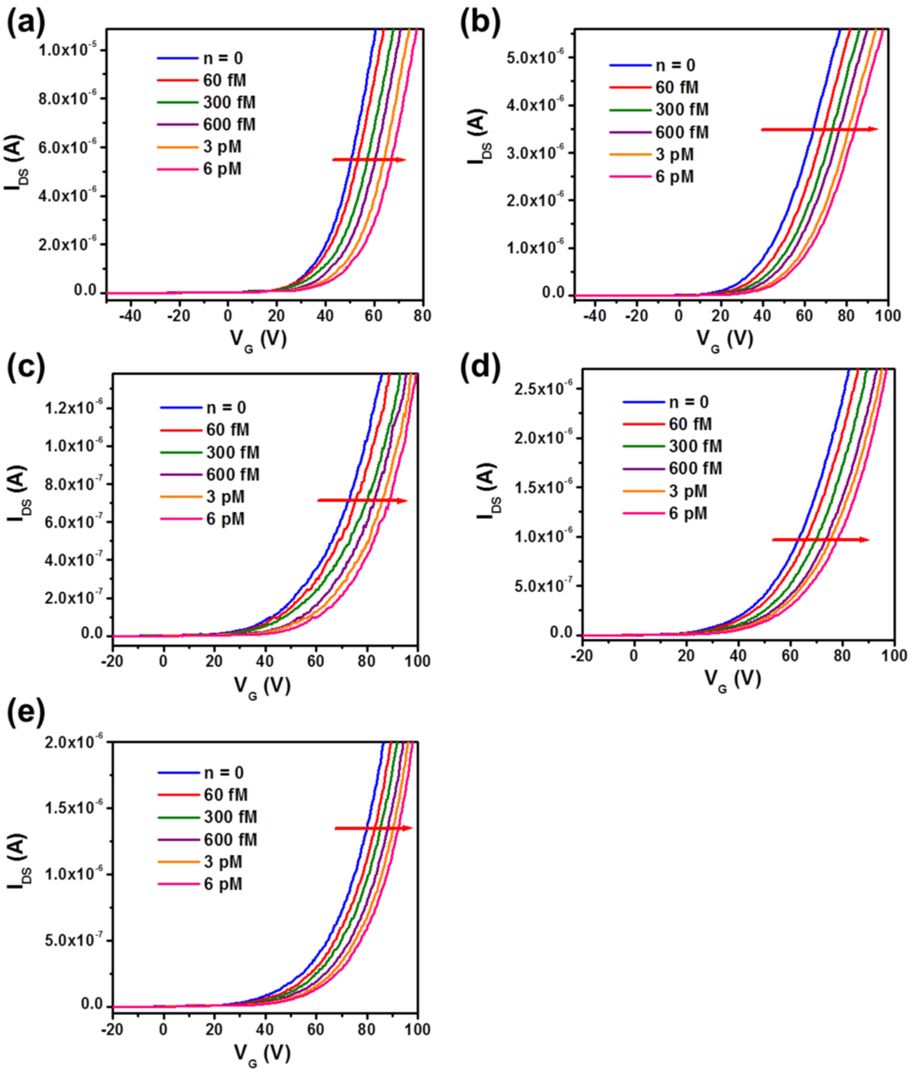

Figure 4.5 Transfer characteristics of five effective-layer-coated MoS_2 FET biosensors (t_{HfO2} = 30 nm). Each of them is subjected to a set of incremental TNF-α concentrations (i.e., n = 0, 60 fM, 300 fM, 600 fM, 3 pM, and 6 pM).

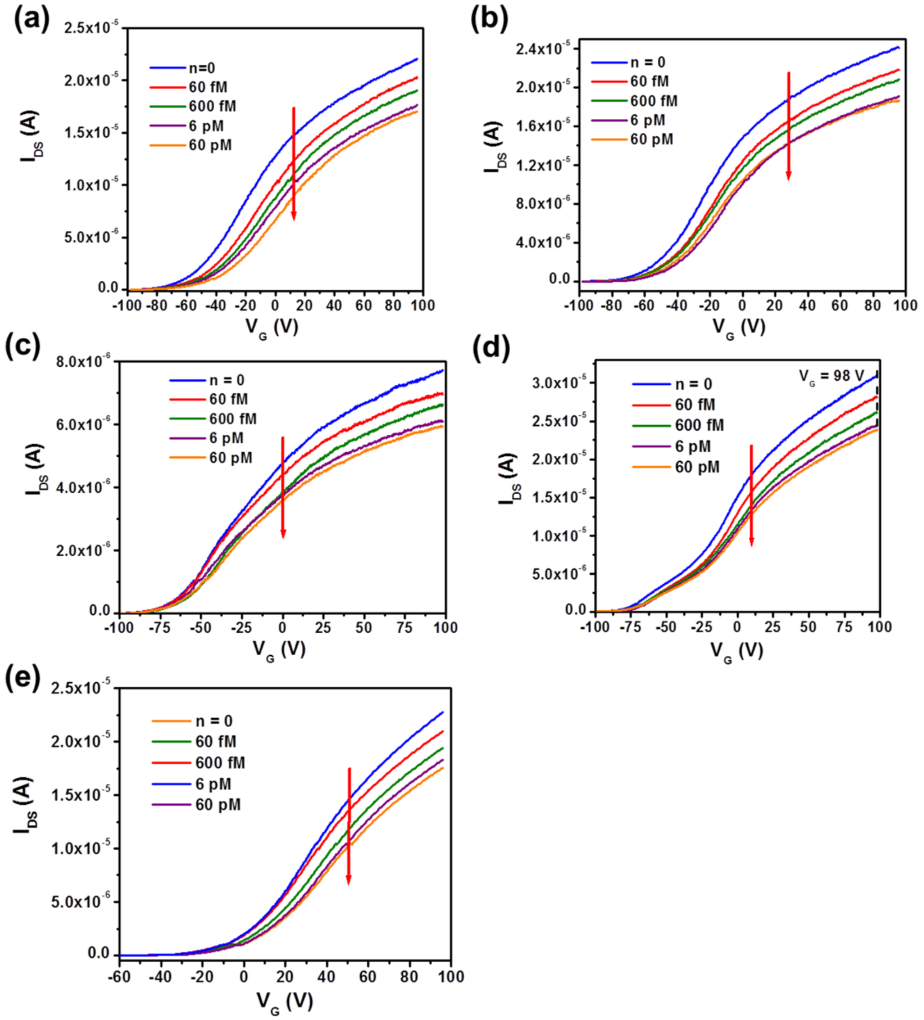

Figure 4.6 Transfer characteristics of five effective-layer-free MoS_2 FET biosensors (t_{HfO2} = 0). Each of them is subjected to a set of incremental TNF-α concentrations (*i.e.*, *n* = 0, 60 fM, 600 fM, 6 pM, and 60 pM).

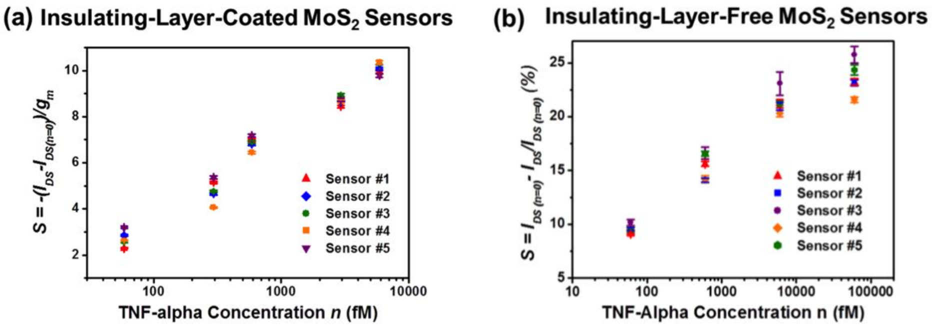

Figure 4.7 The standard curves for TNF-α quantification, acquired from (a) a set of insulating-layer-coated sensors (the ones listed in Figure 4.5), and (b) a set of insulating-layer-free sensors (the ones listed in Figure 4.6).

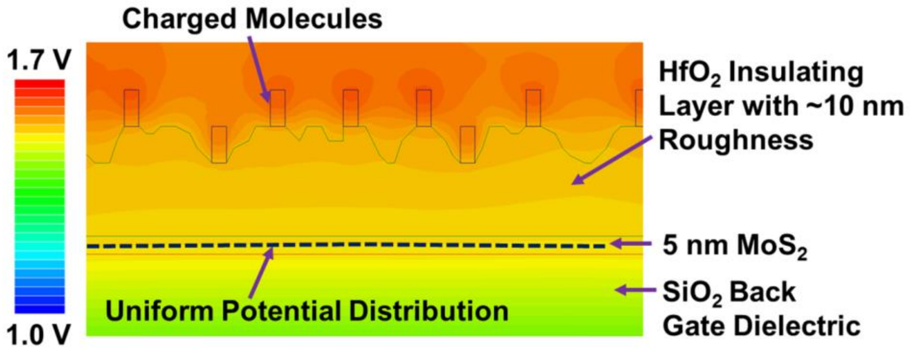

Figure 4.8 Simulation of the electrostatic potential distribution in the MoS_2 channel of an insulating-layer-coated sensor. In this device, the HfO_2 insulating layer has a surface roughness of ~10 nm (average peak-to-valley magnitude).

response quantity (*S*) with the areal occupancy of target biomolecules. For the insulating-layer-coated sensors, although we have a sensor response quantity (*S*) literally proportional to the areal density of bound molecules (see Equation (1)), previous works have shown that the ALD-grown HfO_2 films on 2D layer surfaces show a large roughness, which can make the antigen-antibody binding kinetics deviate from the Langmuir isotherm model [148-150]. Such a new justification about the effect of insulating layer roughness on the antigen-antibody binding kinetics does not undermine our main conclusion, *i.e.*, the introduction of an HfO_2 insulating layer (even a rough layer) can effectively smooth out the antigen-induced disordered potential disturbances in the MoS_2 channel. Specifically, we further simulated the potential distribution in a sensor with HfO_2 roughness of ~10 nm. Figure 4.8 displays that the potential distribution in the MoS_2 channel is still uniform in spite of the HfO_2 roughness.

4.4 Summary

In summary, insulating-layer-coated and insulating-layer-free MoS_2 FET biosensors show V_T-modulated and g_m-modulated responses to antigen-antibody binding events, respectively. Our work proposes that such a difference in the sensor response character could be attributed to the effect of insulating layer thickness on the potential disorder in the MoS_2 FET channels. We also identify a critical insulating layer thickness, around which the sensors exhibit both V_T and g_m-modulated responses. This work advances the critical device physics for understanding and simplifying the FET biosensors based on emerging atomically layered semiconductors.

Chapter 5

Cycle-Wise Operation of MoS_2 and WSe_2 Transistor Biosensors for Rapid Biomolecule Quantification at Femtomolar Levels

5.1 Introduction

Field-effect transistor (FET) biosensors made from emerging layered transition metal dichalcogenides (TMDCs), such as MoS_2 and WSe_2, have exhibited attractive characteristics, such as high biodetection sensitivity, low limit-of-detection (LOD), and good compatibility with planar nanofabrication processes, potentially enabling multiplexing sensor arrays. Specifically, Wang *et al.* and Sarkar *et al.* experimentally demonstrated MoS_2 FET biosensors with femtomolar (fM)-level detection limits [42, 43]. Nam *et al.* established the device physics for calibrating the sensor response signals measured from MoS_2 FET sensors with insulating layers and preliminarily demonstrated the fabrication of MoS_2 FET arrays [49, 151]. Lee *et al.* demonstrated that antibody receptors can be directly grafted on MoS_2 FET channels without using insulating layers, which is due to the hydrophobicity of the MoS_2 surface [142]. Such an insulating-layer-free sensor structure can lower the fabrication complexity as well as the cost of MoS_2 biosensors. Nam *et al.* further found that insulating-layer-free MoS_2 sensors exhibit a higher sensitivity than insulating-layer-coated ones [152]. This was attributed to that two mechanisms, target-molecule-induced doping and target-molecule-induced surface scattering, synergistically contribute to the response signal of an insulating- layer-free sensor, but only target-molecule-induced doping contributes to the response signal of an insulating-layer-coated sensor [152, 153]. Nam *et al.* also demonstrated that WSe_2 FET sensors exhibit a higher sensitivity than MoS_2 FET sensors, which is attributed to the ambipolar transfer characteristics of WSe_2 FETs [153].

In spite of the progress mentioned above, MoS_2 and WSe_2 FET biosensors still suffer seriously from a series of challenges that hinder their practical biosensing applications. Especially, a FET sensor needs to be continuously subjected to a liquid reagent environment for quantifying the time-dependent reaction kinetics of analyte-receptor binding. Such a time-dependent detection capability is a key to realize rapid biomolecule quantification based on sensor response readings at the non-equilibrium states of binding reactions, which could result in very short lapsed times and enable fast real-time immunoassay for quantifying extreme low-abundance biomolecules (*e.g.*, fM-level biomarkers) [154]. However, the electrical signal acquisition process is not generally compatible with such a liquid environment in the sensor. During a typical time-dependent detection process for quantifying the binding reaction kinetics, the sensing FET is electrically biased and constantly exposed to the analyte solution. Here, the applied biases include a gate voltage (V_G) that is used to bias the FET to the linear regime of the transfer characteristic to obtain a high sensitivity as well as a consistent sensor response behavior [49, 153], and a drain-source voltage (V_{DS}) for driving the sensing channel current (I_{DS}). Such continuous electrical stresses in the liquid reagent environment can result in undesirable leakage currents flowing to electrodes and therefore generate high-level electronic noises and false sensor responses, and even electrochemically damage the sensor. It should be noted that even the FET sensor coated with an insulating layer can hardly survive in a long continuous time-dependent detection process (*e.g.*, >1 hour) because of the electric-field-enhanced permeation of reactive ions into the insulating layer [154, 155]. The analyte solutions with different ionic strengths also cause different degrees of the screening effect to the interaction between target molecules and the sensing channel, resulting in inconsistent sensor response signals. Such a screening effect also degrades the biodetection sensitivity of the sensor [156-159]. Another serious issue associated with TMDC-based FET sensors is the hysteretic behavior of the transfer characteristics of such sensors, which is attributed to the gate-modulated charges trapped at TMDC/dielectric interfaces [105]. Such a hysteretic behavior makes the I_{DS} value measured under a given V_G highly dependent on the V_G sweep range, sweep direction, sweep time and loading history, therefore resulting in inconsistent sensor readings. To rule out such indeterminacy of sensor readings due to the hysteresis effect, ones need to measure the complete transfer characteristic curves (*i.e.*, I_{DS}-V_G curves) by sweeping V_G along both positive and negative directions, which is similar to the way for characterizing a FET memory [160-162]. However, this electrical measurement process is not applicable during a continuous time-dependent detection process. Another expedient solution is to constantly bias the FET sensor to the linear (or highly conductive) transport regime, where the indeterminacy of I_{DS} values is relatively smaller than that in the subthreshold regime. However, as discussed above, such a constantly applied gate bias can easily damage the sensor. In addition, during a continuous time-dependent detection process, the nonspecific adsorption of untargeted molecules on the FET sensing channel can also generate false signals. All of these issues seriously limit the applicability of TMDC-based FET biosensors for realizing rapid, highly specific biomolecule quantification using time-dependent sensor response signals or non-equilibrium-state sensor response readings.

In this chapter, we present a cycle-wise time-dependent biodetection method for operating MoS_2/WSe_2-based FET biosensors. Such a cycle-wise process alternatingly sets the FET sensor into incubation, flushing, and electrical measurement steps and therefore avoids the liquid-solution-induced electrochemical damage, screening, and nonspecific adsorption to the sensor. This method can also rule out the indeterminacy of sensor readings due to the hysteretic behaviors of TMDC FETs. This cycle-wise detection method in combination with the superior sensitivity and limit-of-detection (LOD) of MoS_2/WSe_2-based biosensors can enable rapid, low-noise, highly specific biomolecule quantification with fM-level LODs. In this work, we have experimentally achieved time-dependent responses associated with the reaction kinetics of streptavidin-biotin and IL1β-IL1β antibody binding and demonstrated fM-level streptavidin and IL1β quantification in pure as well as complex solutions (*e.g.*, serum) with detection limit of ~1 fM and total incubation time less than 20 min.

5.2 Methods and Materials

5.2.1 Fabrication of MoS_2 and WSe_2 FET Biosensors

The TMDC FETs are produced onto p^+-Si substrates with 300 nm thermally grown SiO_2 layers using a printing approach previously reported by us [151]. The SiO_2 layers are used as the back-gate dielectrics. Such 300 nm thick SiO_2 layers can also enable a simple color coding method for us to quickly identify and locate the MoS_2 and WSe_2 flakes with suitable thicknesses [163]. The thicknesses of printed Few-layer-TMDC channels are specifically controlled to be 5-15 nm. Such TMDC channel thicknesses can result in the optimal field-effect mobility and On/Off ratio values for TMDC FETs [20, 133, 134]. The p^+-Si substrates served as the back gates (*G*). Ti (5 nm)/Au (50 nm) drain (*D*) and source (*S*) contacts to the TMDC channels are created using photolithography followed with metal deposition and lift-off. The channel lengths and widths of as-fabricated TMDC FETs are ~5 μm and ~15 μm, respectively. All electrical measurements are performed using an HP-4145B semiconductor parameter analyzer, which is connected to a Lakeshore™ probe station. Each of the TMDC FETs selected for making a biosensor is integrated with a polydimethylsiloxane (PDMS) block bearing a microfluidic channel (10 mm in length, 200 μm in width, 50 μm in height), as illustrated in Figure 5.1 (a). A motorized syringe pump is used for driving the reagent fluid flows into and out of the microfluidic channel through an inlet/outlet tubing kit (tube diameter: 0.75 mm).

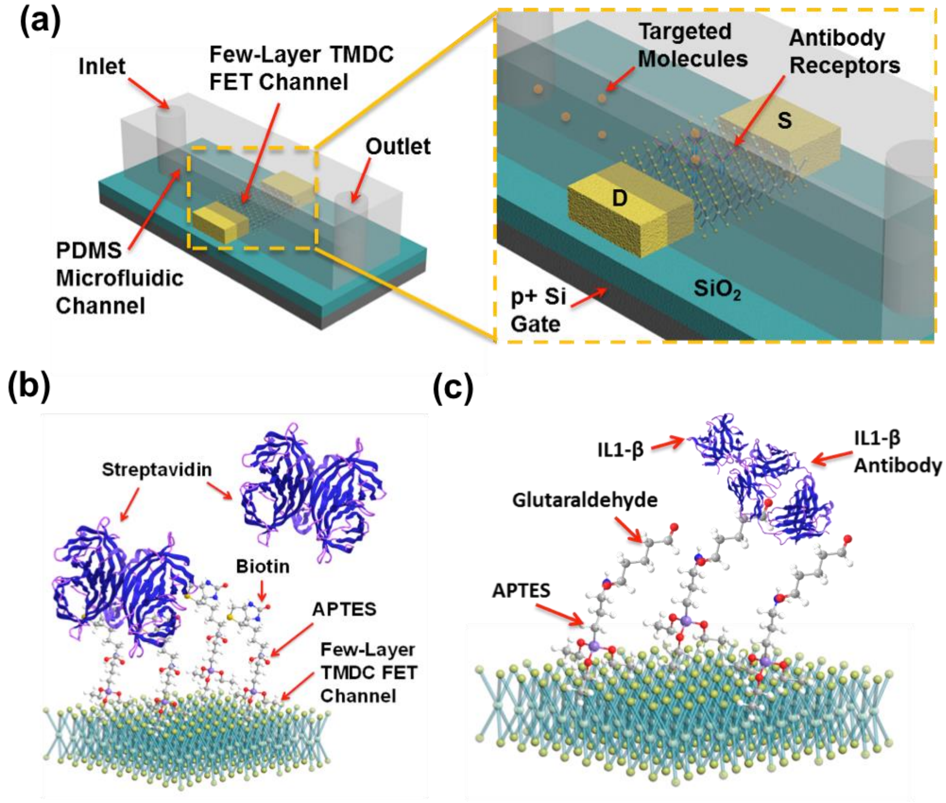

Figure 5.1 Experimental method: (a) illustration of a TMDC-based FET sensor, which is integrated with a PDMS microfluidic channel for enabling the cycle-wise time-dependent detection capability; illustration of a few-layer TMDC FET channel that is functionalized with (b) biotin receptors; (c) IL1β antibody

5.2.2 Bio-Functionalization of TMDC FET Biosensors

An as-fabricated MoS_2 or WSe_2 FET biosensor is incubated in 5% (3-Aminopropyl) triethoxysilane (APTES) in ethanol for 1 hour. After this incubation process, the sensor is rinsed with phosphate buffered saline (PBS) and blown dry by nitrogen gas. For the IL1β antibody functionalization, the sensor is subsequently immersed in 5% gluteraldehyde in PBS for 2 hours followed by rinsing with PBS. Then 0.1 mg/ml NHS-biotin or IL1β antibody in PBS is subsequently incubated on the MoS_2 or WSe_2 channel area for 30 min followed by rinsing with PBS and N_2 blow-dry. During a biodetection process, the integrated PDMS microfluidic system on the FET sensor is used to deliver a series of timely sequenced reagent fluids, including analyte streptavidin or IL1β solutions, pure buffers, and air flows, to the active sensing FET channel.

5.3 Results and Discussion

5.3.1 Cycle-Wise Time-Dependent Biodetection Method for Operating TMDC-Based FET Biosensors

Figure 5.1 (a) illustrates the TMDC-based back-gated FET biosensor under study, which is integrated with a polydimethylsiloxane (PDMS)-based microfluidic channel. A pair of inlet and outlet tubes is connected with the microfluidic channel for delivering various reagent fluids to the FET sensor. Before a biosensing process, the sensing FET channel made from few-layer TMDC (MoS_2 or WSe_2) is functionalized with specific antibody receptors for detecting the target molecules in the analyte solution. During a cycle-wise biodetection and quantification process, the microfluidic structure is operated to deliver a series of timely sequenced reagent fluids to the sensing FET channel and periodically set the sensor into four biodetection stages, including (i) incubation of the sensing channel in the analyte solution containing target molecules for a short but deterministic duration (typically 5-10 min), (ii) flushing the sensing channel using a pure buffer to eliminate unreacted target molecules and untargeted background molecules, (iii) drying the sensing channel using an air flow, and (iv) under such dry condition, electrically measuring the transfer characteristics (*i.e.*, I_{DS}-V_G curves) of the sensing FET by sweeping V_G along both positive and negative directions. Repetitive performance of multiple such incubation-flushing-drying-measurement (IFDM) cycles can acquire a time-dependent response signal associated with the reaction kinetics of analyte-receptor binding.

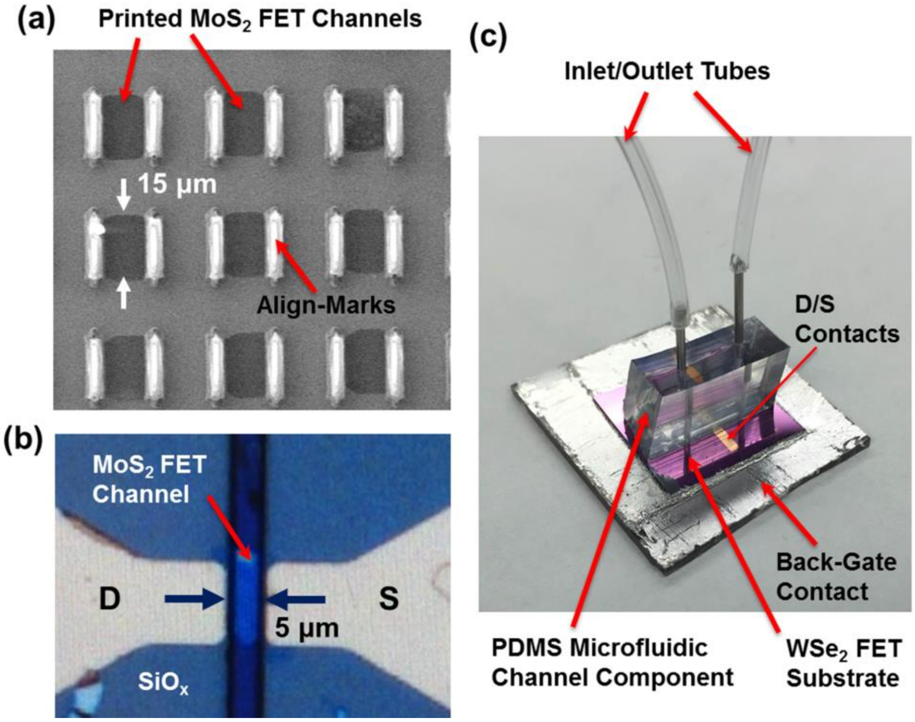

Figure 5.2 Biosensor fabrication and setup: (a) SEM image of several printed few-layer-MoS_2 FET channels; (b) optical micrograph of a representative few-layer-MoS_2 FET biosensor; (c) photograph of a WSe_2 FET sensor integrated with a micro-fluidic channel system. In this work, the few-layer-TMDC (MoS_2 or WSe_2) FET channels were functionalized with biotin receptors, and we experimentally demonstrated time-dependent quantification of streptavidin-biotin binding kinetics.

Figure 5.2 (a) shows the scanning electron micrograph (SEM) of several as-printed few-layer-MoS_2 FET channels. Each of the printed channels is associated with a pair of Ti/Au align-marks, which are used for locating the FET channel specifically selected for making a working biosensor. Figure 5.2 (b) displays the optical micrograph of a representative TMDC FET biosensor consisting of a few-layer MoS_2 channel (thickness ~ 5 nm), a 300 nm thick SiO_2 back gate dielectric layer, a p^+-Si back gate, and a pair of metallic drain/source (*D/S*) contacts (10 nm Ti/50 nm Au). The FET channel length and width are 5 and 15 μm, respectively. Figure 5.2 (c) shows the photograph of a WSe_2 FET sensor integrated with a PDMS microfluidic channel. This microfluidic channel is connected with a motorized syringe pump (not shown in Figure 5.2 (c)) through a pair of inlet/outlet tubes. As demonstrated in Figure 5.2 (c), we can operate this pump/tubing system to deliver timely sequenced reagent fluids to the FET sensing channel for performing IFDM detection cycles.

5.3.2 Time-Dependent Sensor Responses with 30 fM Pure Streptavidin (MoS_2 FET Biosensor)

Figure 5.3 shows the time-dependent sensor responses to a 30 fM solution of pure streptavidin, which were measured using a representative n-type MoS2 sensor (Figure 5.3 (a) and (b)) and a representative ambipolar WSe_2 sensor (Figure 5.3 (c)-(f)). Both sensors were operated using the cycle-wise detection method discussed above, and for each IFDM cycle, the incubation time was T_i = 10 min. In the following discussion, the sensor responses are analyzed as a function of accumulative incubation time (t), which is defined as $t = nT_i$ (here, n is the number of already performed IFDM cycles). Specifically, Figure 5.3 (a) shows the transfer characteristic (*i.e.*, back-gate voltage (V_G) - drain-source current (I_{DS})) curves of the MoS_2 sensor measured at different t values ranging from 0 to 110 min. For each t, two transfer characteristic curves were measured. One was measured

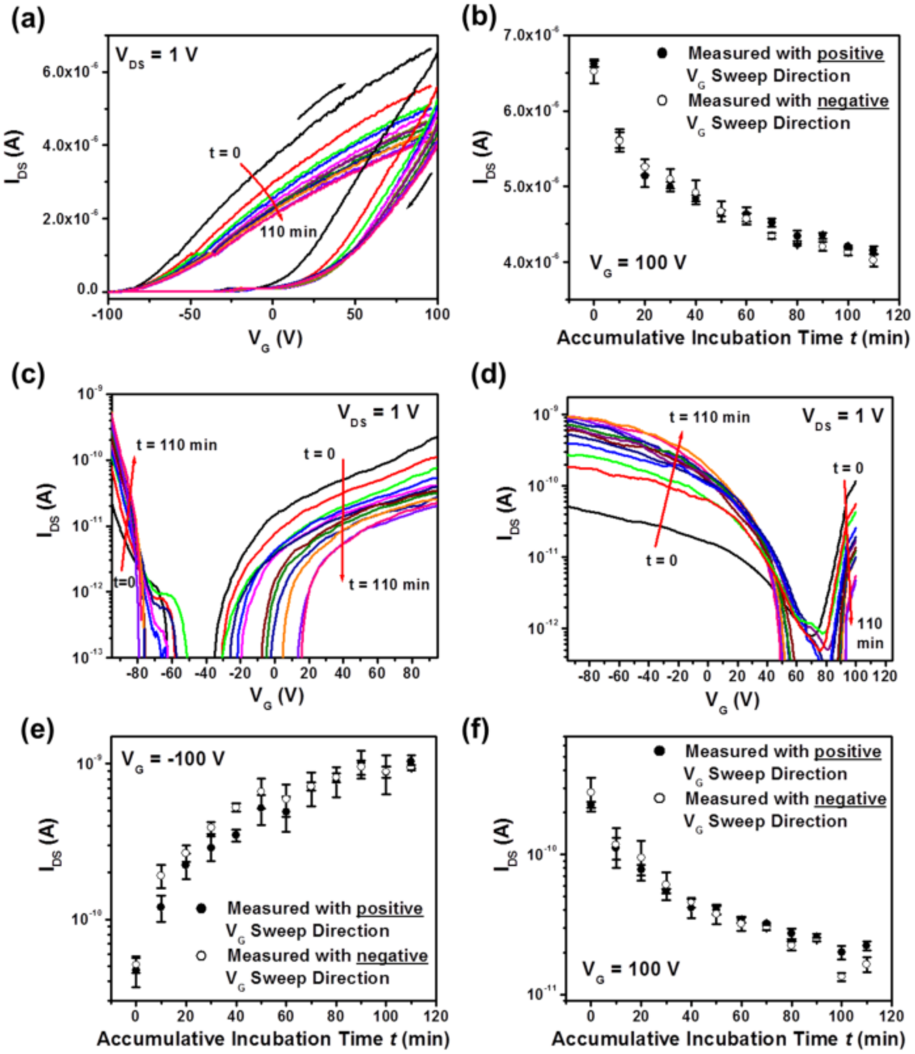

Figure 5.3 Time-dependent sensor responses to a 30 fM solution of pure streptavidin measured using a pair of representative MoS_2 and WSe_2 FET biosensors: (a) I_{DS}-V_G curves of the MoS_2 sensor measured at different accumulative incubation times t ranging from 0 to 110 min (these curves were measured with both positive and negative V_G sweep directions); (b) I_{DS}-t response signals captured from the t-dependent I_{DS}-V_G curves in (a) at V_G = 100 V; (c) and (d) t-dependent I_{DS}-V_G curves of the WSe_2 sensor measured with positive and negative V_G sweep directions, respectively; (e) and (f) I_{DS}-t response signals captured from the p-type (at V_G = -100 V) and n-type (V_G = 100 V) branches of the t-dependent I_{DS}-V_G curves of the WSe_2 FET, respectively.

with positive V_G sweep direction (*i.e.*, from -100 to 100 V, which is referred to as "positively-scanned curves" below), and the other was measured with negative V_G sweep direction (*i.e.*, from 100 to -100 V, which is referred to as "negatively-scanned curves" below). Although this MoS_2 sensor exhibits a prominent hysteretic behavior in its transfer characteristics, both sets of the positively and negatively-scanned I_{DS}-V_G curves measured from this sensor show similar I_{DS}-reduced response behaviors with increasing accumulative incubation time t. To quantify the time-dependent reaction kinetics of biotin-streptavidin binding, the I_{DS} values measured at a given V_G are captured and plotted as a function of accumulative incubation time t. To minimize the indeterminacy of such $I_{DS} – t$ response signals due to the hysteresis of I_{DS}-V_G curves, $I_{DS} – t$ signals should be obtained in the highly conductive regime of I_{DS}-V_G characteristic curves (*e.g.*, V_G = 100 V for our n-type MoS_2 FETs). Figure 5.3 (b) plots the $I_{DS} – t$ response signals captured from the t-dependent I_{DS}-V_G curves in Figure 5.3 (a) (at V_G = 100 V). Figure 5.3 (b) shows that the $I_{DS} – t$ signals obtained from positively and negatively-scanned I_{DS}-V_G curves are consistent with each other, and the hysteresis-induced indeterminacy of I_{DS}-t signals can be ruled out.

Figures 5.3 (c) and (d) display the positively and negatively-scanned t-dependent I_{DS}-V_G curves of the WSe_2 sensor, respectively. For both sets of the I_{DS}-V_G curves, the t values range from 0 to 110 min. The WSe2 FET exhibits an ambipolar transport property. In the p-type branch of I_{DS}-V_G curves, the WSe_2 FET exhibits an I_{DS}-enhanced response behavior with increasing t, whereas in the n-type branch, it exhibits an I_{DS}-reduced response behavior with increasing t. Reliable I_{DS}-t signals with the minimal indeterminacy due to the hysteretic behavior of I_{DS}-V_G curves can be obtained from both highly conductive p-type and n-type regimes of I_{DS}-V_G curves (*e.g.*, V_G = -100 V and 100 V for this WSe_2 FET). Figures 5.3 (e) and (f) plots the I_{DS}-t response signals captured at

V_G = -100 V (*i.e.*, p-type I_{DS}-t responses) and 100 V (*i.e.*, n-type I_{DS}-t responses), respectively. Figures 5.3 (e) and (f) also shows that for either p-type or n-type sensor response cases, the I_{DS}-t signals obtained from positively and negatively-scanned I_{DS}-V_G curves are highly consistent with each other. This work demonstrates that the IFDM cycle-wise method for operating MoS_2 and WSe_2 FET sensors can generate reliable time-dependent sensor response signals for quantifying the kinetics of binding reactions and rule out the indeterminacy of sensor readings due to the hysteresis of the transfer characteristics of such FETs.

5.3.3 Comparison of the Time-Dependent Response Signals Obtained Using IFDM Cycle-Wise and Continuous Detection Methods

We characterized two MoS_2 FET sensors fabricated in the same fabrication batch for a direct comparison of the time-dependent response signals measured using the cycle-wise method and the regular continuous detection method. Figure 5.4 shows these two sensors' responses to the pure 30 fM streptavidin solution. Figure 5.4 (a) shows the t-dependent I_{DS}-V_G characteristic curves measured using one of the MoS_2 sensors, which was operated using the cycle-wise method (T_i = 10 min). An I_{DS}-t signal can be captured from the highly conductive n-type transport regime (*i.e.*, V_G = 100 V) of the I_{DS}-V_G curves plotted in Fig. 5.4 (a). To further minimize the effect of the device-to-device variation in absolute I_{DS} values on the comparison, we used the relative change in I_{DS} (*i.e.*, S = 100% × [$I_{DS}(t) – I_{DS}(t = 0)$]/ $I_{DS}(t = 0)$) with respective to the accumulative incubation time (t) as a calibrated time-dependent sensor response signal. Here, S can also serve as the measure of the biodetection sensitivity. Figure 5.4 (b) plots the *S*-*t* response signal measured from the MoS_2 sensor that was operated using the cycle-wise method (solid circles). The other MoS_2 FET sensor was used to continuously measure the electrical signal associated with the time-dependent reaction kinetics of biotin-streptavidin binding. In particular, the sensor was continuously biased with a back-gate voltage (V_G) of 100 V and a drain-source voltage (V_{DS}) of 1 V. Since the 30 fM streptavidin solution was introduced into the sensor, the instant I_{DS} signal had been being continuously recorded as a function of *t*. This I_{DS}-*t* signal was also calibrated into the signal of *t*-dependent relative change in I_{DS} (*i.e.*, the *S*-*t* signal), which was also plotted in Figure 5.4 (b) (the solid line). In comparison with this *S*-*t* signal obtained using the continuous detection method, the *S*-*t* signal obtained using the IFDM cycle-wise method exhibits the larger signal magnitude (*i.e*., the higher sensitivity) and the smaller relative error of the signal magnitude (*i.e*., the higher signal-to-noise ratio) at a given accumulative incubation time. The relatively weaker magnitude of the *S*-*t* signal obtained using the continuous method is attributed to the Debye screening effect of the liquid solution, which can weaken the electrostatic coupling between the charges of target molecules and the FET channel, resulting in the lower sensitivity [105, 157-159]. The IFDM cycle-wise method can address this issue through physically isolating the incubation and measurement stages during an IFDM cycle. This cycle-wise method can also eliminate the electrical noise from the liquid solution and therefore result in the lower LOD. Additionally, as shown in Figure 5.4 (b), the MoS_2 sensor operated using the continuous method failed at t ~ 50 min. Our other TMDC FET sensors, when operated using the continuous method, also usually fail within one hour of the operation. Such a poor durability is attributed to the net effect of the electrical stresses continuously applied to the FET channel and the continuous exposure of the sensor to the liquid environment, which can lead to electrochemical or thermal damage to the sensing channel. However, the similar TMDC sensors, if operated using the IFDM cycle-wise method (T_i: 5-10 min), can properly work for at least five hours without damage. Therefore, this comparison work indicates that the TMDC FET sensors operated using the cycle-wise method exhibit the better durability, the higher sensitivity, and the higher signal-to-noise ratio in comparison with those operated using the continuous detection method.

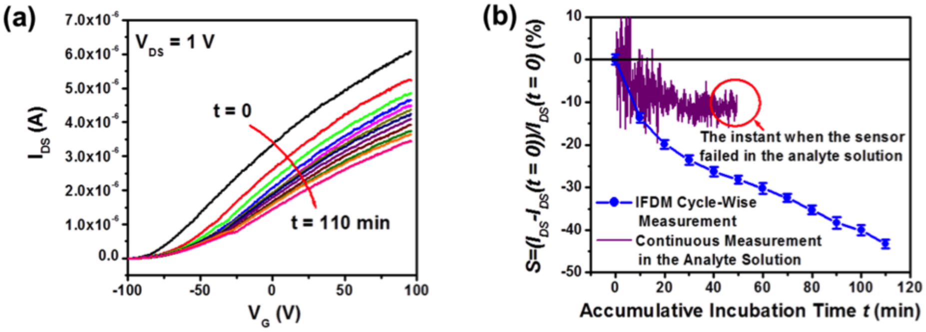

Figure 5.4 Comparison between a MoS_2 FET biosensor operated using the IFDM cycle-wise method and another similar sensor operated using the regular continuous detection method in their responses to a 30 fM solution of pure streptavidin: (a) *t*-dependent I_{DS}-V_G characteristic curves of the sensor operated using the cycle-wise method; (b) the *S*-*t* response signals obtained using the IFDM cycle-wise method (solid circles) and the regular continuous detection method (the solid line).

5.3.4 Detection Specificity of the TMDC FET Biosensors Operated by the IFDM Cycle-Wise Method

To evaluate the detection specificity of the TMDC FET biosensors operated by the IFDM cycle-wise method, we further performed two experiments to test time-dependent quantification of biotin-streptavidin binding reaction kinetics in complex solutions. In the first experiment, we characterized four MoS_2 FET biosensors, which were fabricated in the same batch and have very similar transfer characteristics. Two of them (sensors #1 and #2) were used to quantify 30 fM streptavidin in a pure solution. The other two sensors (sensors #3 and #4) were used to quantify 30 fM streptavidin in a solution that also contained 60 fM tumor necrosis factor alpha (TNF-α). The processing parameters of the IFDM cycle-wise method are the same as those used for the experiments discussed above. Figure 5.5 shows the t-dependent I_{DS}-V_G characteristic curves of these four MoS_2 FET sensors, which were measured using the IFDM cycle-wise method (T_i = 10 min). Figure 5.6 (a) displays four sets of S-t signals respectively captured from the t-dependent I_{DS}-V_G curves of these four MoS_2 sensors (all I_{DS} and S data were captured at V_G = 100 V). These four sets of S-t signals are consistent with each other. This indicates that the presence of 60 fM TNF-α in the analyte solution does not significantly affect the t-dependent sensor response to 30 fM streptavidin. The slight difference among these four S-t curves is attributed to the slight sensor-to-sensor variation in transport characteristics.

In the second experiment, two WSe_2 FET biosensors were fabricated in the same batch. One sensor (sensor #1) was used to quantify 30 fM streptavidin in a pure solution, and the other sensor (sensor #2) was used to quantify 30 fM streptavidin in a serum solution (Merck KGaA, Serum matrix (Contains 0.08% Sodium Azide), 20 times dilution in DI water). Figure 5.7 displays the t-dependent I_{DS}-V_G characteristic curves of these two WSe_2 FET sensors, which were measured using the IFDM cycle-wise method (T_i = 10 min). Figures 5.6 (b) and (c) displays the *S*-*t* response signals captured from the p-type (V_G = -100 V) and n-type (V_G = 100 V) regimes of the *t*-dependent I_{DS}-V_G curves of these two WSe_2 sensors, respectively. Figures 5.6 (b) and (c) shows that for both p-type and n-type sensor readings, the *S*-*t* response to 30 fM streptavidin in the serum solution is highly consistent with the *S*-*t* response to 30 fM streptavidin in the pure streptavidin solution. The complex protein background in the serum solution does not significantly affect the *t*-dependent sensor readings associated with the specific concentrations of target molecules. These two comparison experiments have demonstrated that the MoS_2

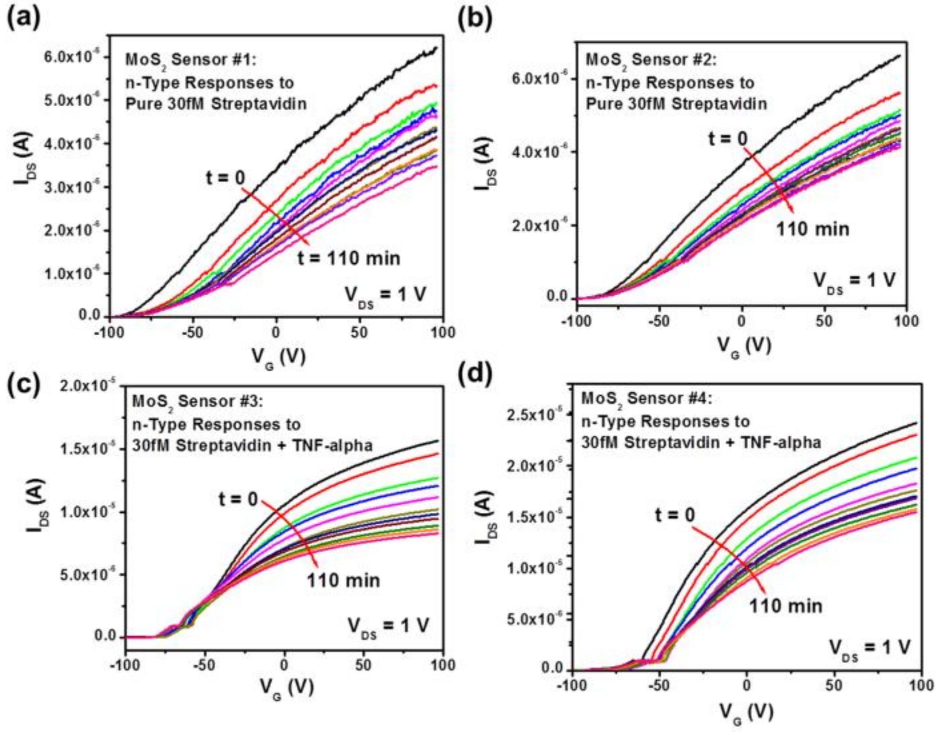

Figure 5.5 IFDM cycle-wise responses (T_i = 10 min) of four MoS_2 FET biosensors that were fabricated in the same fabrication batch: t-dependent I_{DS}-V_G characteristic curves of Sensors #1 (a) and #2 (b), which were measured in a pure solution of 30 fM streptavidin, and Sensors #3 (c) and #4 (d), which were measured in a mixed solution containing 30 fM streptavidin and 60 fM tumor necrosis factor alpha (TNF-α).

and WSe$_2$ FET biosensors operated using the IFDM cycle-wise method exhibit a high biodetection specificity. This is attributed to the flushing step in an IFDM cycle, which can effectively remove non-specifically adsorbed molecules from the FET sensing channel, therefore minimizing the false sensor responses. Furthermore, two-dimensional TMDC surfaces usually have very low friction coefficients and exhibit very low adhesion

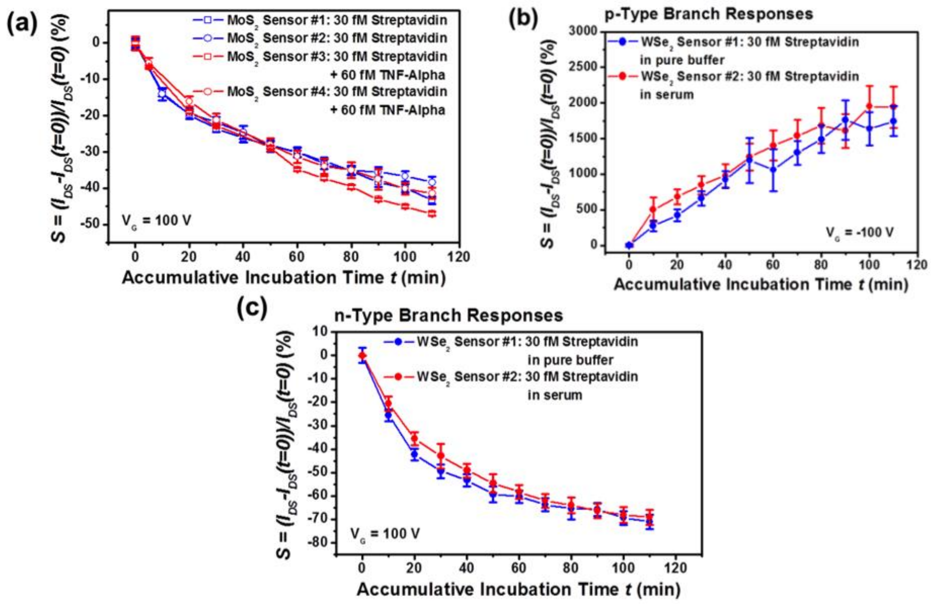

Figure 5.6 Sensor responses to targeted streptavidin molecules in different solutions: (a) *S*-*t* responses, measured from four n-type MoS$_2$ FET sensors, to 30 fM streptavidin in a pure solution (sensors #1 and #2) and a solution also containing 60 fM TNF-α (sensors #3 and #4); (b) p-type and (c) n-type *S*-*t* responses, measured from two ambipolar WSe$_2$ FET sensors, to 30 fM streptavidin in a pure solution (sensor #1) and a serum solution (sensor #2).

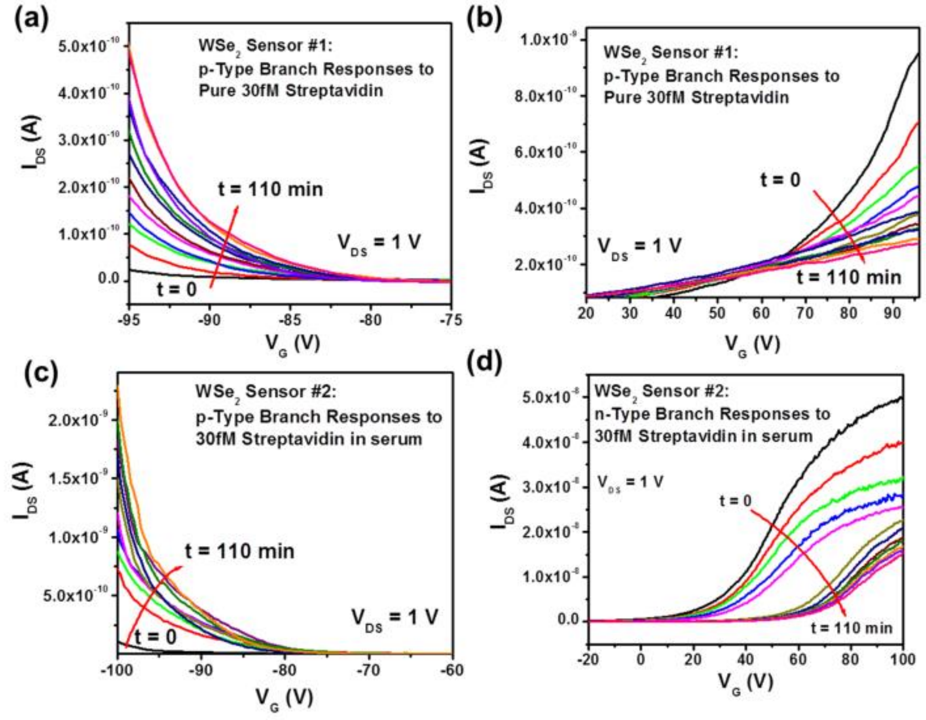

Figure 5.7 IFDM cycle-wise responses, measured from two ambipolar WSe_2 FET biosensors, to streptavidin molecules in a pure solution and a serum solution: (a) p-type and (b) n-type branches of the *t*-dependent I_{DS}-V_G characteristic curves measured from the sensor (Sensor #1) in a pure solution of 30 fM streptavidin; (c) p-type and (d) n-type branches of the *t*-dependent I_{DS}- V_G characteristic curves measured from the sensor (Sensor #2) in a serum solution containing 30 fM streptavidin.

to other materials, which is expected to make the flushing of non-specifically adsorbed molecules on TMDC FET channels much easier than that on the FET channels made from conventional semiconductors [164].

5.3.5 Sensor Response Signals Measured at Different Streptavidin Concentrations

We further used MoS_2 and WSe_2 FET sensors operated by the IFDM cycle-wise method to obtain standard curves for streptavidin quantification (*i.e.*, calibrated sensor response (*R*) versus analyte concentration (*n*) curves) and to enable rapid biomolecule quantification at femtomolar levels. Specifically, we fabricated a set of MoS_2 sensors and a set of WSe_2 sensors in the same fabrication batch. These sensors were used to quantify 30 fM, 300 fM, and 3 pM solutions of pure streptavidin. Figures 5.8 and 5.9 display the *t*-dependent I_{DS}-V_G characteristic curves of these MoS_2 and WSe_2 sensors, respectively, which were measured at different streptavidin concentrations ($n_{streptavidin}$ = 30 fM, 300 fM, and 3 pM). Figures 5.10 (a) and (b) show the *S*-*t* response curves captured from the n-type branches of the I_{DS}-V_G curves of MoS_2 FET sensors (captured at V_G = 100 V) and the p-type branches of the I_{DS}-V_G curves of WSe_2 FET sensors (captured at V_G = -100 V), respectively. These *S*-*t* response curves were measured at $n_{streptavidin}$ = 30 fM, 300 fM, and 3 pM. For both MoS_2 and WSe_2 sensors, the initial slopes of their *S*-*t* response curves exhibit a dependence on streptavidin concentrations ($n_{streptavidin}$) and can be exploited for rapid streptavidin quantification. The determination of such initial slopes of *S*-*t* curves does not need a long accumulative incubation time until the analyte-receptor binding reaction reaches to the equilibrium state. Therefore, the initial slope of an *S*-*t* curve (*i.e.*, *dS/dt* at *t* ~ 0) can serve as a derived sensor response quantity for enabling rapid biomolecule quantification. Here, the specific *dS/dt* value is extracted from the *S*-*t* response curve through linearly fitting the S data measured within the first three IFDM cycles (typically, the accumulative incubation time is shorter than 20 min for $n_{streptavidin}$ ~ 30 fM, and the total assay time is less than 23 min). Figures 5.10 (c) and (d) plots the *dS/dt* - $n_{streptavidin}$ curves extracted from the *S*-*t* response curves measured from MoS_2 and WSe_2 sensors, respectively. Such *dS/dt* - $n_{streptavidin}$ curves can serve as standard curves for rapid streptavidin quantification. To evaluate the repeatability of such streptavidin quantification using the initial varying slopes of *S*-*t* response curves, another set of two MoS_2 FET sensors fabricated in the same batch were used to generate additional two *S*-*t* response curves at $n_{streptavidin}$ = 3 pM, which were plotted in Figure 5.10 (a). All three *S*-*t* response curves measured at $n_{streptavidin}$ = 3 pM appear to have very similar initial slopes, which can be well correlated to $n_{streptavidin}$ = 3 pM. Additionally, another WSe_2 sensor was

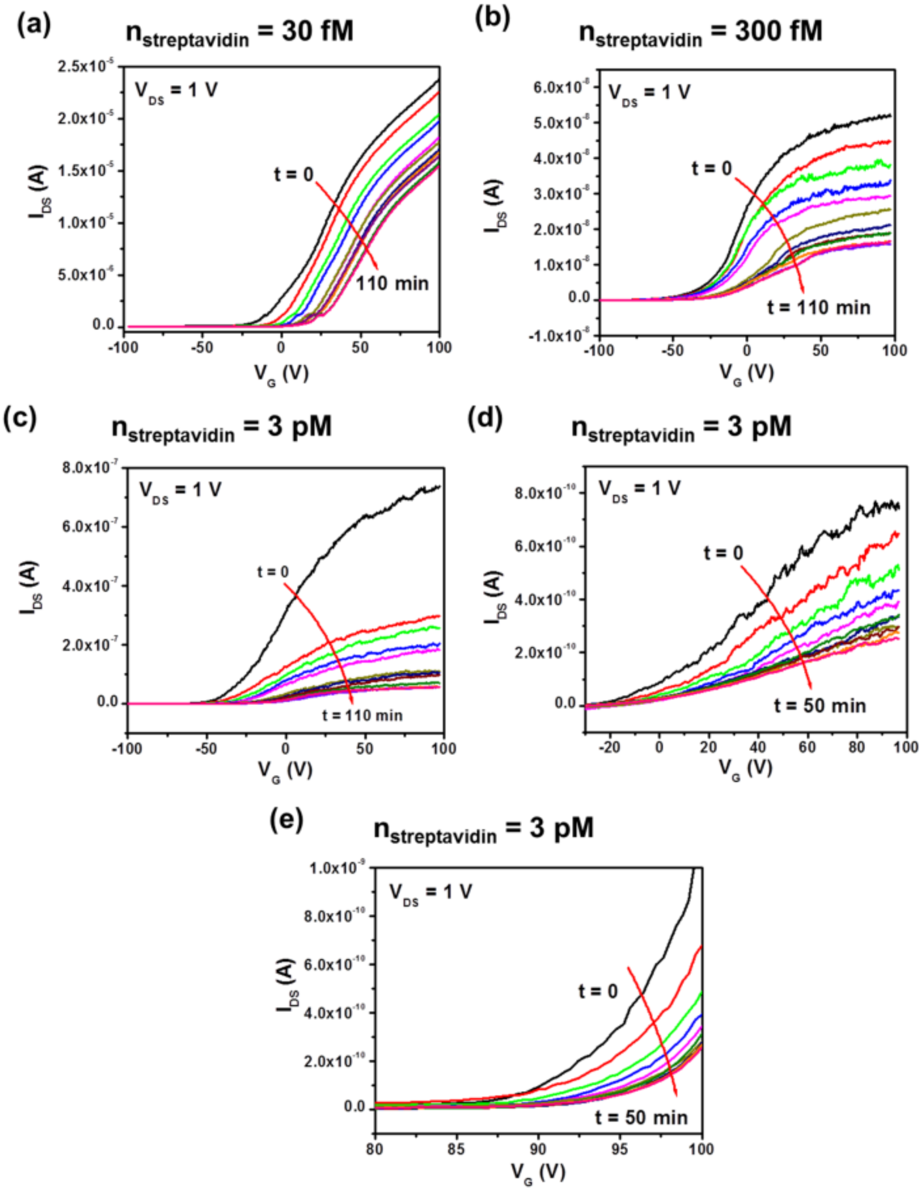

Figure 5.8 *t*-dependent I_{DS}-V_G characteristic curves of a set of MoS_2 FET sensors, which were measured at different streptavidin concentrations ($n_{streptavidin}$ = 30 fM, 300 fM, and 3 pM).

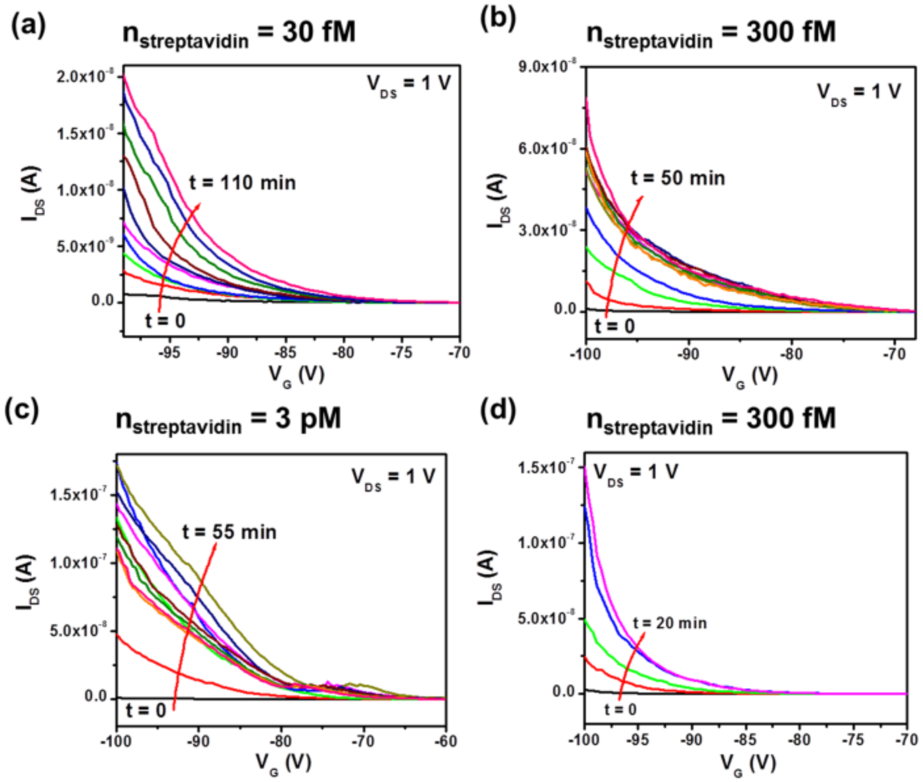

Figure 5.9 p-type branches of the t-dependent I_{DS}-V_G characteristic curves of a set of WSe$_2$ FET sensors, which were measured at different streptavidin concentrations ($n_{streptavidin}$ = 30 fM, 300 fM, and 3 pM).

used to generate an additional *S*-*t* response curve at $n_{streptavidin}$ ~ 300 fM, which is also consistent with the one already plotted in Figure 5.10 (b).

In addition, we also used our MoS$_2$ FET sensors and the IFDM cycle-wise method for testing the quantification of other clinical biomarkers, which usually exhibit a much weaker affinity to their antibody receptors in comparison with streptavidin. Here, we demonstrated Interleukin 1beta (IL1β) quantification. IL1β is a cytokine protein and serves as an important mediator of the inflammatory response. It is related to many cellular activities, including cell proliferation, differentiation, and apoptosis [165]. IL1β has a relatively weak affinity to its antibody in comparison with streptavidin (*i.e.*, $K_{D, Streptavidin}$ ~ 10^{-14} M (or 10 fM), and $K_{D, IL1\beta}$ ~ 10^{-9} M (or 1 nM)). Therefore, the state-of-the-art biodetection methods usually result in LODs in the range of 10s pM to 1 nM for IL1β quantification, and fM-level IL1β quantification is still a challenge.

Figure 5.11 displays the *t*-dependent I_{DS}-V_G characteristic curves measured from a set of six MoS_2 FET sensors, which were subjected to a set of pure IL1β solutions with different IL1β concentrations (*i.e.*, $n_{IL1\beta}$ = 0 fM, 1 fM, 4 fM, 20 fM, 100 fM, and 500 fM), respectively. From these I_{DS}-V_G curves, the corresponding *S*-*t* response curves were extracted at V_G = 100 V and plotted in Fig. 5.12 (a). It should be noted that for $n_{IL1\beta}$ = 0, the *S*-*t* response curve is not completely flat. This indicates that the pure buffer solution results in moderate nonspecific absorption of ions or molecules on the MoS_2 channel. Currently, we have not fully understood the mechanism of such nonspecific absorption, but temporarily attributed it to the slow reaction between the crystal defects on the MoS_2 channel and the buffered solution. Such a zero-concentration *S*-*t* response curve serves as the baseline for IL1β quantification. Figure 5.12 (a) shows that the *S*-*t* response curve measured at $n_{IL1\beta}$ = 1 fM is significantly distinct from that measured at $n_{IL1\beta}$ = 0. This indicates that our MoS_2 FET biosensors in combination with the IFDM cycle-wise method can result in a LOD of ~1 fM for IL1β quantification. As discussed for streptavidin quantification, the initial slopes of the *S*-*t* response curves shown in Fig. 5.12 (a) can be also used as response signals for the rapid IL1β quantification. Figure 5.12 (b) shows the extracted *dS/dt* data plotted as a function of the IL1β concentrations ($n_{IL1\beta}$). In our work, to unambiguously determine the *dS/dt* values for IL1β quantification, the minimum incubation time is about 20 min, and the corresponding total assay time is about 23 min. Therefore, this work has demonstrated that the TMDC FET biosensors operated using the IFDM cycle-wise method can enable rapid fM-level quantification of IL1β and other biomolecules with relatively weak affinity (*i.e.*, nM-level K_D values) to their antibody receptors.

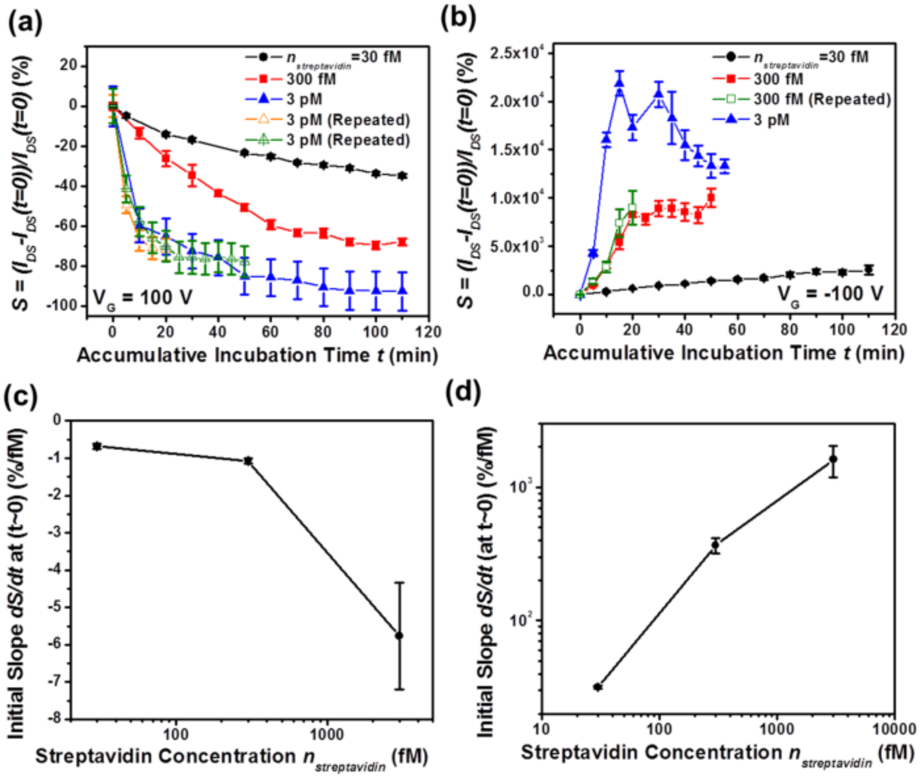

Figure 5.10 *S-t* response curves measured at different streptavidin concentrations ($n_{streptavidin}$ = 30 fM, 300 fM, and 3 pM), which are captured from (a) the n-type branches of the *t*-dependent I_{DS}-V_G curves of a set of MoS_2 sensors and (b) the p-type branches of the I_{DS}-V_G curves of a set of WSe_2 sensors; (c) and (d) plots the *dS/dt* - $n_{streptavidin}$ curves extracted from the *S-t* response curves measured from MoS_2 and WSe_2 sensors, respectively.

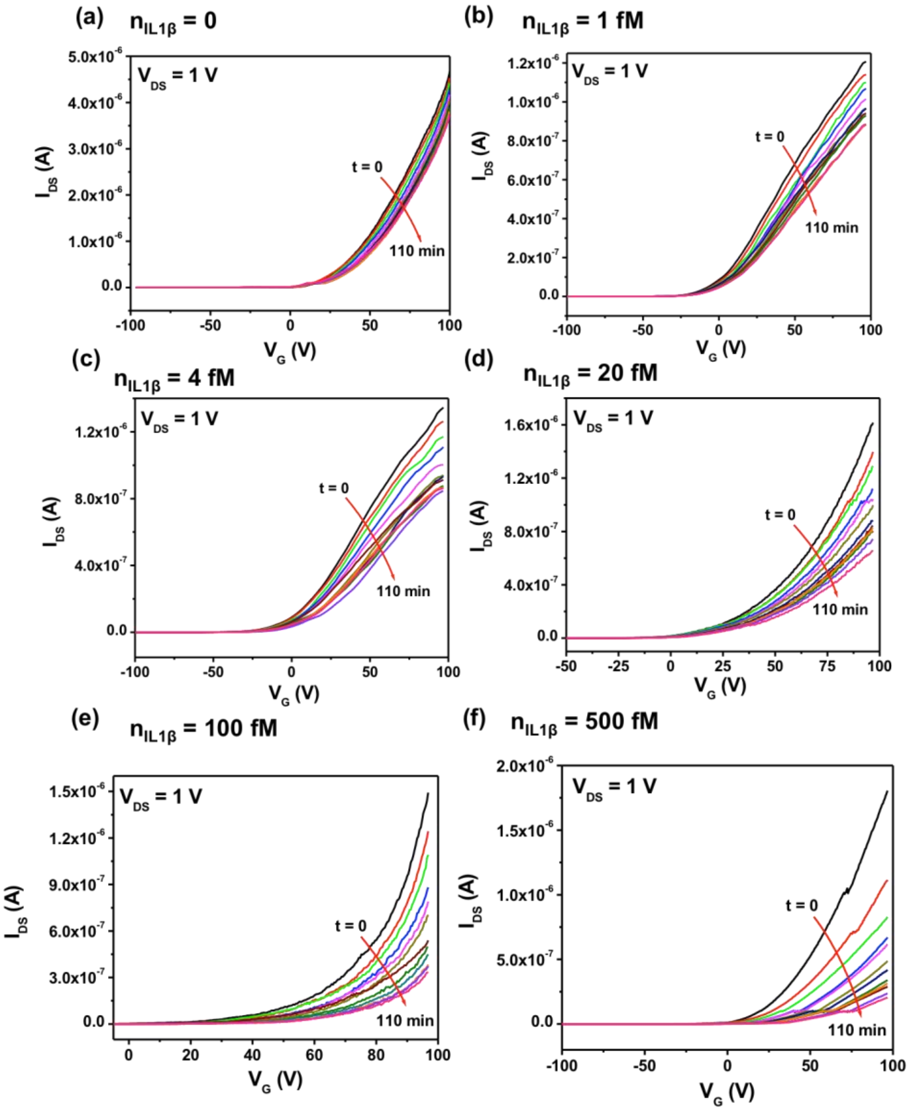

Figure 5.11 *t*-dependent I_{DS}-V_G characteristic curves of a set of MoS_2 FET sensors, which were measured at different IL1β concentrations ($n_{IL1\beta}$ = 0 fM, 1 fM, 4 fM, 20 fM, 100 fM, and 500 fM).

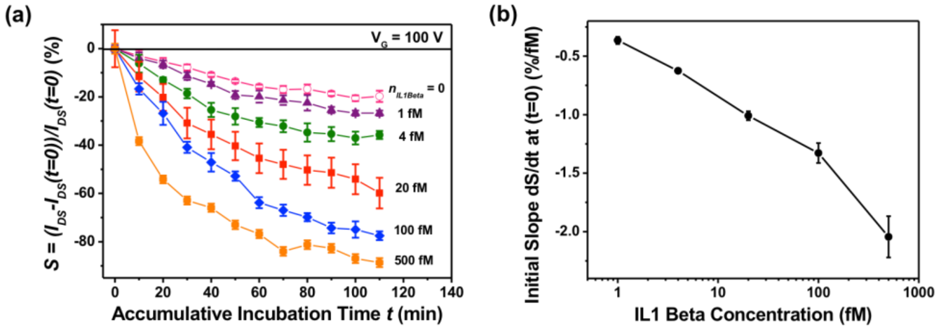

Figure 5.12 (a) *S-t* response curves measured at different IL1β concentrations ($n_{IL1\beta}$ = 0 fM, 1 fM, 4 fM, 20 fM, 100 fM, and 500 fM), which are captured from the *t*-dependent I_{DS}-V_G curves of a set of MoS_2 sensors at V_G = 100 V, V_{DS} = 1 V; (b) plots the *dS/dt* - $n_{IL1\beta}$ curve extracted from the *S-t* response curves shown in (a).

5.4 Summary

In summary, we established a cycle-wise approach for operating MoS_2 and WSe_2 FET biosensors. This approach enabled rapid, low-noise, highly specific biomolecule quantification and analyte-receptor binding kinetics analysis. The cycle-wise detection process utilized a microfluidic structure integrated with a MoS_2 or WSe_2 FET sensor that delivers a time-sequenced series of reagent fluids to the sensing FET channel. Periodically delivering the reagent fluids into the device resulted in assay cycles, each with four stages: incubation, flushing, drying, and measurement (*i.e.*, IFDM cycles). This process can measure time-dependent sensor responses to analyte-receptor binding reaction. The IFDM cycle-wise approach can physically separate incubation, flushing, and electrical measurement steps from each other in the time sequence. Thus, it can prevent liquid-solution-induced electrochemical damage, electronic noise, signal screening, and nonspecific adsorption, therefore improving the sensors' durability, detection limit, sensitivity, and specificity. Combined with the high sensitivity and low detection limit of MoS_2/WSe_2-based FET biosensors, this cycle-wise detection method can realize rapid biomolecule quantification at femtomolar levels. In this work, we have demonstrated the quantification of femtomolar-level streptavidin and IL1β suspended in pure and complex solutions (*e.g.*, serum) with a detection limit of ~1 fM and a total incubation time less than 20 min (or total assay time less than 23 min). This work leverages the superior electronic properties of emerging layered semiconductors for label-free biosensing applications and also advances the sensor operation technology toward realizing fast real-time biomolecule quantification at femtomolar levels. In addition, the presented cycle-wise method could be generally applied to other nanoelectronics-based biological and chemical sensors while overcoming the issues resulting from poor compatibility between reagents and electrical detection processes in a fluidic environment.

Chapter 6

Conclusions and Future Work

6.1 Summary of Thesis

This thesis work successfully advanced nanofabrication technologies and device physics for biosensing applications based on atomically layered materials. In our first study, we developed the plasma-assisted nanoprinting approach for producing ordered and pristine few-layer-MoS_2 flake pixels over large areas. This work lays an important foundation for future scale-up nanoelectronic applications of few-layer-MoS_2 micro- and nanostructures. In our second study, we fabricated MoS_2 transistor sensors with insulating layers, which can be used for quantifying femtomolar-level biomolecules and molecule interactions. This work advanced the critical device physics for leveraging the excellent electronic/structural properties of TMDCs in biosensing applications as well as the research capability in analyzing the biomolecule interactions with fM-level sensitivities. In our third study, we compared between insulating-layer-coated and insulating-layer-free MoS_2 transistor biosensors in their sensor response behaviors. This work advances the device physics for simplifying the transistor biosensor structures targeting for femtomolar-level quantification of biomolecules. In our fourth study, we developed cycle-wise operation of MoS_2 and WSe_2 transistor biosensors for enabling rapid biomolecule quantification at femtomolar levels. This work leverages the superior electronic properties of emerging layered semiconductors for biosensing applications and advances the biosensing techniques toward realizing fast real-time immunoassay for low-abundance biomolecule detection.

6.2 Future Research

Our TMDC FET sensors, especially those fabricated in different fabrication batches, still exhibit observable device-to-device variation in sensor response signals. It is anticipated that such variation could be further minimized by using calibrated response quantities that are completely independent of the FET performance parameters. We currently lack such a calibration approach, however, because we have not established a complete device physics model that can be used for quantitatively analyzing the responses of TMDC FET biosensors to specific analyte-receptor binding reaction events. In our previous work, we qualitatively identified that the electrical responses measured from a few-layer-TMDC FET biosensor are attributed to the net effect of (i) analyte-molecule-introduced doping to the TMDC channel and (ii) surface scattering due to binding-reaction-induced disordered potentials. Future work will seek to quantitatively calculate the contributions of these two mechanisms to the final sensor response signals and establish a calibration method based on such calculation to further improve the sensor-to-sensor consistency in calibrated sensor readings. Furthermore, such a quantitative device physics model is also needed for extracting critical molecular interaction properties, such as the affinity constant (K_D), and association/dissociation rates (k_{on}/k_{off}) of analyte-receptor pairs, from electrical sensor responses. Another approach to explore device-to-device variation in sensor response signals is to study crystal structures of TMDC materials. Unlike silicon-based FET, TMDC FETs have polycrystalline structures. Therefore, the aspects of crystal domain boundaries on TMDC channel surfaces are different in each sensor, which induce the device-to-device variation in sensor response signals. Since we expect the receptors are functionalized on the domain boundaries, another future study will pursue the fabrication of our TMDC FET sensors with different channel lengths, which may affect the total number of binding sites on the sensing channels, resulting in a change of sensor response signals. Based on the aforementioned research, we can contribute to the development of a multiplexed cytokine detection platform with high throughput field-effect transistor biosensors.

APPENDICES

Appendix A

Finite Element Analysis for Simulating Electric Field around the Edge ribbon of a MoS_2 Pixel and Calculating Effective Gate Capacitance of Edge-Based FETs (C_g)

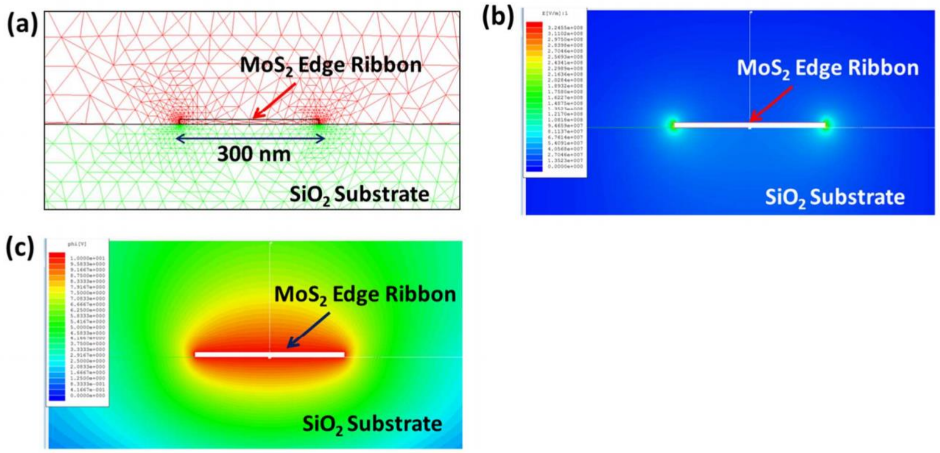

Figure A1 (a) Simulation model based on finite element analysis (FEA) for calculating the effective gate capacitance of the edge ribbon of a MoS_2 pixel, which takes into account the fringe effect at the feature edges. (b) Cross-sectional viewgraph of simulated electric field around the MoS_2 edge ribbon. (c) Cross-sectional viewgraph of simulated equipotential lines of 6 electric field around the MoS_2 ribbon.

Figure A1 shows the simulation of electric field around the edge ribbon of a MoS_2 pixel (cross-sectional view). The simulation was performed by using a finite element analysis (FEA) software tool (MAXWELL SV from Ansoft, Inc.). The simulation can give out the effective gate capacitance associated with a single MoS_2 ribbon per unit channel length (C_g) [unit: F/m].

In the simulation, the dielectric constant of SiO_2 is ε_r ~ 3.9; the thickness of the gate dielectric is d ~ 330 nm; the width and thickness of the MoS_2 edge ribbon are 300 nm and 10 nm, respectively. The average gate capacitance associated with a 300 nm wide, 10 nm thick MoS_2 ribbon per unit channel length is calculated to be 187.9 pF/m.

Appendix B

The Dual-Gate Thin-Film Transistor Biosensor Model

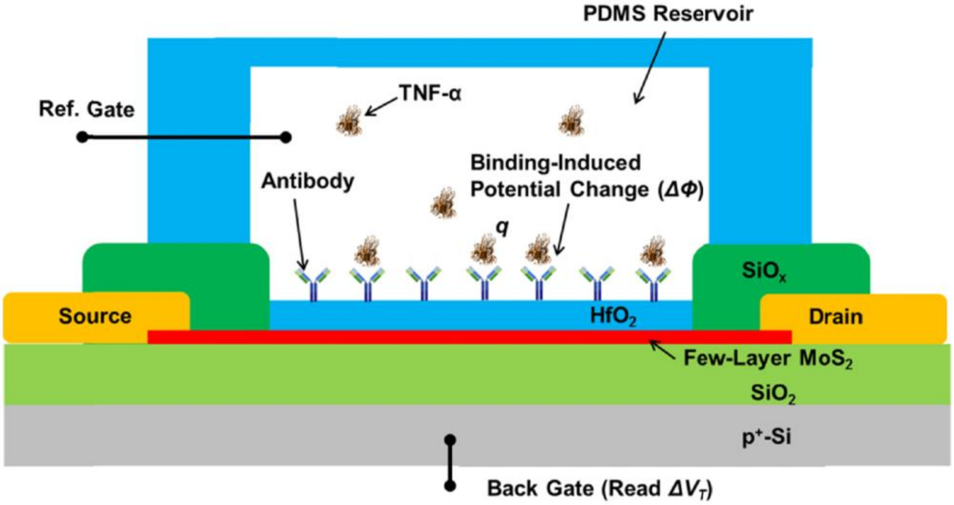

Figure B1 A schematic illustration of the dual-gate thin-film transistor biosensor model

Figure B1 shows the dual-gate thin-film transistor biosensor model. The binding of TNF-α molecules with the antibody receptors functionalized on the HfO_2 effective layer can cause a potential change ($\Delta\Phi$) on this effective layer. $\Delta\Phi$ can be evaluated using $\Delta\Phi = qN_{TNF}/C_{HfO2}$, where q is the effective charge brought to the HfO_2 effective layer through a single antibody-(TNF-α) binding event (here, q is the effective charge sensed by the transistor, and the screening effect due to the electrical double layer in solvent has been involved into q); N_{TNF} is the total number of TNF-α molecules bound to the HfO_2 effective layer; C_{HfO2} is the total capacitance of the HfO_2 effective layer. This $\Delta\Phi$ induces a change in the conductive charge ($\Delta\Phi = C_{HfO2}\Delta\Phi)$ in the MoS_2 channel. This $\Delta\Phi$ can cause a shift of the threshold voltage ($\Delta V_T)$ measured from the back gate (note: not measured from the top gate), and ΔV_T can be evaluated by $\Delta V_T = \Delta Q/C_{SiO2} = (C_{HfO2}/C_{SiO2})\Delta\Phi = qN_{TNF}/C_{SiO2}$, where C_{SiO2} is the capacitance of the back-gate dielectric layer. Furthermore, N_{TNF} can be calculated using $N_{TNF} = \sigma_{TNF}A$, where σ_{TNF} is the areal density of bound TNF-α molecules on the effective layer and A is the total sensor area. C_{SiO2} can be calculated using $C_{SiO2} = k_{SiO2}\varepsilon_0 A/d_{SiO2}$ and k_{SiO2} are the thickness and dielectric constant of the SiO_2 back-gate dielectric layer, respectively; ε_0 is the vacuum permittivity. Therefore, $\Delta V_T = qN_{TNF}/C_{SiO2} = qd_{SiO2}\sigma_{TNF}/k_{SiO2}\varepsilon_0.$

Bibliography

[1] K. S. Novoselov, A. K. Geim, S. V. Morozov, D. Jiang, Y. Zhang, S. V. Dubonos, et al., "Electric Field Effect in Atomically Thin Carbon Films," *Science*, vol. 306, pp. 666-669, 2004.

[2] P. Miro, M. Audiffred, and T. Heine, "An Atlas of Two-Dimensional Materials," *Chemical Society Reviews*, vol. 43, pp. 6537-6554, 2014.

[3] C. Lee, X. Wei, J. W. Kysar, and J. Hone, "Measurement of the Elastic Properties and Intrinsic Strength of Monolayer Graphene," *Science*, vol. 321, pp. 385-388, 2008.

[4] A. A. Balandin, S. Ghosh, W. Bao, I. Calizo, D. Teweldebrhan, F. Miao, and C. N. Lau, "Superior Thermal Conductivity of Single-Layer Graphene," *Nano Letters*, vol. 8, pp. 902-907, 2008.

[5] A. K. Geim and K. S. Novoselov, "The Rise of Graphene," *Nature Materials*, vol. 6, pp. 183-191, 2007.

[6] K. S. Novoselov, V. I. Fal'ko, L. Colombo, P. R. Gellert, M. G. Schwab, and K. Kim, "A Roadmap for Graphene," *Nature*, vol. 490, pp. 192-200, 2012.

[7] F. Xia, T. Mueller, Y.-m. Lin, A. Valdes-Garcia, and P. Avouris, "Ultrafast Graphene Photodetector," *Nature Nanotechnology*, vol. 4, pp. 839-843, 2009.

[8] Z. Liu, J. T. Robinson, X. Sun, and H. Dai, "PEGylated Nanographene Oxide for Delivery of Water-Insoluble Cancer Drugs," *Journal of the American Chemical Society*, vol. 130, pp. 10876-10877, 2008.

[9] K. Yang, L. Feng, X. Shi, and Z. Liu, "Nano-Graphene in Biomedicine: Theranostic Applications," *Chemical Society Reviews*, vol. 42, pp. 530-547, 2013.

[10] F. Schedin, A. K. Geim, S. V. Morozov, E. W. Hill, P. Blake, M. I. Katsnelson, K. S. Novoselov, "Detection of individual gas molecules adsorbed on graphene," *Nature Materials*, vol. 6, pp. 652-655, 2007.

[11] J. D. Fowler, M. J. Allen, V. C. Tung, Y. Yang, R. B. Kaner, and B. H. Weiller, "Practical Chemical Sensors from Chemically Derived Graphene," *ACS Nano*, vol. 3, pp. 301-306, 2009.

[12] F. Yavari and N. Koratkar, "Graphene-Based Chemical Sensors," *Journal of Physical Chemistry Letters*, vol. 3, pp. 1746-1753, 2012.

[13] S. He, B. Song, D. Li, C. Zhu, W. Qi, Y. Wen, L. Wang, S. Song, H. Fang, and C. Fan, "A Graphene Nanoprobe for Rapid, Sensitive, and Multicolor Fluorescent DNA Analysis," *Advanced Functional Materials*, vol. 20, pp. 453-459, 2010.

[14] C.-H. Lu, H.-H. Yang, C.-L. Zhu, X. Chen, and G.-N. Chen, "A Graphene Platform for Sensing Biomolecules," *Angewandte Chemie-International Edition*, vol. 48, pp. 4785-4787, 2009.

[15] Q. He, S. Wu, S. Gao, X. Cao, Z. Yin, H. Li, P. Chen, and H. Zhang, "Transparent, Flexible, All-Reduced Graphene Oxide Thin Film Transistors," *ACS Nano*, vol. 5, pp. 5038-5044, 2011.

[16] S. Wu, Q. He, C. Tan, Y. Wang, and H. Zhang, "Graphene-Based Electrochemical Sensors," *Small*, vol. 9, pp. 1160-1172, 2013.

[17] R. F. Frindt, "Single Crystals of MoS_2 Several Molecular Layers Thick," *Journal of Applied Physics*, vol. 37, pp. 1928, 1966.

[18] H. Peng, K. Lai, D. Kong, S. Meister, Y. Chen, X.-L. Qi, S.-C. Zhang, Z.-X. Shen, and Y. Cui, "Aharonov-Bohm Interference in Topological Insulator Nanoribbons," *Nature Materials*, vol. 9, pp. 225-229, 2010.

[19] L. Song, L. Ci, H. Lu, P. B. Sorokin, C. Jin, J. Ni, A. G. Kvashnin, D. G. Kvashnin, J. Lou, B. I. Yakobson, and P. M. Ajayan, "Large Scale Growth and Characterization of Atomic Hexagonal Boron Nitride Layers," *Nano Letters*, vol. 10, pp. 3209-3215, 2010.

[20] M. Osada and T. Sasaki, "Exfoliated Oxide Nanosheets: New Solution to Nanoelectronics," *Journal of Materials Chemistry*, vol. 19, pp. 2503-2511, 2009.

[21] H. Zhang, "Ultrathin Two-Dimensional Nanomaterials," *ACS Nano*, vol. 9, pp. 9451-9469, 2015.

[22] J. C. Meyer, A. K. Geim, M. I. Katsnelson, K. S. Novoselov, T. J. Booth, and S. Roth, "The Structure of Suspended Graphene Sheets," *Nature*, vol. 446, pp. 60-63, 2007.

[23] T. Shao, B. Wen, R. Melnik, S. Yao, Y. Kawazoe, and Y. Tian, "Temperature Dependent Elastic Constants and Ultimate Strength of Graphene and Graphyne," *Journal of Chemical Physics*, vol. 137, 2012.

[24] Y. Zhu, S. Murali, W. Cai, X. Li, J. W. Suk, J. R. Potts, and R.S. Ruoff, "Graphene and Graphene Oxide: Synthesis, Properties, and Applications," *Advanced Materials*, vol. 22, pp. 5226-5226, 2010.

[25] B. Radisavljevic, A. Radenovic, J. Brivio, V. Giacometti, and A. Kis, "Single-Layer MoS_2 Transistors," *Nature Nanotechnology*, vol. 6, pp. 147-150, 2011.

[26] S. Bertolazzi, J. Brivio, and A. Kis, "Stretching and Breaking of Ultrathin MoS_2," *ACS Nano*, vol. 5, pp. 9703-9709, 2011.

[27] Y. Zhu and F. Guo, "Preparation and Characterization of an Unsupported Nano-MoS_2 Catalyst," *Asian Journal of Chemistry*, vol. 25, pp. 8057-8060, 2013.

[28] J. Pu, Y. Yomogida, K.-K. Liu, L.-J. Li, Y. Iwasa, and T. Takenobu, "Highly Flexible MoS_2 Thin-Film Transistors with Ion Gel Dielectrics," *Nano Letters*, vol. 12, pp. 4013-4017, 2012.

[29] M.-L. Tsai, S.-H. Su, J.-K. Chang, D.-S. Tsai, C.-H. Chen, C.-I. Wu, L.-J. Li, L.-J. Chen, and J.-H. He, "Monolayer MoS_2 Heterojunction Solar Cells," *ACS Nano*, vol. 8, pp. 8317-8322, 2014.

[30] S. Wu, Z. Zeng, Q. He, Z. Wang, S. J. Wang, Y. Du, Z. Yin, X. Sun, W. Chen, and H. Zhang, "Electrochemically Reduced Single-Layer MoS_2 Nanosheets: Characterization, Properties, and Sensing Applications," *Small*, vol. 8, pp. 2264-2270, 2012.

[31] C. Zhu, Z. Zeng, H. Li, F. Li, C. Fan, and H. Zhang, "Single-Layer MoS_2-Based Nanoprobes for Homogeneous Detection of Biomolecules," *Journal of the American Chemical Society*, vol. 135, pp. 5998-6001, 2013.

[32] Y. Zhang, B. Zheng, C. Zhu, X. Zhang, C. Tan, H. Li, B. Chen, J. Yang, J. Chen, Y. Huang, L. Wang, and Hua Zhang, "Single-Layer Transition Metal Dichalcogenide Nanosheet-Based Nanosensors for Rapid, Sensitive, and Multiplexed Detection of DNA," *Advanced Materials*, vol. 27, pp. 935-939, 2015.

[33] H. Li, Z. Yin, Q. He, H. Li, X. Huang, G. Lu, D. W. H. Fam, A. L. Y. Tok, Q. Zhang, and H. Zhang, "Fabrication of Single- and Multilayer MoS_2 Film-Based Field-Effect Transistors for Sensing NO at Room Temperature," *Small*, vol. 8, pp. 63-67, 2012.

[34] W. Zhou, Z. Yin, Y. Du, X. Huang, Z. Zeng, Z. Fan, H. Liu, J. Wang, and H. Zhang, "Synthesis of Few-Layer MoS_2 Nanosheet-Coated TiO_2 Nanobelt Heterostructures for Enhanced Photocatalytic Activities," *Small*, vol. 9, pp. 140-147, 2013.

[35] J. Kibsgaard, Z. Chen, B. N. Reinecke, and T. F. Jaramillo, "Engineering the Surface Structure of MoS_2 to Preferentially Expose Active Edge Sites for Electrocatalysis," *Nature Materials*, vol. 11, pp. 963-969, 2012.

[36] L. Cao, S. Yang, W. Gao, Z. Liu, Y. Gong, L. Ma, G. Shi, S. Lei, Y. Zhang, S. Zhang, R. Vajtai, and P. M. Ajayan, "Direct Laser-Patterned Micro-Supercapacitors from Paintable MoS_2 Films," *Small*, vol. 9, pp. 2905-2910, 2013.

[37] J. A. Wilson and A. D. Yoffe, "Transition Metal Dichalcogenides Discussion And Interpretation of Observed Optical, Electrical and Structural Properties," *Advances in Physics*, vol. 18, pp. 193, 1969.

[38] L. F. Mattheis, "Band Structures of Transition-Metal-Dichalcogenide Layer Compounds," *Physical Review B*, vol. 8, pp. 3719-3740, 1973.

[39] N. V. Podberezskaya, S. A. Magarill, N. V. Pervukhina, and S. V. Borisov, "Crystal Chemistry of Dichalcogenides MX_2," *Journal of Structural Chemistry*, vol. 42, pp. 654-681, 2001.

[40] Q. H. Wang, K. Kalantar-Zadeh, A. Kis, J. N. Coleman, and M. S. Strano, "Electronics and Optoelectronics of Two-Dimensional Transition Metal Dichalcogenides," *Nature Nanotechnology*, vol. 7, pp. 699-712, 2012.

[41] R. Lv, J. A. Robinson, R. E. Schaak, D. Sun, Y. Sun, T. E. Mallouk, and M. Terrones, "Transition Metal Dichalcogenides and Beyond: Synthesis, Properties, and Applications of Single- and Few-Layer Nanosheets," *Accounts of Chemical Research*, vol. 48, pp. 56-64, 2015.

[42] L. Wang, Y. Wang, J. I. Wong, T. Palacios, J. Kong, and H. Y. Yang, "Functionalized MoS_2 Nanosheet-Based Field-Effect Biosensor for Label-Free Sensitive Detection of Cancer Marker Proteins in Solution," *Small*, vol. 10, pp. 1101-1105, 2014.

[43] D. Sarkar, W. Liu, X. Xie, A. C. Anselmo, S. Mitragotri, and K. Banerjee, "MoS_2 Field-Effect Transistor for Next-Generation Label-Free Biosensors," *ACS Nano*, vol. 8, pp. 3992-4003, 2014.

[44] J. Z. Ou, A. F. Chrimes, Y. Wang, S.-Y. Tang, M. S. Strano, and K. Kalantar-zadeh, "Ion-Driven Photoluminescence Modulation of Quasi-Two-Dimensional MoS_2 Nanoflakes for Applications in Biological Systems," *Nano Letters*, vol. 14, pp. 857-863, 2014.

[45] H. D. Ha, D. J. Han, J. S. Choi, M. Park, and T. S. Seo, "Dual Role of Blue Luminescent MoS_2 Quantum Dots in Fluorescence Resonance Energy Transfer Phenomenon," *Small*, vol. 10, pp. 3858-3862, 2014.

[46] J. H. Appel, D. O. Li, J. D. Podlevsky, A. Debnath, A. A. Green, Q. H. Wang, and J. Chae, "Low Cytotoxicity and Genotoxicity of Two-Dimensional MoS_2 and WS_2," *ACS Biomaterials-Science & Engineering*, vol. 2, pp. 361-367, 2016.

[47] M. F. Neurath, "Cytokines in Inflammatory Bowel Disease," *Nature Reviews Immunology*, vol. 14, pp. 329-342, 2014.

[48] B.-R. Oh, N.-T. Huang, W. Chen, J. H. Seo, P. Chen, T. T. Cornell, T. P. Shanley, J. Fu, and K. Kurabayashi, "Integrated Nanoplasmonic Sensing for Cellular Functional Immunoanalysis Using Human Blood," *ACS Nano*, vol. 8, pp. 2667-2676, 2014.

[49] H. Nam, B.-R. Oh, P. Chen, M. Chen, S. Wi, W. Wan, K. Kurabayashi, and X. Liang, "Multiple MoS_2 Transistors for Sensing Molecule Interaction Kinetics," *Scientific Reports*, vol. 5, 2015.

[50] Y. Cui, Q. Q. Wei, H. K. Park, and C. M. Lieber, "Nanowire Nanosensors for Highly Sensitive and Selective Detection of Biological and Chemical Species," *Science*, vol. 293, pp. 1289-1292, 2001.

[51] J. Wang, "Carbon-Nanotube Based Electrochemical Biosensors: A Review," *Electroanalysis*, vol. 17, pp. 7-14, 2005.

[52] L. S. Byskov, "Sulfur Bonding in MoS_2 and Co-Mo-S Structures," *Springer*, vol. 47, pp. 177, 1997.

[53] T. Korn, S. Heydrich, M. Hirmer, J. Schmutzler, and C. Schueller, "Low-Temperature Photocarrier Dynamics in Monolayer MoS_2," *Applied Physics Letters*, vol. 99, 2011.

[54] K. F. Mak, C. Lee, J. Hone, J. Shan, and T. F. Heinz, "Atomically Thin MoS_2: A New Direct-Gap Semiconductor," *Physical Review Letters*, vol. 105, 2010.

[55] H. Liu and P. D. Ye, "MoS_2 Dual-Gate MOSFET With Atomic-Layer-Deposited Al_2O_3 as Top-Gate Dielectric," *IEEE Electron Device Letters*, vol. 33, pp. 546-548, 2012.

[56] Z. Yin, H. Li, H. Li, L. Jiang, Y. Shi, Y. Sun, G. Lu, Q. Zhang, X. Chen, and H. Zhang, "Single-Layer MoS_2 Phototransistors," *ACS Nano*, vol. 6, pp. 74-80, 2012.

[57] Q. He, Z. Zeng, Z. Yin, H. Li, S. Wu, X. Huang, and H. Zhang, "Fabrication of Flexible MoS_2 Thin-Film Transistor Arrays for Practical Gas-Sensing Applications," *Small*, vol. 8, pp. 2994-2999, 2012.

[58] H. Wang, L. Yu, Y.-H. Lee, Y. Shi, A. Hsu, M. L. Chin, L.-J. Li, M. Dubey, J. Kong, and T. Palacios, "Integrated Circuits Based on Bilayer MoS_2 Transistors," *Nano Letters*, vol. 12, pp. 4674-4680, 2012.

[59] G. Eda, H. Yamaguchi, D. Voiry, T. Fujita, M. Chen, and M. Chhowalla, "Photoluminescence from Chemically Exfoliated MoS_2," *Nano Letters*, vol. 11, pp. 5111-5116, 2011.

[60] R. Fivaz and E. Mooser, "Mobility of Charge Carriers in Semiconducting Layer Structures," *Physical Review*, vol. 163, pp. 743, 1967.

[61] A. Ayari, E. Cobas, O. Ogundadegbe, and M. S. Fuhrer, "Realization and Electrical Characterization of Ultrathin Crystals of Layered Transition-Metal Dichalcogenides," *Journal of Applied Physics*, vol. 101, 2007.

[62] J. N. Coleman, M. Lotya, A. O'Neill, S. D. Bergin, P. J. King, U. Khan, K. Young, A. Gaucher, S. De, R. J. Smith, I. V. Shvets, S. K. Arora, G. Stanton, H.-Y. Kim, K. Lee, G. T. Kim, G. S. Duesberg, T. Hallam, J. J. Boland, J. J. Wang, J. F. Donegan, J. C. Grunlan, G. Moriaty, A. Shmeliov, R. J. Nicholls, J. M. Perkins, E. M. Grieveson, K. Theuwissen, D. W. McComb, P. D. Nellist, and V. Nicolosi, "Two-Dimensional Nanosheets Produced by Liquid Exfoliation of Layered Materials," *Science*, vol. 331, pp. 568-571, 2011.

[63] Y. Yao, Z. Lin, Z. Li, X. Song, K.-S. Moon, and C.-P. Wong, "Large-Scale Production of Two-Dimensional Nanosheets," *Journal of Materials Chemistry*, vol. 22, pp. 13494-13499, 2012.

[64] B. K. Miremadi and S. R. Morrison, "The Intercalation and Exfoliation of Tungsten Disulfide," *Journal of Applied Physics*, vol. 63, pp. 4970-4974, 1988.

[65] W. M. R. Divigalpitiya, R. F. Frindt, and S. R. Morrison, "Inclusion Systems of Organic-Molecules in Restacked Single-Layer Molybdenum-Disulfide," *Science*, vol. 246, pp. 369-371, 1989.

[66] G. M. Cai, J. K. Jian, X. L. Chen, M. Lei, and W. Y. Wang, "Regular Hexagonal MoS_2 Microflakes Grown from MoO_3 Precursor," *Applied Physics A-Materials Science & Processing*, vol. 89, pp. 783-788, 2007.

[67] M. Virsek, M. Krause, A. Kolitsch, A. Mrzel, I. Iskra, S. D. Skapin, and M. Remskar, "The Transformation Pathways of $Mo_6S_2I_8$ Nanowires into Morphology-Selective MoS_2 Nanostructures," *Journal of Physical Chemistry C*, vol. 114, pp. 6458-6463, 2010.

[68] K.-K. Liu, W. Zhang, Y.-H. Lee, Y.-C. Lin, M.-T. Chang, C.-Y. Su, C.-S. Chang, H. Li, Y. Shi, H. Zhang, C.-S. Lai, and L.-J. Li, "Growth of Large-Area and Highly Crystalline MoS_2 Thin Layers on Insulating Substrates," *Nano Letters*, vol. 12, pp. 1538-1544, 2012.

[69] Y.-H. Lee, X.-Q. Zhang, W. Zhang, M.-T. Chang, C.-T. Lin, K.-D. Chang, Y.-C. Yu, J. T.-W. Wang, C.-S. Chang, L.-J. Li, and T.-W. Lin, "Synthesis of Large-Area MoS_2 Atomic Layers with Chemical Vapor Deposition," *Advanced Materials*, vol. 24, pp. 2320-2325, 2012.

[70] Y. Zhan, Z. Liu, S. Najmaei, P. M. Ajayan, and J. Lou, "Large-Area Vapor-Phase Growth and Characterization of MoS_2 Atomic Layers on a SiO_2 Substrate," *Small*, vol. 8, pp. 966-971, 2012.

[71] Y. Shi, W. Zhou, A.-Y. Lu, W. Fang, Y.-H. Lee, A. L. Hsu, S. M. Kim, K. K. Kim, H. Y. Yang, L.-J. Li, J.-C. Idrobo, and J. Kong, "van der Waals Epitaxy of MoS_2 Layers Using Graphene As Growth Templates," *Nano Letters*, vol. 12, pp. 2784-2791, 2012.

[72] A. Castellanos-Gomez, M. Barkelid, A. M. Goossens, V. E. Calado, H. S. J. van der Zant, and G. A. Steele, "Laser-Thinning of MoS_2: On Demand Generation of a Single-Layer Semiconductor," *Nano Letters*, vol. 12, pp. 3187-3192, 2012.

[73] C. L. Stender, E. C. Greyson, Y. Babayan, and T. W. Odom, "Patterned MoS_2 Nanostructures over Centimeter-Square Areas," *Advanced Materials*, vol. 17, pp. 2837-2841, 2005.

[74] H. Liu, J. Gu, and P. D. Ye, "MoS_2 Nanoribbon Transistors: Transition From Depletion Mode to Enhancement Mode by Channel-Width Trimming," *IEEE Electron Device Letters*, vol. 33, pp. 1273-1275, 2012.

[75] G. Reimbold, "Effects of Plasma Induced Charges on Thin Oxide of CMOS Technologies," *Microelectronics Journal*, vol. 27, pp. 599-609, 1996.

[76] C. Wang, K. J. Morton, Z. Fu, W.-D. Li, and S. Y. Chou, "Printing of Sub-20 nm Wide Graphene Ribbon Arrays Using Nanoimprinted Graphite Stamps and Electrostatic Force Assisted Bonding," *Nanotechnology*, vol. 22, 2011.

[77] A. Picard and G. Turban, "Plasma-Etching of Refractory-Metals (W, Mo, Ta) and Silicon in SF_6 and SF_6-O_2 - An Analysis of the Reaction-Products," *Plasma Chemistry and Plasma Processing*, vol. 5, pp. 333-351, 1985.

[78] K. H. Baek, S. J. Yun, J. M. Park, Y. S. Yoon, K. S. Nam, K. H. Kwon, and C.-I. Kim, "The Role of Sulfur During Mo Etching Using SF_6 and Cl_2 Gas Chemistries," *Journal of Materials Science Letters*, vol. 17, pp. 1483-1486, 1998.

[79] A. K. Geim, "Graphene: Status and Prospects," *Science*, vol. 324, pp. 1530-1534, 2009.

[80] X. Liang, A. S. P. Chang, Y. Zhang, B. D. Harteneck, H. Choo, D. L. Olynick, and S. Cabrini, "Electrostatic Force Assisted Exfoliation of Prepatterned Few-Layer Graphenes into Device Sites," *Nano Letters*, vol. 9, pp. 467-472, 2009.

[81] X. Liang, Z. Fu, and S. Y. Chou, "Graphene Transistors Fabricated via Transfer-Printing in Device Active-Areas on Large Wafer," *Nano Letters*, vol. 7, pp. 3840-3844, 2007.

[82] Y. Kubota, K. Watanabe, O. Tsuda, and T. Taniguchi, "Deep Ultraviolet Light-Emitting Hexagonal Boron Nitride Synthesized at Atmospheric Pressure," *Science*, vol. 317, pp. 932-934, 2007.

[83] Y. Kobayashi, K. Kumakura, T. Akasaka, and T. Makimoto, "Layered Boron Nitride as a Release Layer for Mechanical Transfer of GaN-Based Devices," *Nature*, vol. 484, pp. 223-227, 2012.

[84] D. Hsieh, D. Qian, L. Wray, Y. Xia, Y. S. Hor, R. J. Cava, and M. Z. Hasan, "A Topological Dirac Insulator in a Quantum Spin Hall Phase," *Nature*, vol. 452, pp. 970-974, 2008.

[85] X. Liang, D. L. Olynick, S. Cabrini, and J. Bokor, "Single-Digit Nanofabrication Routes for Tailoring and Assembling Graphene into Functional Nanotructures and Devices," *Silicon Compatible Materials, Processes, and Technologies for Advanced Integrated Circuits and Emerging Applications*, vol. 35, pp. 55-65, 2011.

[86] W. Lu, H. Koerner, and R. Vaia, "Effect of Electric Field on Exfoliation of Nanoplates," *Applied Physics Letters*, vol. 89, 2006.

[87] X. J. Wang, X. B. Wang, and P. R. C. Gascoyne, "General Expressions for Dielectrophoretic Force and Electrorotational Torque Derived Using the Maxwell Stress Tensor Method," *Journal of Electrostatics*, vol. 39, pp. 277-295, 1997.

[88] S. Lee and W. Lu, "The Switching of Rotaxane-Based Motors," *Nanotechnology*, vol. 22, 2011.

[89] S. Lee and W. Lu, "Effect of Mechanical Load on the Shuttling Operation of Molecular Muscles," *Applied Physics Letters*, vol. 94, 2009.

[90] K. S. Novoselov, D. Jiang, F. Schedin, T. J. Booth, V. V. Khotkevich, S. V. Morozov, and A. K. Geim, "Two-Dimensional Atomic Crystals," *Proceedings of the National Academy of Sciences of the United States of America*, vol. 102, pp. 10451-10453, 2005.

[91] S. Kim, A. Konar, W.-S. Hwang, J. H. Lee, J. Lee, J. Yang, C. Jung, H. Kim, J.-B. Yoo, J.-Y. Choi, Y. W. Jin, S. Y. Lee, D. Jena, W. Choi, and K. Kim, "High-Mobility and Low-Power Thin-Film Transistors Based on Multilayer MoS_2 Crystals," *Nature Communications*, vol. 3, 2012.

[92] S. Das, H.-Y. Chen, A. V. Penumatcha, and J. Appenzeller, "High Performance Multilayer MoS_2 Transistors with Scandium Contacts," *Nano Letters*, vol. 13, pp. 100-105, 2013.

[93] W. Bao, X. Cai, D. Kim, K. Sridhara, and M. S. Fuhrer, "High Mobility Ambipolar MoS_2 Field-Effect Transistors: Substrate and Dielectric Effects," *Applied Physics Letters*, vol. 102, 2013.

[94] D. Jena and A. Konar, "Enhancement of Carrier Mobility in Semiconductor Nanostructures by Dielectric Engineering," *Physical Review Letters*, vol. 98, 2007.

[95] T. D. Ray, L. A. Lewis, S. Gulati, P. A. Rice, and S. Ram, "Characterization of Antibodies in Human Serum Against Serogroup B Neisseria Meningitidis that Block Complement-Dependent Bactericidal Activity," *Molecular Immunology*, vol. 47, pp. 2249-2249, 2010.

[96] A. L. Timko, C. H. Miller, F. B. Johnson, and V. Ross, "In Vitro Quantitative Chemical Analysis of Tattoo Pigments," *Archives of Dermatology*, vol. 137, pp. 143-147, 2001.

[97] B. P. Timko, T. Cohen-Karni, Q. Qing, B. Tian, and C. M. Lieber, "Design and Implementation of Functional Nanoelectronic Interfaces With Biomolecules, Cells, and Tissue Using Nanowire Device Arrays," *IEEE Transactions on Nanotechnology*, vol. 9, pp. 269-280, 2010.

[98] G. F. Zheng, F. Patolsky, Y. Cui, W. U. Wang, and C. M. Lieber, "Multiplexed Electrical Detection of Cancer Markers with Nanowire Sensor Arrays," *Nature Biotechnology*, vol. 23, pp. 1294-1301, 2005.

[99] M. R. Jacobs and C. E. Good, "Residual Bacterial Contamination of Apheresis Platelets Following Early Culture - Results of a Multi-Site Study of 18,449 Units Using the Verax Pan Genera Detection Assay," *Transfusion*, vol. 50, pp. 30A-30A, 2010.

[100] M. R. Jacobs, S. Bajaksouzian, R. Yomtovian, A. Han, A. P. Talbot, N. X. Krueger, and A. Levin, "Detection of Bacteria in Leukocyte-Reduced Whole Blood Derived Platelet Units Using the Immunetics BacTx Test," *Transfusion*, vol. 50, pp. 194A-194A, 2010.

[101] Y. K. Vashist, G. Uzungolu, A. Kutup, F. Gebauer, A. Koenig, L. Deutsch, O. Zehler, P. Busch, V. Kalinin, J. R. Izbicki, E. F. Yekebas, "Heme Oxygenase-1 Germ Line GTn Promoter Polymorphism is an Independent Prognosticator of Tumor Recurrence and Survival in Pancreatic Cancer," *Journal of Surgical Oncology*, vol. 104, pp. 305-311, 2011.

[102] Y. Huang, H. G. Sudibya, D. Fu, R. Xue, X. Dong, L.-J. Li, and P. Chen, "Label-Free Detection of ATP Release from Living Astrocytes with High Temporal Resolution Using Carbon Nanotube Network," *Biosensors & Bioelectronics*, vol. 24, pp. 2716-2720, 2009.

[103] H. G. Sudibya, J. Ma, X. Dong, S. Ng, L.-J. Li, X.-W. Liu, and P. Chen, "Interfacing Glycosylated Carbon-Nanotube-Network Devices with Living Cells to Detect Dynamic Secretion of Biomolecules," *Angewandte Chemie-International Edition*, vol. 48, pp. 2723-2726, 2009.

[104] X. Duan, Y. Li, N. K. Rajan, D. A. Routenberg, Y. Modis, and M. A. Reed, "Quantification of the Affinities and Kinetics of Protein Interactions Using Silicon Nanowire Biosensors," *Nature Nanotechnology*, vol. 7, pp. 401-407, 2012.

[105] K. Shoorideh and C. O. Chui, "On the Origin of Enhanced Sensitivity in Nanoscale FET-Based Biosensors," *Proceedings of the National Academy of Sciences of the United States of America*, vol. 111, pp. 5111-5116, 2014.

[106] E. Stern, J. F. Klemic, D. A. Routenberg, P. N. Wyrembak, D. B. Turner-Evans, A. D. Hamilton, D. A. LaVan, T. M. Fahmy, and M. A. Reed, "Label-free Immunodetection with CMOS-Compatible Semiconducting Nanowires," *Nature*, vol. 445, pp. 519-522, 2007.

[107] F.-S. Zhou and Q.-H. Wei, "Scaling Laws for NanoFET Sensors," *Nanotechnology*, vol. 19, 2008.

[108] M. Chhowalla, H. S. Shin, G. Eda, L.-J. Li, K. P. Loh, and H. Zhang, "The Chemistry of Two-Dimensional Layered Transition Metal Dichalcogenide Nanosheets," *Nature Chemistry*, vol. 5, pp. 263-275, 2013.

[109] M. Bernardi, M. Palummo, and J. C. Grossman, "Extraordinary Sunlight Absorption and One Nanometer Thick Photovoltaics Using Two-Dimensional Monolayer Materials," *Nano Letters*, vol. 13, pp. 3664-3670, 2013.

[110] L. Britnell, R. M. Ribeiro, A. Eckmann, R. Jalil, B. D. Belle, A. Mishchenko, Y.-J. Kim, R. V. Gorbachev, T. Georgiou, S. V. Morozov, A. N. Grigorenko, A. K. Geim, C. Casiraghi, A. H. C. Neto, and K. S. Novoselov, "Strong Light-Matter Interactions in Heterostructures of Atomically Thin Films," *Science*, vol. 340, pp. 1311-1314, 2013.

[111] H.-Y. Chang, S. Yang, J. Lee, L. Tao, W.-S. Hwang, D. Jena, N. Lu, and D. Akinwande, "High-Performance, Highly Bendable MoS_2 Transistors with High-K Dielectrics for Flexible Low-Power Systems," *ACS Nano*, vol. 7, pp. 5446-5452, 2013.

[112] C. N. R. Rao, K. Biswas, K. S. Subrahmanyam, and A. Govindaraj, "Graphene, the New Nanocarbon," *Journal of Materials Chemistry*, vol. 19, pp. 2457-2469, 2009.

[113] P. Avouris, "Graphene: Electronic and Photonic Properties and Devices," *Nano Letters*, vol. 10, pp. 4285-4294, 2010.

[114] W. Zhu, D. Neumayer, V. Perebeinos, and P. Avouris, "Silicon Nitride Gate Dielectrics and Band Gap Engineering in Graphene Layers," *Nano Letters*, vol. 10, pp. 3572-3576, 2010.

[115] Y. Q. Wu, Y. M. Lin, K. A. Jenkins, J. A. Ott, C. Dimitrakopoulos, D. B. Farmer, F. Xia, A. Grill, D. A. Antoniadis, and P. Avouris, "RF Performance of Short Channel Graphene Field-Effect Transistor," *2010 International Electron Devices Meeting - Technical Digest*, 2010.

[116] M. J. Allen, V. C. Tung, and R. B. Kaner, "Honeycomb Carbon: A Review of Graphene," *Chemical Reviews*, vol. 110, pp. 132-145, 2010.

[117] J. Alicea, Y. Oreg, G. Refael, F. von Oppen, and M. P. A. Fisher, "Non-Abelian Statistics and Topological Quantum Information Processing in 1D Wire Networks," *Nature Physics*, vol. 7, pp. 412-417, 2011.

[118] W. Al-Sawai, H. Lin, R. S. Markiewicz, L. A. Wray, Y. Xia, S.-Y. Xu, M. Z. Hasan, and A. Bansil, "Topological Electronic Structure in Half-Heusler Topological Insulators," *Physical Review B*, vol. 82, 2010.

[119] J. J. Cha and Y. Cui, "Topological Insulators: The Surface Surfaces," *Nature Nanotechnology*, vol. 7, pp. 85-86, 2012.

[120] C. L. Kane and E. J. Mele, "Z_2 Topological Order and the Quantum Spin Hall Effect," *Physical Review Letters*, vol. 95, 2005.

[121] K. Novoselov and A. Geim, "Graphene Detects Single Molecule of Toxic Gas," *Materials Technology*, vol. 22, pp. 178-179, 2007.

[122] D. J. Late, Y.-K. Huang, B. Liu, J. Acharya, S. N. Shirodkar, J. Luo, A. Yan, D. Charles, U. V. Waghmare, V. P. Dravid, and C. N. R. Rao, "Sensing Behavior of Atomically Thin-Layered MoS_2 Transistors," *ACS Nano*, vol. 7, pp. 4879-4891, 2013.

[123] S. Bae, H. Kim, Y. Lee, X. Xu, J.-S. Park, Y. Zheng, J. Balakrishnan, T. Lei, H. R. Kim, Y. I. Song, Y.-J. Kim, K. S. Kim, B. Ozyilmaz, J.-H. Ahn, B. H. Hong, and S. Iijima, "Roll-to-Roll Production of 30-Inch Graphene Films for Transparent Electrodes," *Nature Nanotechnology*, vol. 5, pp. 574-578, 2010.

[124] W. Park, J. Baik, T.-Y. Kim, K. Cho, W.-K. Hong, H.-J. Shin, and T. Lee, "Photoelectron Spectroscopic Imaging and Device Applications of Large-Area Patternable Single-Layer MoS_2 Synthesized by Chemical Vapor Deposition," *ACS Nano*, vol. 8, pp. 4961-4968, 2014.

[125] X. Liang, V. Giacometti, A. Ismach, B. D. Harteneck, D. L. Olynick, and S. Cabrini, "Roller-Style Electrostatic Printing of Prepatterned Few-Layer-Graphenes," *Applied Physics Letters*, vol. 96, 2010.

[126] H. Nam, S. Wi, H. Rokni, M. Chen, G. Priessnitz, W. Lu, and X. Liang, "MoS_2 Transistors Fabricated via Plasma-Assisted Nanoprinting of Few-Layer MoS_2 Flakes into Large-Area Arrays," *ACS Nano*, vol. 7, pp. 5870-5881, 2013.

[127] B. B. Aggarwal and K. Natarajan, "Tumor Necrosis Factors: Developments During the Last Decade," *European Cytokine Network*, vol. 7, pp. 93-124, 1996.

[128] D. Aderka, "The Potential Biological and Clinical Significance of the Soluble Tumor Necrosis Factor Receptors," *Cytokine and Growth Factor Reviews*, vol. 7, pp. 231-240, 1996.

[129] W. Shurety, A. Merino-Trigo, D. Brown, D. A. Hume, and J. L. Stow, "Localization and Post-Golgi Trafficking of Tumor Necrosis Factor-Alpha in Macrophages," *Journal of Interferon and Cytokine Research*, vol. 20, pp. 427-438, 2000.

[130] R. Gorlin, "The Biological Actions and Potential Clinical-Significance of Dietary PSI-3 Fatty-Acids," *Archives of Internal Medicine*, vol. 148, pp. 2043-2048, 1988.

[131] W. J. Frazier and M. W. Hall, "Immunoparalysis and Adverse Outcomes from Critical Illness," *Pediatric Clinics of North America*, vol. 55, pp. 647-668, 2008.

[132] M. W. Hall, N. L. Knatz, C. Vetterly, S. Tomarello, M. D. Wewers, H. D. Volk, and J. A. Carcillo, "Immunoparalysis and Nosocomial Infection in Children with Multiple Organ Dysfunction Syndrome," *Intensive Care Medicine*, vol. 37, pp. 525-532, 2011.

[133] M. Chen, H. Nam, S. Wi, L. Ji, X. Ren, L. Bian, S. Lu, and X. Liang, "Stable Few-Layer MoS_2 Rectifying Diodes Formed by Plasma-Assisted Doping," *Applied Physics Letters*, vol. 103, 2013.

[134] Y. J. Zhang, J. T. Ye, Y. Yornogida, T. Takenobu, and Y. Iwasa, "Formation of a Stable p-n Junction in a Liquid-Gated MoS_2 Ambipolar Transistor," *Nano Letters*, vol. 13, pp. 3023-3028, 2013.

[135] F. N. Ishikawa, M. Curreli, H.-K. Chang, P.-C. Chen, R. Zhang, R. J. Cote, M. E. Thompson, and C. Zhou, "A Calibration Method for Nanowire Biosensors to Suppress Device-to-Device Variation," *ACS Nano*, vol. 3, pp. 3969-3976, 2009.

[136] V. H. Perez-Luna, M. J. O'Brien, K. A. Opperman, P. D. Hampton, G. P. Lopez, L. A. Klumb, and P. S. Stayton, "Molecular Recognition between Genetically Engineered Streptavidin and Surface-Bound Biotin," *Journal of the American Chemical Society*, vol. 121, pp. 6469-6478, 1999.

[137] L. S. Jung, K. E. Nelson, P. S. Stayton, and C. T. Campbell, "Binding and Dissociation Kinetics of Wild-Type and Mutant Streptavidins on Mixed Biotin-Containing Alkylthiolate Monolayers," *Langmuir*, vol. 16, pp. 9421-9432, 2000.

[138] R. Samnakay, C. Jiang, S. L. Rumyantsev, M. S. Shur, and A. A. Balandin, "Selective Chemical Vapor Sensing with Few-Layer MoS_2 Thin-Film Transistors: Comparison with Graphene Devices," *Applied Physics Letters*, vol. 106, 2015.

[139] W. Wu, D. De, S.-C. Chang, Y. Wang, H. Peng, J. Bao, and S.-S. Pei, "High Mobility and High On/Off Ratio Field-Effect Transistors Based on Chemical Vapor Deposited Single-Crystal MoS_2 Grains," *Applied Physics Letters*, vol. 102, 2013.

[140] P. K. Ang, W. Chen, A. T. S. Wee, and K. P. Loh, "Solution-Gated Epitaxial Graphene as pH Sensor," *Journal of the American Chemical Society*, vol. 130, pp. 14392-14393, 2008.

[141] P. K. Ang, A. Li, M. Jaiswal, Y. Wang, H. W. Hou, J. T. L. Thong, C. T. Lim, and K. P. Loh, "Flow Sensing of Single Cell by Graphene Transistor in a Microfluidic Channel," Nano Letters, vol. 11, pp. 5240-5246, 2011.

[142] J. Lee, P. Dak, Y. Lee, H. Park, W. Choi, M. A. Alam, and S. Kim, "Two-dimensional Layered MoS_2 Biosensors Enable Highly Sensitive Detection of Biomolecules," *Scientific Reports*, vol. 4, 2014.

[143] E. Abrahams, P. W. Anderson, D. C. Licciardello, and T. V. Ramakrishnan, "Scaling Theory of Localization: Absence of Quantum Diffusion in Two Dimensions," *Physical Review Letters*, vol. 42, pp. 673-676, 1979.

[144] P. W. Anderson, "Absence of Diffusion in Certain Random Lattices," *Physical Review*, vol. 109, pp. 1492-1505, 1958.

[145] O. P. Sinha, "Charge Redistribution in Anderson Model," *American Journal of Physics*, vol. 38, pp. 996, 1970.

[146] K. Takashima and T. Yamamoto, "Conductance Fluctuation of Edge-Disordered Graphene Nanoribbons: Crossover from Diffusive Transport to Anderson Localization," *Applied Physics Letters*, vol. 104, 2014.

[147] M. Reth, "Matching Cellular Dimensions with Molecular Sizes," *Nature Immunology*, vol. 14, pp. 765-767, 2013.

[148] S. McDonnell, B. Brennan, A. Azcatl, N. Lu, H. Dong, C. Buie, J. Kim, C. L. Hinkle, M. J. Kim, and R. M. Wallace, "HfO_2 on MoS_2 by Atomic Layer Deposition: Adsorption Mechanisms and Thickness Scalability," *ACS Nano*, vol. 7, pp. 10354-10361, 2013.

[149] L. Zheng, X. Cheng, Y. Yu, Y. Xie, X. Li, and Z. Wang, "Controlled Direct Growth of Al_2O_3-Doped HfO_2 Films on Graphene by H_2O-Based Atomic Layer Deposition," *Physical Chemistry Chemical Physics*, vol. 17, pp. 3179-3185, 2015.

[150] H. Alles, J. Aarik, A. Aidla, A. Fay, J. Kozlova, A. Niilisk, M. Pars, M. Rahn, M. Wiesner, and V. Sammelselg, "Atomic Layer Deposition of HfO_2 on Graphene from $HfCl_4$ and H_2O," *Central European Journal of Physics*, vol. 9, pp. 319-324, 2011.

[151] M. Chen, H. Nam, H. Rokni, S. Wi, J. S. Yoon, P. Chen, K. Kurabayashi, W. Lu, and X. Liang, "Nanoimprint-Assisted Shear Exfoliation (NASE) for Producing Multilayer MoS_2 Structures as Field-Effect Transistor Channel Arrays," *ACS Nano*, vol. 9, pp. 8773-8785, 2015.

[152] H. Nam, B.-R. Oh, P. Chen, J. S. Yoon, S. Wi, M. Chen, K. Kurabayashi, and X. Liang, "Two Different Device Physics Principles for Operating MoS_2 Transistor

Biosensors with Femtomolar-Level Detection Limits," *Applied Physics Letters*, vol. 107, 2015.

[153] H. Nam, B. R. Oh, M. K. Chen, S. Wi, D. Li, K. Kurabayashi, and X. Liang, "Fabrication and Comparison of MoS_2 and WSe_2 Field-Effect Transistor Biosensors," *Journal of Vacuum Science & Technology B*, vol. 33, p. 7, 2015.

[154] M. S. Luchansky and R. C. Bailey, "Rapid, Multiparameter Profiling of Cellular Secretion Using Silicon Photonic Microring Resonator Arrays," *Journal of the American Chemical Society*, vol. 133, pp. 20500-20506, 2011.

[155] A. Atkinson, "Growth of NiO and SiO_2 Thin-Films," *Philosophical Magazine B-Physics of Condensed Matter Statistical Mechanics Electronic Optical and Magnetic Properties*, vol. 55, pp. 637-650, 1987.

[156] D. Sarantaridis and A. Atkinson, "Redox Cycling of Ni-Based Solid Oxide Fuel Cell Anodes: A Review," *Fuel Cells*, vol. 7, pp. 246-258, 2007.

[157] G. S. Kulkarni and Z. Zhong, "Detection beyond the Debye Screening Length in a High-Frequency Nanoelectronic Biosensor," *Nano Letters*, vol. 12, pp. 719-723, 2012.

[158] W. H. Lee, J.-M. Lee, M. Uhm, J. Lee, K. R. Kim, S.-J. Choi, D. M. Kim, Y.-J. Jeong, and D. H. Kim, "Characterization and Capacitive Modeling of Target Concentration-Dependent Subthreshold Swing in Silicon Nanoribbon Biosensors," *IEEE Electron Device Letters*, vol. 35, pp. 587-589, 2014.

[159] K. Shoorideh and C. O. Chui, "Optimization of the Sensitivity of FET-Based Biosensors via Biasing and Surface Charge Engineering," *IEEE Transactions on Electron Devices*, vol. 59, pp. 3104-3110, 2012.

[160] D. J. Late, B. Liu, H. S. S. R. Matte, V. P. Dravid, and C. N. R. Rao, "Hysteresis in Single-Layer MoS_2 Field Effect Transistors," *ACS Nano*, vol. 6, pp. 5635-5641, 2012.

[161] M. S. Choi, G.-H. Lee, Y.-J. Yu, D.-Y. Lee, S. H. Lee, P. Kim, J. Hone, and W. J. Yoo, "Controlled Charge Trapping by Molybdenum Disulphide and Graphene in Ultrathin Heterostructured Memory Devices," *Nature Communications*, vol. 4, 2013.

[162] Y. Zhou, S.-T. Han, P. Sonar, and V. A. L. Roy, "Nonvolatile Multilevel Data Storage Memory Device from Controlled Ambipolar Charge Trapping Mechanism," *Scientific Reports*, vol. 3, 2013.

[163] M. Chen, H. Nam, S. Wi, G. Priessnitz, I. M. Gunawan, and X. Liang, "Multibit Data Storage States Formed in Plasma-Treated MoS_2 Transistors," *ACS Nano*, vol. 8, pp. 4023-4032, 2014.

[164] J. Quereda, A. Castellanos-Gomez, N. Agrait, and G. Rubio-Bollinger, "Single-layer MoS_2 Roughness and Sliding Friction Quenching by Interaction with Atomically Flat Substrates," *Applied Physics Letters*, vol. 105, 2014.

[165] H. Chaudhry, J. Zhou, Y. Zhong, M. M. Ali, F. Mcguire, P. S. Nagarkatti, and M. Nagarkatti, “Role of Cytokines as a Double-edged Sword in Sepsis,” *In Vivo*, vol. 27, pp. 669-684, 2013.